

FAULT TOLERANT QUANTUM COMPUTATION WITH SUPERCONDUCTING ELEMENTS:  
HIGH-FIDELITY GATE DESIGN AND TOPOLOGICAL ERROR CORRECTION

by

JOYDIP GHOSH

(Under the direction of Michael R. Geller)

ABSTRACT

Quantum computing with superconducting elements promises scalability and is widely regarded as a viable approach to develop a fault-tolerant architecture for a quantum computer. In this thesis, I address some hardware-related theoretical challenges encountered in realizing a quantum computer with superconducting devices. I first discuss how to design high-fidelity two-qubit entangling gates, especially the controlled- $\sigma^z$  (CZ) operation, and then explore the performance of some existing fault-tolerant superconducting architectures under a realistic multi-parameter error model.

Assuming phase or transmon qubits and using only low frequency qubit-bias control, our CZ operation exhibits threshold fidelity (intrinsic) with a realistic two-parameter pulse profile. In addition, we develop an analytic model that estimates the fidelities of CZ gates as a function of pulse parameters as well as quantifies the error due to any perturbation over an optimal pulse shape. Our analysis shows that leakage of population to non-computational states remains the dominant source of intrinsic error for such quantum operations. The effect of such leakage errors on the fault-tolerance of standard topological codes has remained largely unknown so far. We therefore explore the signature and consequences of such leakage

errors on ancilla-assisted Pauli operator measurement, which is a central ingredient for any standard topological error correction scheme. We consider a realistic coupled-qutrit model, parameterize the non-ideal CZ gate, and simulate the repeated ancilla-assisted measurement of a single  $\sigma^z$  operator. We find that there is the possibility of a less typical but dangerous type of leakage event in the data qubit, where ancilla becomes *paralyzed*, rendering it oblivious to data-qubit errors for many consecutive measurement cycles. The consequences of such paralysis on the fault-tolerance of standard topological codes are also discussed in this context.

Next we consider a realistic, multi-parameter error model and investigate the performance of surface code error correction for some possible superconducting architectures. We map amplitude and phase damping to the Pauli channel via the *Pauli Twirling Approximation*, and obtain the logical error rate as a function of the qubit coherence time, intrinsic state preparation, and gate and readout errors. A numerical Monte Carlo simulation is performed to obtain the logical error rates and a leading order analytic model is constructed to estimate their scaling behavior below threshold. Our results suggest that large-scale fault-tolerant quantum computation should be possible with existing superconducting devices.

INDEX WORDS: Superconducting qubits, CZ gate, quantum gate design, ancilla-assisted qubit measurement, topological error correction, surface code

FAULT TOLERANT QUANTUM COMPUTATION WITH SUPERCONDUCTING ELEMENTS:  
HIGH-FIDELITY GATE DESIGN AND TOPOLOGICAL ERROR CORRECTION

by

JOYDIP GHOSH

B.E., National Institute of Technology, Durgapur, India, 2005

M.S., George Mason University, Virginia, USA, 2008

A Dissertation Submitted to the Graduate Faculty  
of The University of Georgia in Partial Fulfillment  
of the

Requirements for the Degree

DOCTOR OF PHILOSOPHY

ATHENS, GEORGIA

2013

©2013

Joydip Ghosh

All Rights Reserved

FAULT TOLERANT QUANTUM COMPUTATION WITH SUPERCONDUCTING ELEMENTS:  
HIGH-FIDELITY GATE DESIGN AND TOPOLOGICAL ERROR CORRECTION

by

JOYDIP GHOSH

Approved:

Major Professor: Michael R. Geller

Committee: Henning Meyer  
Phillip C. Stancil

Electronic Version Approved:

Maureen Grasso  
Dean of the Graduate School  
The University of Georgia  
August 2013

**Fault Tolerant Quantum Computation with  
Superconducting Elements: High-fidelity  
Gate Design and Topological Error  
Correction**

Joydip Ghosh

July 18, 2013

*To my grandmother:*

Smt. Biva Rani Ghosh

# Acknowledgments

At the very outset, I would like to thank my advisor, Professor Michael Geller, for his extraordinary perseverance in steering my academic life successfully to the end of this doctoral program. Mike has always respected my ideas but has also been candid about their merits and demerits. His tranquil temperament in difficult times along with an astute discretion in expressing successful discoveries has been enormously useful for me to understand the balance between courage and caution in life as a whole. The most important aspect of research methodology that I learnt from him is how to extract important questions from a seemingly resolved scientific question. His perfectionist attitude toward presentation of scientific facts helped construct a logical mindset in me and I sincerely wish it would continue to prevail as the foundation of my own philosophy of science.

I would also like to thank Professor John Martinis, the great intuitive mind in the community of superconducting quantum computing, for his encouraging attitude toward my research endeavor. My interaction with John has been very limited but conversations with him have always inspired me to move forward. No words are sufficient to thank Dr. Austin Fowler for teaching me surface code through innumerable email communications. I am sincerely grateful to Professor Alexander (Sasha) Korotkov and Professor Frank Wilhelm for their honest suggestions that eventually turned out to be important for my research as well as my academic career. I would like to extend my heartfelt gratitude to Professor Franco Nori for inviting me to visit his research group at RIKEN. It is impossible for me to forget

my days in Japan—the lunchtime discussions, the fascinating skywatch session in the cold starry night, and above all, the warmth and friendship I received from the entire group. Professor Barry Sanders: Thank you so much for nominating me for the prestigious fellowship at Calgary, my next destination. I thank Professor Phillip Stancil and Professor Henning Meyer to serve on my PhD committee and also Phillip for involving me in one of his projects that exposed me to a slightly different type of research. Thanks to Professor Loris Magnani for his invaluable suggestions during various twists and turns in my graduate life at UGA.

I am definitely indebted to my parents for their continuous support and sacrifice since my childhood. I specially want to express my gratitude to all my teachers who have imbibed their knowledge in me and therefore helped construct the foundation of my current understanding.

Dr. Emily Pritchett and Dr. Andrei Galiautdinov deserve the utmost credits to help me grasp the subject in the early days of my involvement with the group. Needless to mention, I cannot forget your impact as long as I remain active in the community!

I especially thank Debasrita Bhakta for being a wonderful listener with relentless inquisitiveness as well as for proof-checking various parts of my thesis with utmost sincerity. It's also my great pleasure to acknowledge the valuable academic conversations I have had with Swapnonil Banerjee (UC Davis), Priyanka Chakraborti (WMU), Ashmita Das (IACS), Sayonita Ghoshhajra (UGA), Andrew (Jamie) Kerman (MIT-LL), Andrew Sornborger (UC-Davis), Hao You (UGA), Zhongyuan Zhou (UGA) and many many others. Last, but not the least, I thank all my friends, at UGA and elsewhere, for your love and respect, and I promise to do justice to the confidence that you have shown me.

The research conducted here was funded by the US Office of the Director of National Intelligence (ODNI), Intelligence Advanced Research Projects Activity (IARPA), and National Science Foundation (NSF). All statements of fact, opinion or conclusions contained herein are those of the author(s) and should not be construed as representing the official views or policies of the IARPA, the ODNI, the NSF, or the US Government.

# Contents

List of Figures	x
List of Tables	xv
<b>1 Introduction</b>	<b>1</b>
1.1 Quantum computation: A prelude . . . . .	2
1.2 Quantum computing with superconducting devices . . . . .	5
1.3 Quantum error correction and fault tolerance . . . . .	6
<b>2 Quantum Gate Design</b>	<b>7</b>
2.1 Formulation of the problem . . . . .	7
2.2 Controlled-NOT gate design . . . . .	10
2.3 Controlled- $\sigma^z$ gate for qubit-resonator model . . . . .	22
2.4 Controlled- $\sigma^z$ gate in QVN architecture . . . . .	59
<b>3 Ancilla-assisted Qubit Measurement</b>	<b>74</b>
3.1 Measurement protocol . . . . .	76
3.2 Coupled qutrit model . . . . .	77
3.3 Non-ideal Controlled- $\sigma^z$ gate . . . . .	83
3.4 Consequences for fault-tolerant quantum computation . . . . .	90

<b>4</b>	<b>Analysis of Fault-tolerant Architectures</b>	<b>91</b>
4.1	Mapping decoherence to a diagonal Pauli channel . . . . .	93
4.2	Physical and logical errors . . . . .	96
4.3	Architecture performance . . . . .	102
4.4	Summary . . . . .	112
<b>5</b>	<b>Conclusion</b>	<b>114</b>
<b>A</b>	<b>Derivation of Approximate Logical Error Rate</b>	<b>116</b>
<b>B</b>	<b>Coupled Qubit Model under Decoherence</b>	<b>122</b>
	<b>Bibliography</b>	<b>125</b>

# List of Figures

1.1	Bloch sphere representation of a single qubit. Each point on the surface of the sphere denotes a pure state and a rotation of the Bloch sphere about any of the axes represents a single-qubit Pauli $\sigma^x$ , $\sigma^y$ or $\sigma^z$ operation. . . . .	2
2.1	(Color online) Plot of optimal fidelity versus total gate time, averaged over randomly generated interactions with fixed values of $\eta$ , for $\eta = 0.1, 0.5$ , and $1.0$ . . . . .	14
2.2	(Color online) A plot of first six energy levels of a qubit coupled to a resonator at $g/h = 115$ MHz. . . . .	16
2.3	(Color online) A plot of control and leakage sensitivity vs. qubit frequency for $g/h = 115$ MHz. . . . .	18
2.4	(Color online) A plot of control and leakage sensitivity vs. coupling. . . . .	19
2.5	(Color online) A plot of fidelity vs. total gate time in nanoseconds. Red points are obtained via optimization and the blue line is an interpolation. . . . .	22
2.6	(Color online) A plot of qubit frequency vs. time for CNOT at total gate time=45 ns. . . . .	23
2.7	Layout of the four-qubit QVN processor. The $q_i$ represent superconducting qubits capacitively coupled to memory resonators $m_i$ as well as a resonator bus $b$ . . . . .	24

2.8	(Color online) Energies of eigenstates $ \overline{qb}\rangle$ of a single qubit $q$ coupled to a resonator bus $b$ . Here $\omega_b/2\pi = 6.5$ GHz, $\eta/2\pi = 300$ MHz, and $g_b/2\pi = 45$ MHz. The time dependence of the qubit frequency during a CZ gate (solid black curve) is indicated at the top of the figure. . . . .	26
2.9	Two-parameter CZ pulse profile (2.69) for the case of $\omega_{\text{on}}/2\pi = 6.8$ GHz, $\omega_{\text{off}}/2\pi = 7.5$ GHz, $t_{\text{ramp}} = 7$ ns, $\sigma = 1.24$ ns, and $t_{\text{on}} = 10$ ns. The total gate time excluding auxiliary $z$ rotations is $t_{\text{gate}} = 17$ ns. The example shown is representative of a 99.9% fidelity gate for a qubit with 300 MHz anharmonicity. 39	39
2.10	Detuning pulse profile (2.95) for a single frequency switch. . . . .	46
2.11	(Color online) $ A ^2$ versus switching time $\sigma$ for indicated values of $\Delta_{\text{on}}$ and $\Delta_{\text{off}}$ . 48	48
2.12	(Color online) Transition frequency for transmon with 300 and 400 MHz anharmonicity. . . . .	67
2.13	(Color online) Frequency diagram for the CZ gate between $q_1$ and bus. This diagram describes the gate of Table 2.5. The lines 1– 4 correspond to 4 memory resonators and horizontal axis corresponds time. . . . .	69
2.14	(Color online) $\text{QVN}_4$ mode diagram for the $\text{CZ}_{23}$ gate. Gaussian filtering of the pulse is not shown. . . . .	72
3.1	Protocol for ancilla-assisted $\sigma^z$ measurement. . . . .	76
3.2	(Color online) Energies of various levels, in the $ \text{AD}\rangle$ basis, as a function of $\epsilon_1/2\pi$ . Here $\epsilon_2/2\pi = 6$ GHz, the coupling strength is $g/2\pi = 25$ MHz, and $\eta_1/2\pi = \eta_2/2\pi = 200$ MHz. . . . .	78
3.3	(Color online) Simulated repeated readout of the ancilla qutrit in the presence of amplitude damping. Single peaks, upward or downward, indicate errors on the ancilla. Data errors result in steps; an example is shown near cycle 1000. In this simulation we assume $T_1 = 40 \mu\text{s}$ , $T_2 = 2T_1$ , and $t_{\text{cycle}} = 45$ ns. . . . .	82

3.4	(Color online) Simulated sequential measurements of the ancilla qubit. The readout values $ 0\rangle$ or $ 1\rangle$ are shown as a function of measurement cycle number. Red rectangles signify leakage events, where the data $ 2\rangle$ state probability is close to unity. Random ancilla oscillations during the leakage events are observed except when $\theta \approx 0$ . Two values of $W$ are given for each trace: the theoretical value from (3.27) and a value, shown in parentheses, numerically computed from the simulation. The simulations assume $T_1 = 40 \mu s$ , $T_2 = 2T_1$ , $\chi_i = \zeta_i = 10^{-2}$ for all $i = 1, \dots, 4$ , and random values of phase angle parameters consistent with the indicated values of $\theta$ . . . . .	89
4.1	(Color online) A schematic diagram of distance-3 surface code is shown. Two possible error chains, $X_L$ (purple and horizontal) and $Z_L$ (magenta and vertical), are displayed and various terminologies used in here are illustrated. Syndrome $Z$ operators are shown in green (labelled by $Z$ ) and syndrome $X$ operators are in yellow (labelled by $X$ ). An error chain starting and ending at the same boundary is referred to as a ‘clasp’ and is shown in gray color. . . . .	98
4.2	(Color online) A schematic diagram of a surface code error correction cycle is shown. The red region (dark gray leftmost region) contains state preparation, the blue region (medium gray middle part) contains four consecutive CNOT operations and the green region (light gray) highlights the measurements of syndrome $Z$ and $X$ qubits. . . . .	99
4.3	(Color online) Plot of analytic estimate of logical $X$ error probability per cycle vs. single physical qubit error probability per timestep. Solid lines denote numerical estimates via Monte-Carlo simulation while dashed lines are obtained from our analytical formula given by Eq. (A.6). . . . .	101

4.4	(Color online) Layout of the distance-3 surface code considered here. Open circles denote data qubits, and light green (dark blue) filled circles denote $X$ -type ( $Z$ -type) syndrome qubits. The dashed lines denote tunable qubit-qubit coupling. We refer to this hardware design as the textbook architecture. . . .	104
4.5	(Color online) Logical $X$ and $Z$ error rate per cycle is shown as a function of coherence time $T_1$ for the textbook architecture. Plots for $d = 3$ are shown in blue and those for $d = 5$ are shown in red. . . . .	105
4.6	(Color online) Schematic diagram of the distance-3 Helmer architecture. The circles represent superconducting qubits, with “idle” frequencies indicated by their colors. The horizontal and vertical magenta (gray) rectangles are resonators. All horizontal (vertical) resonators have the same frequency. . . . .	106
4.7	(Color online) Logical $X$ and $Z$ error rate per cycle is shown as a function of coherence time $T_1$ for the Helmer architecture. Plots for $d = 3$ are shown in blue and those for $d = 5$ are shown in red. . . . .	107
4.8	(Color online) Schematic diagram of the architecture discussed by DiVincenzo [1] for code distance $d=3$ . The filled circles with boundaries represent qubits, squares with boundaries represent resonators, and colors of both denote their fixed frequencies. The unbounded circles are for the eye and indicate whether a given block is for data (dark gray), $X$ -type syndrome (light green), or $Z$ -type syndrome (blue). A possible frequency allocation for all the components is shown. . . . .	108
4.9	(Color online) Logical $X$ and $Z$ error rate per cycle is shown as a function of coherence time $T_1$ for the DiVincenzo architecture. Plots for $d = 3$ are shown in blue and those for $d = 5$ are shown in red. . . . .	110

4.10 (Color online) Various possible fixed coupling-based architectures are shown for  $d=3$  surface code. The circles denote qubits, squares denote resonators and various colors (grayscale) denote a possible frequency allocation. (a) An architecture where superconducting qubits are arranged in a two-dimensional square lattice each coupled to its nearest neighbor with fixed couplers. (b) An architecture where superconducting qubits are used for data qubits and resonators for syndrome qubits coupled via fixed couplers. Each resonator is also coupled to another qubit required for read out. (c) Same as architecture (b) except for the fact that each qubit is also coupled to another resonator used as its memory. (d) In this architecture each qubit in a two-dimensional square lattice is coupled to its nearest neighbor via a resonator. . . . . 112

A.1 (Color online) Data qubits (red filled circles) of a single row in a distance-5 surface code is shown in two subsequent time slices. The blue filled circles denote measurement locations. An error in any measurement location generates two adjacent timelike syndrome events. . . . . 119

B.1 (Color online) Plot of leakage probability from  $|11\rangle$  state under decoherence for various  $g$  during a CZ operation vs total CZ operation time. . . . . 124

# List of Tables

2.1	Parameter values used in the simulation. The tuned qubit frequency is the frequency of the qubits used during the entangling operations. The ranges of allowed values of Rabi frequencies and overall coupling strengths are used to constrain the optimization. $J_{\mu\nu}^*$ and $g$ are defined in Eq. (2.12). . . . .	12
2.2	Optimum values of parameters for CNOT gate. . . . .	21
2.3	Device parameters used for QVN <sub>4</sub> architecture. . . . .	25
2.4	CZ pulse shape precision requirements. The bounds listed in the $t_{\text{on}}$ column assume that this is the only type of pulse parameter inaccuracy present, with an (estimated) error given in the first column, and that the auxiliary $z$ rotation angles are reoptimized and implemented perfectly. The $\omega_{\text{on}}$ bounds are defined analogously. The error $\mathbb{E}$ is defined in (2.115). . . . .	56

2.5	Optimal state-averaged process fidelity $F_{\text{ave}}$ for the Strauch CZ gate between qubit $q_1$ and the bus, in the QVN <sub>4</sub> processor of Fig. 2.7. No decoherence or noise is included here. Specifications for 99.9% and 99.99% gates are provided for three values of qubit anharmonicity $\eta$ . The parameters $t_{\text{ramp}}$ and $\sigma$ characterize the pulse switching time, and $t_{\text{gate}}$ is the total gate time excluding auxiliary $z$ rotations. $F_{ 11\rangle}$ is the minimum fidelity, which is also the fidelity of the $ 11\rangle$ state if it is occupied initially. Data after double vertical lines give the nonadiabatic switching error and minimum fidelity estimates; these quantities are defined and discussed in Sec. 2.3.6. . . . . .	68
2.6	Optimal QVN <sub>4</sub> gate fidelity for a Strauch CZ gate between qubit $q_1$ and the bus. . . . .	71
4.1	Parameters assumed for the three fault-tolerant architectures. . . . .	102
4.2	Time duration for each step in the error-correction cycle for DiVincenzo architecture. . . . .	109
4.3	Fault-tolerant $T_1$ thresholds for the three architectures studied in this work. . . . .	113
B.1	Optimal parameters and results obtained for CNOT gate in this coupled qubit model. We use these results for the estimation of logical error rate in textbook architecture. . . . .	123

# Chapter 1

## Introduction

*Those who are in love with practice without knowledge are like the sailor who gets into a ship without rudder or compass and who can never be certain where he is going. Practice must always be founded on sound theory, and to this Perspective is the guide and the gateway.*

– Leonardo Da Vinci

Quantum mechanics, with its exotic outfit and unusual content, survived all possible practical challenges and gradually became a pivotal component of modern physics. The profound philosophical debate between Niels Bohr and Albert Einstein continued among generations of physicists in various forms and was eventually resolved by a series of decisive experiments. Quantum mechanics thus became a ‘sound theory’ by the end of last century. The idea of a quantum computer, a computing device powered by the laws of quantum mechanics and capable of solving a class of problems exponentially faster than a classical computer, began to emerge in the late 20<sup>th</sup> century [2]. Realizing a quantum computer with superconducting elements is one of the most promising schemes proposed so far [3, 4]. The era of superconducting quantum computing began in 2002 with the discovery that a long-lived quantum state can be prepared, controlled, and measured in a current biased

Josephson junction [5,6] as well as in a Cooper-pair box [7]. In this thesis, I discuss various theoretical challenges encountered so far, especially in designing high-fidelity quantum gates and performing fault-tolerant quantum computation with superconducting devices.

## 1.1 Quantum computation: A prelude

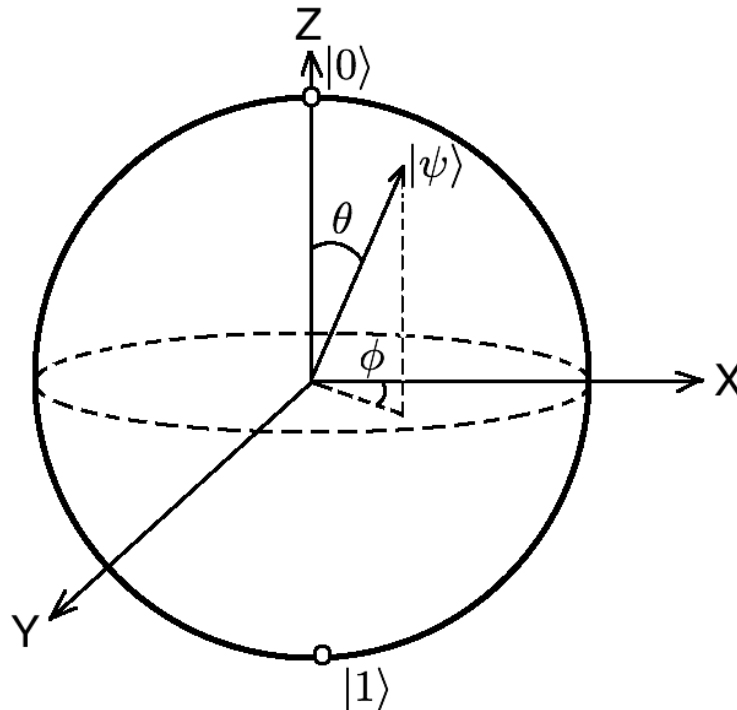


**Figure 1.1:** Bloch sphere representation of a single qubit. Each point on the surface of the sphere denotes a pure state and a rotation of the Bloch sphere about any of the axes represents a single-qubit Pauli  $\sigma^x$ ,  $\sigma^y$  or  $\sigma^z$  operation.

In this section, I briefly describe some key concepts of quantum computation as well as its current status in the context of superconducting quantum computing. DiVincenzo put forward a set of necessary criteria for the implementation of a quantum computer [8]. The requirements include scalability, ability to initialize the qubits, long coherence time, ability to carry out a universal set of gates, and ability to perform measurements on each qubit.

Designing high-fidelity quantum gates is, therefore, a crucial part of this implementation process as well as one of the main goals of my thesis. The *universality theorem* guarantees that the single qubit rotations along with any two-qubit entangling operation, such as Controlled- $\sigma^z$  (CZ), construct a universal set, such that any arbitrary element of  $SU(2^n)$  can be reduced to a finite sequence of these elements [9]. In the so-called ‘Bloch sphere’ representation (see Fig. 1.1), a single qubit rotation means designing a quantum operation on the single qubit in order to rotate any pure state  $|\psi\rangle$  (denoted by the radial vector in Fig. 1.1) to another pure state. Motzoi *et al.* recently addressed the problem of designing high-fidelity single qubit operations using an approach called Derivative Removal by Adiabatic Gate (DRAG) [10], and it has been shown that it is possible to suppress the leakage of population to the non-computational  $|2\rangle$  state exponentially, which gives rise to arbitrarily high-fidelity single qubit gates.

Since the universality theorem requires at least one entangling two-qubit operation, a natural question to ask at this point is how to design a high-fidelity two-qubit entangling gate. We investigate this question in Ch. 2, mainly focusing on the CZ gate as our entangling operation. In the computational basis ( $\{|00\rangle, |01\rangle, |10\rangle, |11\rangle\}$ ), a CZ operation can be represented by a  $4 \times 4$  matrix as,

$$\text{CZ} = \begin{bmatrix} 1 & 0 & 0 & 0 \\ 0 & 1 & 0 & 0 \\ 0 & 0 & 1 & 0 \\ 0 & 0 & 0 & -1 \end{bmatrix}, \quad (1.1)$$

which means, it acts like an Identity operation on each basis state except for  $|11\rangle$  state, which acquires a minus sign (or equivalently a phase of angle  $\pi$ ). Another well-known two-qubit entangling operation is Controlled-NOT (CNOT), which can also be expressed in a matrix

form as,

$$\text{CNOT} = \begin{bmatrix} 1 & 0 & 0 & 0 \\ 0 & 1 & 0 & 0 \\ 0 & 0 & 0 & 1 \\ 0 & 0 & 1 & 0 \end{bmatrix}, \quad (1.2)$$

in the same computational basis. Note that, unlike CZ, CNOT does not preserve the symmetry under the exchange of qubit indices. Therefore, two qubits have different roles to play for a CNOT gate and one qubit is referred to as *control* and another one as *target* qubit. The action of CNOT on two-qubit basis states is such that when the control qubit is  $|0\rangle$ , it acts as an Identity on the target, and when the control qubit is  $|1\rangle$ , it performs a  $\sigma^x$  rotation of angle  $\pi$  on the target qubit. Notice that, we can convert a CZ gate into a CNOT gate (and the vice-versa) with some pre and post single qubit operations,

$$\text{CZ} = \text{H}_2 \text{CNOT} \text{H}_2 \quad \text{and} \quad \text{CNOT} = \text{H}_2 \text{CZ} \text{H}_2, \quad (1.3)$$

where  $\text{H}_2$  denotes a Hadamard gate (H) on the second (target) qubit. Hadamard is a single qubit operation, defined as (in  $\{|0\rangle, |1\rangle\}$  basis),

$$\text{H} = \frac{1}{\sqrt{2}} \begin{bmatrix} 1 & 1 \\ 1 & -1 \end{bmatrix}. \quad (1.4)$$

If it is possible to transform a two-qubit gate into another one under some pre- and post-local rotations, they are referred to as *equivalent* to each other. It is important to note that CZ and CNOT belong to the same equivalence class.

Measuring a qubit is one of the DiVincenzo criteria and, therefore, essential in realizing a quantum computer. There exist numerous approaches to measure a superconducting qubit. In this thesis, I always assume the approach developed recently by Sete *et al.* [11]. For

fault-tolerant quantum computation, it is often required to measure a single (data) qubit via another (ancilla) qubit, commonly referred to as ancilla-assisted measurement. In Ch. 3, I discuss the ancilla-assisted measurement of a single qubit and explore its consequences for topological quantum error correction.

## 1.2 Quantum computing with superconducting devices

Superconducting devices are promising especially due to their long coherence time. In this section, I give a short review (for details see [12]) of two superconducting devices, a transmon qubit and a resonator, which are relevant for our purposes here.

A transmon is a modified version of a superconducting charge qubit, designed to operate in the regime where  $E_J/E_C > 1$ ,  $E_J$  and  $E_C$  being the Josephson energy and charging energy respectively [13]. Another variant of transmon, sometimes referred to as *Xmon*, has recently been developed by Barends *et al.* [14]. Xmon qubits are scalable having long coherence times ( $T_1 \sim 44 \mu\text{s}$ ) as well as suitable for two-dimensional fault-tolerant architectures as required by surface or toric code. In our work here, we mostly assume frequency-tunable transmon (or Xmon) as our superconducting qubit, unless otherwise specified.

There exist varieties of superconducting resonators and in our work we mostly assume the coplanar waveguide (CPW) resonator as our cavity, which has already been demonstrated with an internal quality factor above  $10^7$  [15]. A superconducting transmon qubit can be coupled to a CPW resonator with a fixed coupling by placing it near the antinode of a specific mode (called the ‘resonant’ mode) of the resonator. Two transmon qubits can also be coupled directly in various ways, while for our purpose we assume fixed capacitive coupling [16–18], as opposed to tunable coupling [19–31].

### 1.3 Quantum error correction and fault tolerance

There are two dominant sources of error in a given quantum gate operation: Intrinsic and decoherence-induced. Intrinsic error characterizes the distance between the ideal target quantum gate and the practically achievable operation closest to it in the long coherence limit. In Ch. 2, I discuss the various sources of intrinsic error mechanisms in detail for the CZ gate. In superconducting quantum computing, the decoherence-induced errors are mostly generated by the finite  $T_1$  (relaxation time) and  $T_2$  (dephasing time) of the qubits and resonators.

If the errors are unavoidable, how is it possible to run a quantum algorithm in a quantum computer for an arbitrarily long time? There exists a celebrated theorem in quantum computing, called the *threshold theorem*, which says, provided we somehow bound the error of each quantum gate below a certain threshold, quantum error-correcting codes can be used to efficiently perform an arbitrarily long quantum computation [9]. Topological quantum error-correcting codes (e.g., surface or toric code), where a quantum information is protected by encoding it in a topological excitation of a fault-tolerant architecture, recently attract significant attention primarily due to their high error threshold. In Ch. 4, I consider some existing fault-tolerant (based on surface code) superconducting architectures and analyze their performance under a realistic multi-parameter error model.

# Chapter 2

## Quantum Gate Design

*Design is so simple, that's why it is so complicated.*

– Paul Rand

Designing high-fidelity quantum gates is one of the key requirements for the realization of a quantum computer. As mentioned earlier, single qubit rotations along with a two-qubit entangling gate construct a universal set of quantum gates. I concentrate on two-qubit entangling gates in this chapter. First, I describe briefly how to design a CNOT gate using Weyl chamber and spectroscopic approaches and next discuss the anticrossing-based CZ gate in detail.

### 2.1 Formulation of the problem

In this section, I elucidate the formulation of quantum gate design problem for a two-qubit operation from the perspective of quantum control. The Hamiltonian of a coupled-qubit system,

$$H(\epsilon_1, \eta_1, \epsilon_2, \eta_2, g), \tag{2.1}$$

can be represented by a  $k^2 \times k^2$  matrix.  $k$  denotes the number of energy levels in each qubit,  $\epsilon_i$  and  $\eta_i$  are the frequency and anharmonicity of the  $i^{\text{th}}$  qubit respectively, and  $g$  denotes the coupling between two qubits. For an ideal qubit  $k = 2$ , but superconducting qubits usually contain higher energy levels and therefore  $k > 2$  for our qubits. In our work, we mostly assume fixed coupling between the qubits (*i.e.*,  $g$  is time-independent) and ignore any frequency-dependence of anharmonicities. So, the Hamiltonian is time-dependent only via qubit frequencies,  $\epsilon_1$  and  $\epsilon_2$ . The unitary time-evolution operator for any time-dependent Hamiltonian can be expressed as,

$$U(t_{\text{gate}}) = \widehat{\mathcal{T}} \exp \left[ -i \int_0^{t_{\text{gate}}} H(t) dt \right], \quad (2.2)$$

where  $\widehat{\mathcal{T}}$  is the so-called time-ordering operator and  $H(t) \equiv H(\epsilon_1(t), \eta_1, \epsilon_2(t), \eta_2, g)$ . For a gate design problem, we are interested to find a control pulse for the qubit frequencies,  $\epsilon_1(t)$  and  $\epsilon_2(t)$ , such that  $U(t_{\text{gate}})$  is the given target quantum gate ( $U_{\text{target}}$ ), we want to design. So, quantum gate design problem can be thought of as an inverse of the usual time evolution problem, where the time-dependent Hamiltonian is known and the propagator is supposed to be determined using exponential or some more elegant technique.

In practice, the designed unitary gate  $U$  is not exactly same as  $U_{\text{target}}$ , and it is required to define a (normalized) fidelity function  $F$ , which quantifies the closeness between  $U$  and  $U_{\text{target}}$ . A natural way to understand this closeness is to take a randomly generated vector  $|\chi\rangle$  (defined on a Hilbert space), apply the operations  $U$  and  $U_{\text{target}}$  on the vector to obtain transformed vectors  $U|\chi\rangle$  and  $U_{\text{target}}|\chi\rangle$ , and then define the overlap between these transformed states as an expression for fidelity that depends on the state  $|\chi\rangle$ ,

$$F_{\chi}(U_{\text{target}}, U) = \langle \chi | U_{\text{target}}^{\dagger} U |\chi\rangle \langle \chi | U^{\dagger} U_{\text{target}} |\chi\rangle. \quad (2.3)$$

Finally, we average over randomly generated  $|\chi\rangle$  (chosen from a uniform distribution) to introduce an average fidelity, according to

$$F(U_{\text{target}}, U) = \frac{1}{N(|\chi\rangle)} \sum_{|\chi\rangle} F_{\chi}(U_{\text{target}}, U), \quad (2.4)$$

where  $N(|\chi\rangle)$  is the total number of randomly generated  $|\chi\rangle$  states. To obtain a closed form expression of fidelity we change this sum to an integral,

$$F(U_{\text{target}}, U) = \int |\langle\chi| \mathcal{M} |\chi\rangle|^2 dV, \quad (2.5)$$

where  $\mathcal{M} \equiv U_{\text{target}}^{\dagger} U$  and  $dV$  is a normalized measure. It has already been proven [32–34] that, for any linear operator  $M$  on an  $n$ -dimensional complex Hilbert space,

$$\int_{S^{2n-1}} |\langle\chi| M |\chi\rangle|^2 dV = \frac{\text{Tr}(MM^{\dagger}) + |\text{Tr}(M)|^2}{n(n+1)}, \quad (2.6)$$

where the normalized state vectors  $|\chi\rangle$  are defined on the unit sphere  $S^{2n-1}$  in  $\mathbb{C}$ . Using Eq.(2.6) for a  $n$ -dimensional Hilbert space and assuming  $U_{\text{target}}$  as an unitary operator, we can rewrite our expression for average normalized fidelity as

$$F(U_{\text{target}}, U) = \frac{\text{Tr}(U^{\dagger}U) + \left| \text{Tr}(U_{\text{target}}^{\dagger}U) \right|^2}{n(n+1)}. \quad (2.7)$$

In what follows, we use (2.7) as our definition of fidelity between any two quantum operations and express it in percent.

## 2.2 Controlled-NOT gate design

In this section, I discuss two approaches to design a CNOT gate, the Weyl chamber approach and the conditional spectroscopic approach.

### 2.2.1 Weyl chamber approach <sup>1</sup>

Designing two-qubit quantum gates using Weyl chamber approach was proposed by Zhang *et al.* [35,36]. Geller *et al.* used this geometric approach to derive a pulse sequence for a CNOT gate for a four-dimensional coupled-qubit model with weak but otherwise arbitrary coupling between the two qubits [37]. In this section, I first describe the coupled-qubit model and CNOT pulse sequence, and then explore how the resulting fidelity of the CNOT gate depends on total gate time for various exchange interactions [38].

The Hamiltonian of a coupled-qubit system can be written as

$$H = \sum_{i=1,2} \left[ -\frac{\epsilon_i}{2} \sigma_i^z + \Omega_i \cos \left( \frac{\epsilon_i t}{\hbar} + \phi_i \right) \sigma_i^x \right] + \sum_{\mu,\nu=x,y,z} J_{\mu\nu} \sigma_1^\mu \otimes \sigma_2^\nu, \quad (2.8)$$

where  $J_{\mu\nu}$  is a  $3 \times 3$  coupling matrix which takes different forms for different architectures under consideration. The parameters  $\epsilon_i$  and  $\Omega_i$  (with  $\Omega_i \ll \epsilon_i$ ) are qubit frequency and Rabi frequency of the  $i^{th}$  qubit and are assumed to be tunable. Also, weak coupling ( $|J_{\mu\nu}| \ll \epsilon_i$ ) is assumed for our purpose here. The CNOT gates are implemented according to a pulse sequence consisting of two entangling operations along with single qubit rotations. The entangling operations are carried out with tuned qubits ( $\epsilon_1 = \epsilon_2$ ) and the local rotations are performed with detuned qubits. For weakly coupled tuned qubits, the Hamiltonian (2.8) can

---

<sup>1</sup>J. Ghosh and M. R. Geller, *Physical Review A* **81**, 052340 (2010) [Copyrighted material reprinted in this section as per transfer of copyright agreement with the publisher].

be written in the interaction picture (or rotating frame) as

$$H \approx \sum_{i=1,2} \frac{\Omega_i}{2} (\cos \phi_i \sigma_i^x - \sin \phi_i \sigma_i^y) + \mathcal{H}, \quad (2.9)$$

where

$$\mathcal{H} \equiv J (\sigma_1^x \sigma_2^x + \sigma_1^y \sigma_2^y) + J_{zz} \sigma_1^z \sigma_2^z + J' (\sigma_1^x \sigma_2^y - \sigma_1^y \sigma_2^x). \quad (2.10)$$

The parameters  $J$  and  $J'$  in Eq.(2.10) are given by

$$J \equiv \frac{J_{xx} + J_{yy}}{2} \quad \text{and} \quad J' \equiv \frac{J_{xy} - J_{yx}}{2}. \quad (2.11)$$

In order to quantify the strength of an exchange interaction, we decompose the coupling tensor  $J_{\mu\nu}$  according to

$$J_{\mu\nu} = g \times J_{\mu\nu}^*, \quad (2.12)$$

where  $g > 0$  is a measure of the overall strength and  $J_{\mu\nu}^*$  describes the form of the coupling.  $J_{\mu\nu}^*$  is defined to satisfy

$$|J_{\mu\nu}^*| \leq 1 \quad \text{for all } \mu, \nu. \quad (2.13)$$

Three important examples of  $J_{\mu\nu}^*$  are given in Table 2.1.

The pulse sequence derived in Ref. [37], carried out from right to left, is

$$\begin{aligned} \text{CNOT} = & e^{i\frac{3\pi}{4}} R_y \left( -\frac{\pi}{2} \right)_1 R_x \left( -\frac{\pi}{2} \right)_2 R_z (-\varphi)_2 R_x \left( \frac{\pi}{2} \right)_1 \\ & \times e^{-i\mathcal{H}\Delta t/\hbar} R_x (\pi)_1 e^{-i\mathcal{H}\Delta t/\hbar} R_z (\varphi)_2 R_y \left( \frac{\pi}{2} \right)_1, \end{aligned} \quad (2.14)$$

where  $R_\mu(\theta)_i \equiv e^{-\frac{i}{2}(\theta)\sigma_i^\mu}$  (with  $\mu = x, y, z$  and  $i=1,2$ ) is a single qubit rotation. Here

$$\varphi \equiv \arg(J + iJ') \quad \text{and} \quad \Delta t \equiv \frac{\pi\hbar}{8\sqrt{J^2 + J'^2}}. \quad (2.15)$$

**Table 2.1:** Parameter values used in the simulation. The tuned qubit frequency is the frequency of the qubits used during the entangling operations. The ranges of allowed values of Rabi frequencies and overall coupling strengths are used to constrain the optimization.  $J_{\mu\nu}^*$  and  $g$  are defined in Eq. (2.12).

parameter	value
common tuned qubit frequency $\epsilon/h$	10 GHz
qubit-qubit detuning	1 GHz
range of allowed Rabi frequencies $\Omega/h$	50-500 MHz
range of allowed coupling strengths $g/h$	1-500 MHz
range of gate times $t_{\text{gate}}$ considered	10-50 ns
$J_{\mu\nu}^*$ for Isotropic Heisenberg coupling	$\begin{bmatrix} 1 & 0 & 0 \\ 0 & 1 & 0 \\ 0 & 0 & 1 \end{bmatrix}$
$J_{\mu\nu}^*$ for Ising coupling	$\begin{bmatrix} 0 & 0 & 0 \\ 0 & 0 & 0 \\ 0 & 0 & 1 \end{bmatrix}$
$J_{\mu\nu}^*$ for XY coupling	$\begin{bmatrix} 1 & 0 & 0 \\ 0 & 1 & 0 \\ 0 & 0 & 0 \end{bmatrix}$

The operator  $e^{-i\mathcal{H}\Delta t/\hbar}$  represents the action of bringing the qubits into resonance for a time  $\Delta t$ . The CNOT pulse sequence given in Eq.(2.14) involves two rotations about the  $z$  axis. For our exact simulations below, it will be convenient to rewrite (2.14) in terms of  $x$  and  $y$  rotations, leading to

$$\begin{aligned} \text{CNOT} = e^{i\frac{3\pi}{4}} & \left[ R_y\left(\frac{\pi}{2}\right)_1 R_x\left(-\frac{\pi}{2}\right)_2 \right] R_y(\varphi)_2 R_x\left(\frac{\pi}{2}\right)_2 e^{-i\mathcal{H}\Delta t/\hbar} R_x(\pi)_1 e^{-i\mathcal{H}\Delta t/\hbar} \\ & \times \left[ R_x\left(\frac{\pi}{2}\right)_1 R_x\left(-\frac{\pi}{2}\right)_2 \right] R_y(-\varphi)_2 R_y\left(\frac{\pi}{2}\right)_1. \end{aligned} \quad (2.16)$$

This is the CNOT pulse sequence used in the present analysis. Operations inside square brackets can be performed simultaneously.

Now, I present the results obtained from numerical simulations. The results show the dependence of fidelity as a function of total gate time for various possible exchange interactions. It is observed that the fidelity curves are mostly independent on the form of interaction, unless the interaction is sufficiently close to that of the Ising model (see Table 2.1 for various parameter values used in the simulation). To quantify this closeness we define a parameter [recall (2.11) and (2.12)],

$$\eta \equiv \frac{\sqrt{J^2 + J'^2}}{g}. \quad (2.17)$$

It can be shown that  $0 \leq \eta \leq \sqrt{2}$ . For the Ising interaction,  $\eta = 0$ , whereas for the Heisenberg and XY interactions,  $\eta = 1$ . Given that the fidelity is largely independent of the form of interaction, as long as  $\eta$  is not too small, it is useful to average over interaction forms to obtain interaction-independent fidelity curves. This is provided in Fig. 2.1, which presents interaction-averaged fidelity curves for  $\eta = 0.1, 0.5$ , and  $1.0$ .

While the pulse profile required for a CNOT gate at  $\eta \rightarrow 0$  is much simpler [35, 37], the origin of the poor fidelity of (2.16), when  $\eta$  is small (as shown by Fig. 2.1), can be understood as follows: In the pulse construction (2.16) of Ref. [37], a Cartan decomposition is used to decompose the time-evolution operator generated by (2.9) into single-qubit rotations, an entangling operator, and a global phase factor. The entangler has the form

$$A(x, y, z) \equiv e^{-i(x\sigma_1^x\sigma_2^x + y\sigma_1^y\sigma_2^y + z\sigma_1^z\sigma_2^z)}, \quad (2.18)$$

where  $x, y$ , and  $z$  are three coordinates (angles). Following Zhang *et al.* [35], the entangler coordinates trace out a trajectory in the three-dimensional space of entanglers as time progresses. In the construction of Ref. [37], the trajectory starts in the plane  $x = y$ , and then a refocusing  $\pi$  pulse is used to reflect the trajectory to the point  $(\frac{\pi}{4}, 0, 0)$  or  $(-\frac{\pi}{4}, 0, 0)$

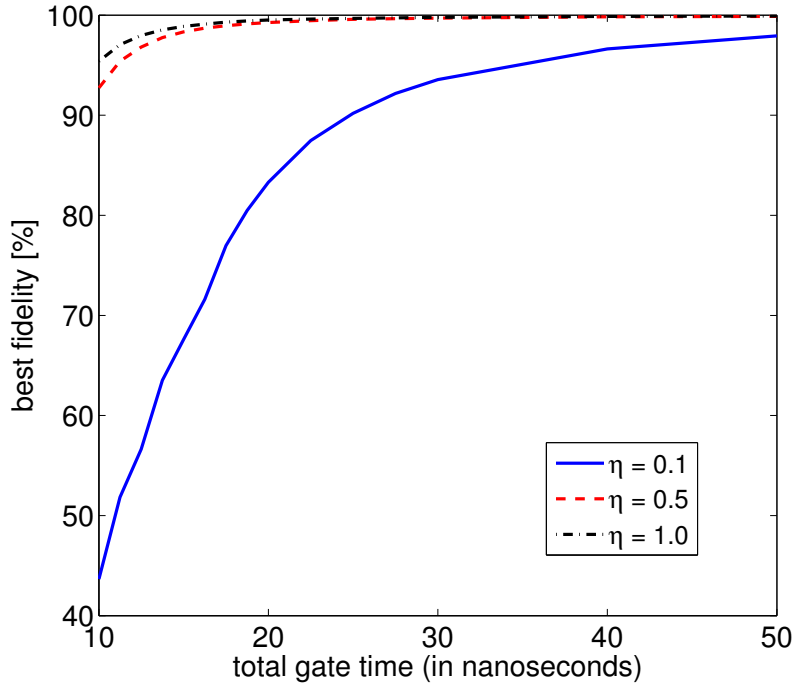


**Figure 2.1:** (Color online) Plot of optimal fidelity versus total gate time, averaged over randomly generated interactions with fixed values of  $\eta$ , for  $\eta = 0.1, 0.5$ , and  $1.0$ .

on  $x$  axis. (The actual point reached depends on the sign of  $J$ .) The time it takes to do this—neglecting the time needed for the  $\pi$  pulse—is  $2\Delta t$  [see (2.15)], or  $\pi\hbar/4g\eta$ . Including all the single-qubit rotations in (2.16) leads to a total gate time of

$$t_{\text{gate}} = \frac{\pi\hbar}{4g\eta} + \frac{3\pi + 2\varphi}{\Omega}. \quad (2.19)$$

Because the first term in (2.19) is inversely proportional to  $\eta g$ , for a fixed gate time a larger value of coupling strength  $g$  is required when  $\eta$  is small. But when  $g$  increases the assumption of weak coupling used in [37] is violated and the corrections to the rotating-wave-approximation get larger. Furthermore, that large coupling leads to considerable errors during the single-qubit operations because the qubit-qubit interaction is not switched off.

## 2.2.2 Conditional spectroscopic approach <sup>1</sup>

Spectroscopic CNOT gate has been demonstrated by Plantenberg *et al.* for a pair of superconducting flux qubits [39]. Here, I first review the spectroscopic approach for a qubit-resonator system and then describe how to improve its fidelity so as to be competitive with other existing approaches.

The idea behind a spectroscopic CNOT gate is simple and has a wide range of applicability: A  $\pi$  pulse is applied to the target qubit with a carefully selected carrier frequency (the frequency of the microwave drive attached with the qubit). The carrier frequency is close to the qubit transition frequency given that the attached control resonator is in the “on” or  $|1\rangle$  state, which in the  $|qr\rangle$  basis is

$$\omega_{\text{on}} \equiv \frac{E_{11} - E_{01}}{\hbar}, \quad (2.20)$$

where  $E_{ij}$  is the energy of the eigenstate  $|ij\rangle$ . The Rabi frequency has to be smaller than the detuning to the “off” transition at

$$\omega_{\text{off}} \equiv \frac{E_{10} - E_{00}}{\hbar}. \quad (2.21)$$

A direct  $\sigma^z \otimes \sigma^z$  coupling between the devices would of course generate a difference in  $\omega_{\text{on}}$  and  $\omega_{\text{off}}$ , but in the qubit plus resonator system—which has no direct  $\sigma^z \otimes \sigma^z$  coupling—such an interaction is generated by level repulsion from the noncomputational  $|2\rangle$  states. The difference  $|\omega_{\text{on}} - \omega_{\text{off}}|$  characterizes the sensitivity of the conditioning effect and determines the speed of the resulting gate. When the qubit and resonator are detuned by an amount larger than the coupling between them, they become weakly coupled. In this limit, the sensitivity for current devices is limited to a few MHz, which is not sufficient for practical application. Therefore to amplify the sensitivity we adiabatically bring the target qubit to

---

<sup>1</sup>J. Ghosh and M. R. Geller, *Quantum Information Processing*, Springer, Netherlands, **11**, 6, 1349-57 (2012) [Copyrighted material reprinted in this section as per license agreement with the publisher].

a suitable point near resonance with the control resonator, and drive the qubit while it is strongly coupled with the resonator. After performing a  $\pi$  pulse the qubit is adiabatically detuned from the resonator.

Two main sources of intrinsic errors exist in this approach: Although we set the carrier frequency to a value such that we have a  $\pi$  pulse in the qubit when the resonator is in  $|1\rangle$ , there is a small probability for the qubit to get rotated even if the resonator is in  $|0\rangle$ . The second error comes from the fact that, since we are driving the qubit, it is possible to have leakage to the qubit  $|2\rangle$  state. The fidelity will reach its maximum value when both of these errors are minimized simultaneously. We use the DRAG method [10] to suppress the error due to leakage and adjust all other parameters by optimization.

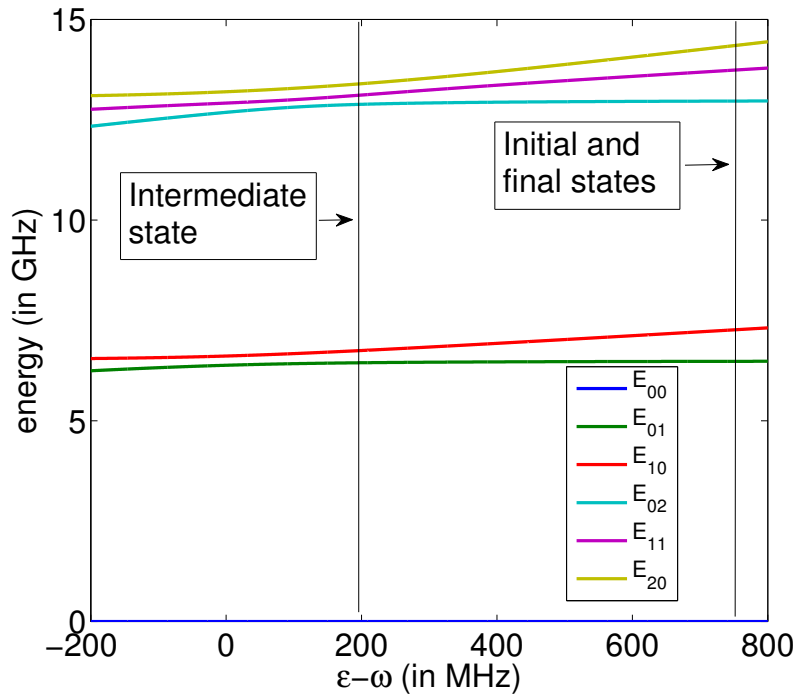


**Figure 2.2:** (Color online) A plot of first six energy levels of a qubit coupled to a resonator at  $g/h = 115$  MHz.

In the basis of uncoupled qubits, the Hamiltonian of a qubit capacitively coupled to a

resonator (assuming harmonic eigenfunction of 2-states) is given by (suppressing  $\hbar$ ),

$$H = H_0 + H_{\text{rf}} + H_{\text{int}}, \quad (2.22)$$

where,

$$H_0 = \begin{pmatrix} 0 & 0 & 0 \\ 0 & \epsilon & 0 \\ 0 & 0 & 2\epsilon - \Delta \end{pmatrix}_q + \begin{pmatrix} 0 & 0 & 0 \\ 0 & \omega & 0 \\ 0 & 0 & 2\omega \end{pmatrix}_r$$

$$H_{\text{rf}} = \Omega(t) \cos(\omega_{\text{rf}}(t) t + \phi(t)) \begin{pmatrix} 0 & 1 & 0 \\ 1 & 0 & \sqrt{2} \\ 0 & \sqrt{2} & 0 \end{pmatrix}_q \quad (2.23)$$

$$H_{\text{int}} = g \begin{pmatrix} 0 & -i & 0 \\ i & 0 & -\sqrt{2}i \\ 0 & \sqrt{2}i & 0 \end{pmatrix}_q \otimes \begin{pmatrix} 0 & -i & 0 \\ i & 0 & -\sqrt{2}i \\ 0 & \sqrt{2}i & 0 \end{pmatrix}_r,$$

where,  $\epsilon$ ,  $\omega$  and  $\Delta$  are qubit frequency, resonator frequency, and anharmonicity of the qubit, respectively.  $\Omega$ ,  $\omega_{\text{rf}}$  and  $\phi$  are Rabi frequency, carrier frequency, and phase of the microwave pulse.  $g$  is the (time-independent) interaction strength between qubit and resonator. The first six energy levels of the system (obtained numerically) are shown in Fig. 2.2. We use coupling  $g/h=115$  MHz, resonator frequency  $\omega/h = 6.5$  GHz and anharmonicity of the qubit  $\Delta/h = 200$  MHz. The simulations discussed below are carried out in a frame rotating with the instantaneous frequency of the qubit.

Eigenstates of the full Hamiltonian reduce to the eigenstates of the uncoupled Hamiltonian far away from the resonance. We denote the first six eigenstates of the full Hamiltonian by  $E_{00}, E_{01}, E_{10}, E_{02}, E_{11}, E_{20}$  and define a conditional control sensitivity  $S_c$  and leakage sen-

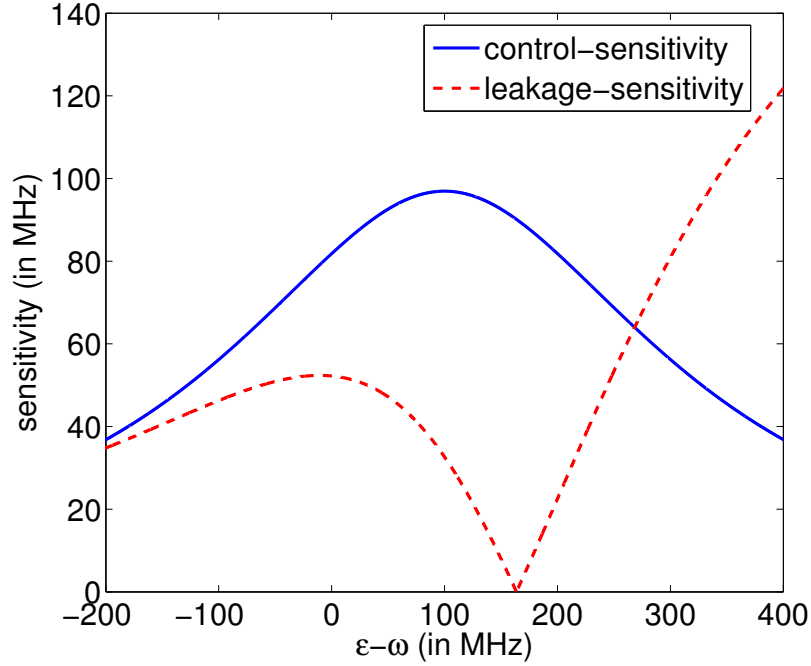


**Figure 2.3:** (Color online) A plot of control and leakage sensitivity vs. qubit frequency for  $g/h = 115$  MHz.

sensitivity  $S_l$  as

$$\begin{aligned}
 S_c &\equiv |(E_{11} - E_{01}) - (E_{10} - E_{00})|, \\
 S_l &\equiv |(E_{21} - E_{11}) - (E_{11} - E_{01})|.
 \end{aligned}
 \tag{2.24}$$

The conditional control sensitivity is the (magnitude of the) difference between  $\omega_{\text{on}}$  and  $\omega_{\text{off}}$ . Leakage sensitivity is the anharmonicity of the target qubit when control resonator is on. In order to achieve a high fidelity both of these quantities need to be maximized (by varying the detuning  $\epsilon - \omega$ ). A plot of these sensitivities is shown in Fig. 2.3. Peaks in the control sensitivity (resulting from expected anticrossings) at detuning equal to zero and  $\Delta$  conspire to give the maximum at 100 MHz detuning shown in the blue curve of Fig. 2.3. Operating near 100 MHz detuning, however, leads to poor performance because of the large leakage error there. Better operation points exist near -100 and 200 MHz detuning; we shall make

use of the latter. Fig. 2.4 shows the behavior of sensitivities vs. coupling at  $(\epsilon - \omega)/h = 215$  MHz.

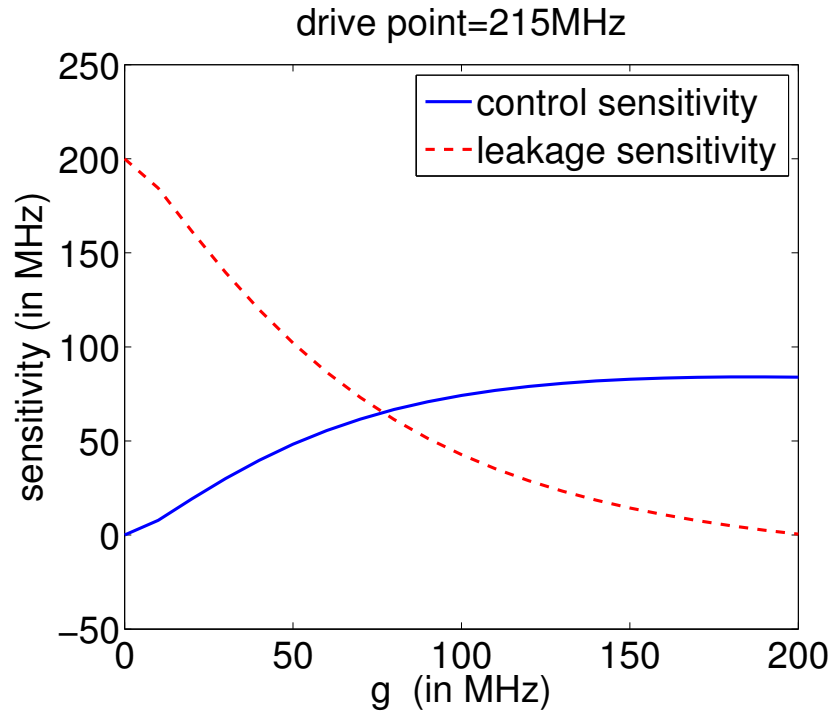


**Figure 2.4:** (Color online) A plot of control and leakage sensitivity vs. coupling.

To implement a CNOT gate we begin with a strongly detuned qubit-resonator system. Then the qubit is adiabatically tuned into resonance with the resonator, driven with a  $\pi$  pulse, and finally detuned. In the  $|qr\rangle$  basis this protocol ideally produces

$$U_{\text{target}} = \begin{bmatrix} 1 & 0 & 0 & 0 \\ 0 & 0 & 0 & 1 \\ 0 & 0 & 1 & 0 \\ 0 & 1 & 0 & 0 \end{bmatrix} = \text{SWAP} \times \text{CNOT} \times \text{SWAP}, \quad (2.25)$$

where

$$\text{SWAP} \equiv \begin{bmatrix} 1 & 0 & 0 & 0 \\ 0 & 0 & 1 & 0 \\ 0 & 1 & 0 & 0 \\ 0 & 0 & 0 & 1 \end{bmatrix} \quad (2.26)$$

is the swap gate. To obtain this target we also perform  $z$  rotations on the qubit before and after the sequence described above, with angles determined by optimizations.

As far as leakage outside the computational subspace is concerned, we can consider  $E_{01}$ ,  $E_{11}$  and  $E_{21}$  to be a single 3-level quantum system where we are interested in local rotations between the first two levels and therefore, in order to suppress the errors due to leakage to the third level, local rotations are performed with a DRAG pulse [10], up to 5<sup>th</sup> order. In order to do a local rotation of angle  $\theta$  about the  $x$  axis, we set the Rabi pulse of the Hamiltonian to be

$$\begin{aligned} \Omega(t) \cos(\phi(t)) &= f_\theta + \frac{(\lambda^2-4)f_\theta^3}{8\Delta^2} - \frac{(13\lambda^4-76\lambda^2+112)f_\theta^5}{128\Delta^4}, \\ \Omega(t) \sin(\phi(t)) &= -\frac{\dot{f}_\theta}{\Delta} + \frac{33(\lambda^2-2)f_\theta^2\dot{f}_\theta}{24\Delta^3}, \\ \omega_{\text{rf}}(t) &= \omega_c + \frac{(\lambda^2-4)f_\theta^2}{4\Delta} - \frac{(\lambda^4-7\lambda^2+12)f_\theta^4}{16\Delta^3}, \end{aligned} \quad (2.27)$$

where,  $\lambda$  is the ratio between the coupling strengths in double excitation subspace and single excitation subspace and assumed to be equal to  $\sqrt{2}$  under harmonic eigenfunction approximation. The first two equations give the amplitudes of  $\cos(\omega_{\text{rf}}t)$  and  $\sin(\omega_{\text{rf}}t)$  quadratures. Here  $\omega_c$  is found via optimization around  $|E_{01}-E_{11}|$  and  $f_\theta(t)$  is chosen to be a Gaussian function (vertically shifted) such that  $f_\theta(0) = f_\theta(t_g) = 0$  and  $\int_0^{t_g} f_\theta(t)dt = \theta$ ,  $t_g$  being the time required to perform the local rotation.

Fig. 2.5 shows the fidelity curve obtained from optimization and Table 2.2 shows corre-

**Table 2.2:** Optimum values of parameters for CNOT gate.

$t_{\text{gate}}$ (ns.)	$t_{\text{ramp}}$ (ns.)	$g$ (MHz)	$\epsilon - \omega$ (MHz)	Fidelity[%]
33	7.1	118.5966	235.1804	92.4021
35	7.3	107.5055	218.8692	97.2223
37	7.0	123.8367	237.4236	96.4515
39	7.3	113.2576	217.7214	98.7965
41	7.4	107.7414	218.2388	98.5218
43	7.2	117.6687	218.6669	98.5886
45	7.5	107.3625	199.2662	99.3914
47	7.5	104.0402	204.6788	99.2326
49	7.3	113.8836	208.3964	99.1864
51	7.5	107.6466	202.2407	99.3836

sponding coupling strengths, duration of each ramp and driving points. Our result shows that the intrinsic fidelity can be pushed to 99% within 45 ns gate time. The remaining error comes from the adiabaticity of the ramp pulses and leakage outside the computational basis states, for example between  $|11\rangle$  and  $|20\rangle$  (in  $|qr\rangle$  basis) at driving point where  $\epsilon \approx \omega + \Delta$ .

As an example, we show the change of qubit frequency (in GHz) over time (in nanoseconds) in Fig. 2.6 for the CNOT having total gate time = 45 ns. while the resonator frequency is always fixed at 6.5 GHz and pre and post  $\sigma^z$ -rotation angles are found to be  $\vartheta_{\text{post}} = -1.0915$  and  $\vartheta_{\text{pre}} = 0.5442$  radian for this case. We use linear pulse for ramps and a gaussian envelope is used for DRAG.

We have computed intrinsic fidelity of a CNOT gate based on conditional spectroscopy approach and have shown that it is possible to achieve greater than 99% fidelity within an experimentally practical time scale of 45 ns. However, this design requires a large coupling strength, so tunable coupling would probably be required in a multi-qubit system. Although our analysis assumed a qubit and resonator, the design also applies to capacitively cou-

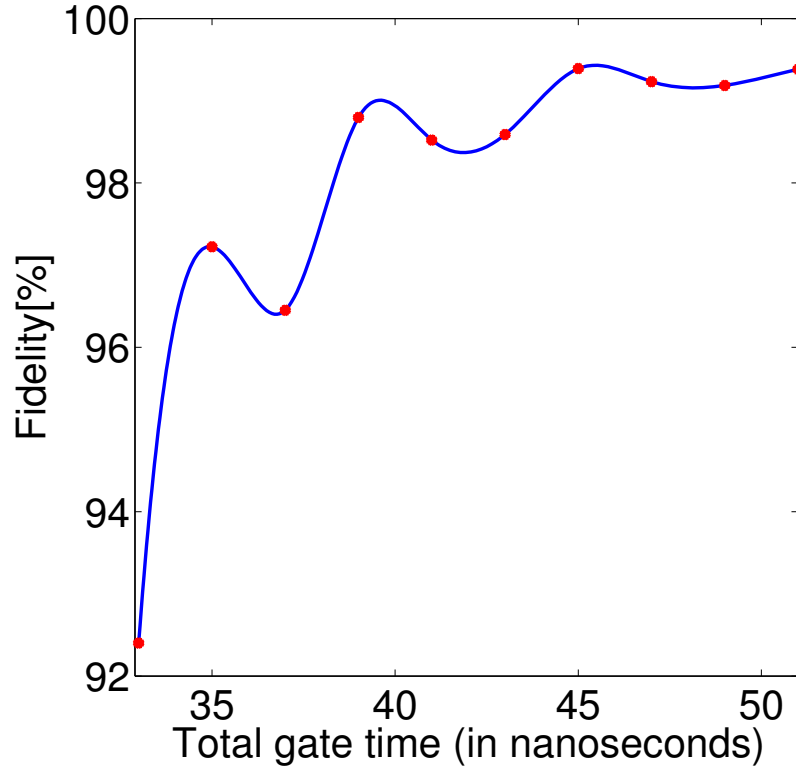


**Figure 2.5:** (Color online) A plot of fidelity vs. total gate time in nanoseconds. Red points are obtained via optimization and the blue line is an interpolation.

pled qubits, where a slightly higher fidelity would be expected because of the additional anharmonicity.

## 2.3 Controlled- $\sigma^z$ gate for qubit-resonator model <sup>1</sup>

In this section, I first review the existing approaches of designing a CZ gate, and then develop a unified theory of anticrossing-based CZ gate protocol for a qubit-resonator system. The anticrossing-based CZ gate was first proposed by Strauch *et al.* in the sudden regime [16],

<sup>1</sup>J. Ghosh, A. Galiutdinov, Z. Zhou, A. N. Korotkov, J. M. Martinis, and M. R. Geller, *Physical Review A* **87**, 022309 (2013) [Copyrighted material reprinted in this section as per transfer of copyright agreement with the publisher].

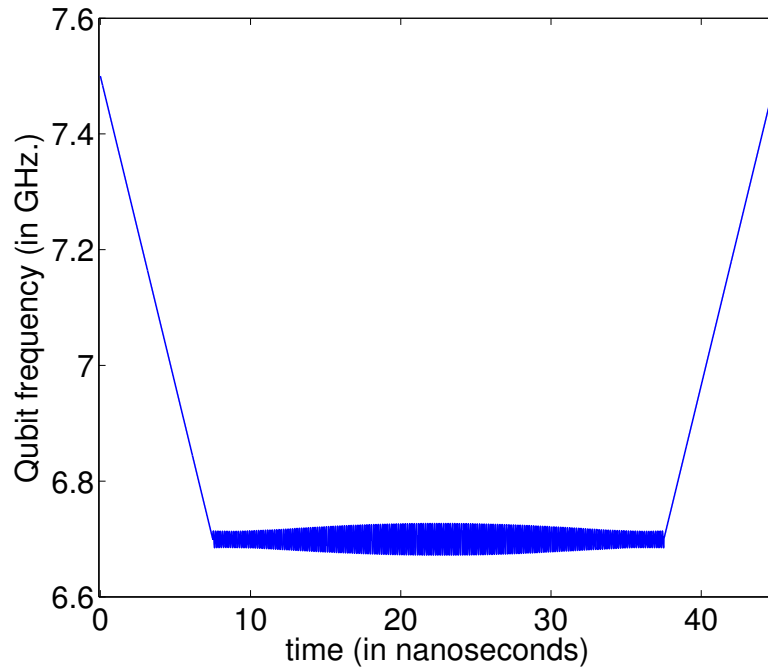


**Figure 2.6:** (Color online) A plot of qubit frequency vs. time for CNOT at total gate time=45 ns.

as well as demonstrated by DiCarlo *et al.* in the adiabatic regime [40]. While I discuss the CZ gate for a multi-qubit architecture, for instance the *quantum von Neumann* (QVN) architecture [41], in detail in the next section, I sometimes refer to it here especially in the context of ‘eigenstate basis’, ‘local clocks’, and ‘auxiliary z rotation’. For the convenience of readers, I show the schematic diagram of 4-qubit QVN (QVN<sub>4</sub> in short) in Fig. 2.7 and give the values of various parameters in Table. 2.3. An  $n$ -qubit QVN (denoted by QVN <sub>$n$</sub> ) consists of  $n$  superconducting qubits, each capacitively coupled to its own memory resonator (shown by  $m_i$  in Fig. 2.7) as well as a common bus resonator (denoted by  $b$ ). A detailed description of this architecture is given in Sec. 2.4.

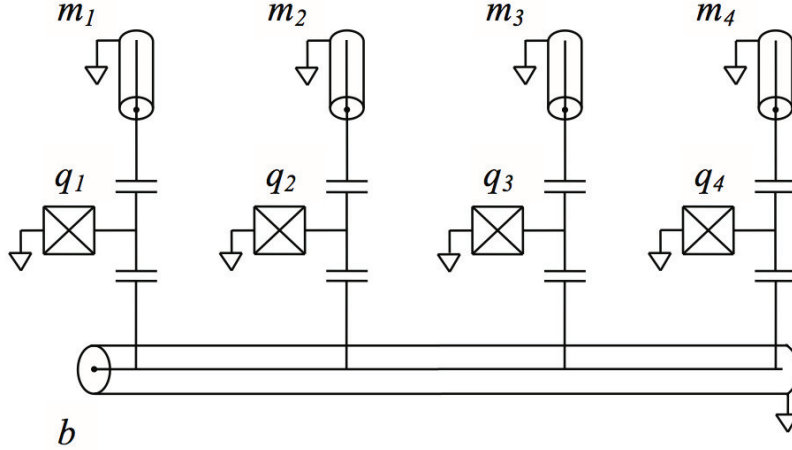


**Figure 2.7:** Layout of the four-qubit QVN processor. The  $q_i$  represent superconducting qubits capacitively coupled to memory resonators  $m_i$  as well as a resonator bus  $b$ .

### 2.3.1 A review of existing protocols

Here, I review the anticrossing-based CZ gate protocols in both sudden and adiabatic regimes. To accomplish this we introduce several approximations that allow for an analytic treatment of the CZ gate dynamics.

First, we consider a truncated model consisting of a single superconducting qubit with frequency  $\epsilon$  and anharmonic detuning  $\eta$ , capacitively coupled to a bus resonator with frequency  $\omega_b$ ,

$$H = \begin{pmatrix} 0 & 0 & 0 \\ 0 & \epsilon & 0 \\ 0 & 0 & 2\epsilon - \eta \end{pmatrix}_q + \begin{pmatrix} 0 & 0 & 0 \\ 0 & \omega_b & 0 \\ 0 & 0 & 2\omega_b \end{pmatrix}_b + g_b Y_q \otimes Y_b. \quad (2.28)$$

In this case  $Y$  reduces to

$$Y = \begin{pmatrix} 0 & -i & 0 \\ i & 0 & -\sqrt{2}i \\ 0 & \sqrt{2}i & 0 \end{pmatrix}. \quad (2.29)$$

**Table 2.3:** Device parameters used for QVN<sub>4</sub> architecture.

quantity	value
empty qubit parking frequency $\omega_{\text{park}}/2\pi$	10.0 GHz
memory resonator $m_1$ frequency $\omega_{m1}/2\pi$	8.3 GHz
memory resonator $m_2$ frequency $\omega_{m2}/2\pi$	8.2 GHz
memory resonator $m_3$ frequency $\omega_{m3}/2\pi$	8.1 GHz
memory resonator $m_4$ frequency $\omega_{m4}/2\pi$	8.0 GHz
initial detuned qubit frequency $\omega_{\text{off}}/2\pi$	7.5 GHz
bus resonator frequency $\omega_{\text{b}}/2\pi$	6.5 GHz
qubit-memory coupling strength $g_{\text{m}}/2\pi$	100 MHz
qubit-bus coupling strength $g_{\text{b}}/2\pi$	30 – 60 MHz
qubit anharmonicity $\eta/2\pi$	200 – 400 MHz

This Hamiltonian is written in the basis of *bare* eigenstates, which are the system eigenfunctions when the qubit and resonator are uncoupled. We write these bare states as  $|qb\rangle$ , with  $q, b \in \{0, 1, 2\}$ . The energies of the interacting eigenstates, which we write with an overline as  $\overline{|qb\rangle}$ , are plotted in Fig. 2.8 as a function of  $\epsilon/2\pi$  for the case of  $\omega_{\text{b}}/2\pi = 6.5$  GHz,  $\eta/2\pi = 300$  MHz, and  $g_{\text{b}}/2\pi = 45$  MHz. The interacting eigenstates are labeled such that  $\overline{|qb\rangle}$  is perturbatively connected to  $|qb\rangle$  when  $\epsilon \gg \omega_{\text{b}}$ .

Second, we assume a short switching time and ignore the dynamical phases acquired during the ramps. As we will see below, this approximation is valid when  $g_{\text{b}} \ll \eta$ , so that the switching can be made *sudden* with respect to the coupling  $g_{\text{b}}$ , but still adiabatic with respect to the anharmonicity  $\eta$ .

The CZ gate of Strauch *et al.* [16], adapted to the qubit-resonator system, works by using the anticrossing of the  $\overline{|11\rangle}$  channel with the auxiliary state  $\overline{|20\rangle}$ . In terms of the pulse parameters, the qubit-resonator state is prepared at a off-resonance qubit frequency  $\epsilon = \omega_{\text{off}}$ , and the frequency is then switched to  $\epsilon = \omega_{\text{on}}$  for a FWHM time duration  $t_{\text{on}}$  (described

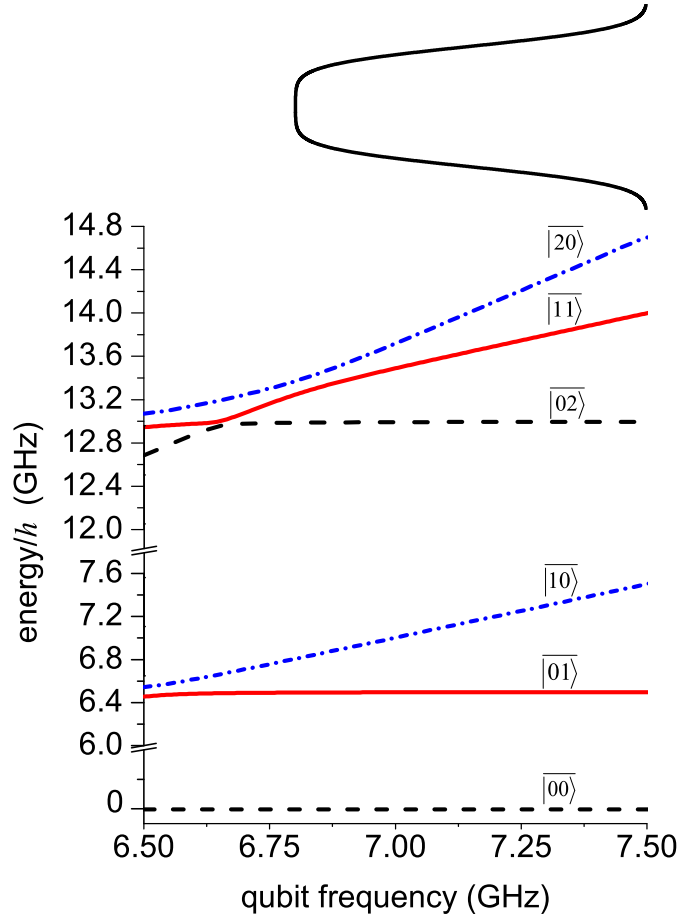


**Figure 2.8:** (Color online) Energies of eigenstates  $|qb\rangle$  of a single qubit  $q$  coupled to a resonator bus  $b$ . Here  $\omega_b/2\pi = 6.5$  GHz,  $\eta/2\pi = 300$  MHz, and  $g_b/2\pi = 45$  MHz. The time dependence of the qubit frequency during a CZ gate (solid black curve) is indicated at the top of the figure.

below in detail). In the simplified model considered in this section,

$$\omega_{\text{on}} = \omega_b + \eta, \quad (2.30)$$

and

$$t_{\text{on}} = \frac{\pi}{\sqrt{2}g_b}. \quad (2.31)$$

Equation (2.30) gives the qubit frequency for which the bare state  $|11\rangle$  is degenerate with  $|20\rangle$ , and is at a frequency  $\eta$  above the usual resonance condition. Equation (2.31) is the sudden-limit value, derived below. The qubit frequency is then returned to the detuned value  $\omega_{\text{off}}$ . The complete pulse profile is also shown in Fig. 2.8 (solid black curve) for the case of  $\omega_{\text{on}}/2\pi = 6.8$  GHz and  $\omega_{\text{off}}/2\pi = 7.5$  GHz.

Let's follow the evolution resulting from an initial (normalized) qubit-resonator state

$$a_{00}|\overline{00}\rangle + a_{01}|\overline{01}\rangle + a_{10}|\overline{10}\rangle + a_{11}|\overline{11}\rangle. \quad (2.32)$$

Because the  $|\overline{00}\rangle$  channel is very well separated from the others, the  $|\overline{00}\rangle$  component will only acquire a dynamical phase factor

$$e^{-iE_{00}t_{\text{gate}}}, \quad (2.33)$$

where  $E_{00}$  is the energy of the  $|\overline{00}\rangle$  eigenstate. Without loss of generality we can shift the entire spectrum so that  $E_{00} = 0$  [as in (2.28)] and the phase factor (2.33) becomes unity. This freedom results from the fact that any unitary gate operation only needs to be defined up to an overall multiplicative phase factor. With this phase convention the CZ gate acts as the identity on this component, so we have the map

$$|\overline{00}\rangle \rightarrow |\overline{00}\rangle. \quad (2.34)$$

The  $|\overline{01}\rangle$  component will mostly return to  $|\overline{01}\rangle$ , also with an acquired phase, but a small component will be left in  $|\overline{10}\rangle$  due to the nonadiabatic excitation of that channel, which is only separated in energy from  $|\overline{01}\rangle$  by about  $\eta$  when  $\epsilon = \omega_b + \eta$ . The  $|\overline{10}\rangle$  component similarly suffers from a small nonadiabatic coupling to  $|\overline{01}\rangle$ . As we will explain below, these nonadiabatic errors are exponentially suppressed when the functional form of  $\epsilon(t)$  is properly

designed. Then we have

$$|\overline{01}\rangle \rightarrow e^{-i\alpha} \sqrt{1 - \mathbb{E}_1} |\overline{01}\rangle + e^{-i\alpha'} \sqrt{\mathbb{E}_1} |\overline{10}\rangle \quad (2.35)$$

and

$$|\overline{10}\rangle \rightarrow e^{-i\beta} \sqrt{1 - \mathbb{E}_1} |\overline{10}\rangle + e^{-i\beta'} \sqrt{\mathbb{E}_1} |\overline{01}\rangle, \quad (2.36)$$

where  $\mathbb{E}_1$  is a small nonadiabatic population error (below we refer to  $\mathbb{E}_1$  as a *switching* error).

In the  $\mathbb{E}_1 \rightarrow 0$  limit,  $\alpha$  and  $\beta$  are dynamical phases given by

$$\alpha = \int_0^{t_{\text{gate}}} E_{01} dt \approx \left( \omega_b - \frac{g_b^2}{\eta} \right) t_{\text{on}}, \quad (2.37)$$

$$\beta = \int_0^{t_{\text{gate}}} E_{10} dt \approx \left( \omega_b + \eta + \frac{g_b^2}{\eta} \right) t_{\text{on}}, \quad (2.38)$$

where the second approximate quantities neglect phase accumulation during the ramps and use perturbative expressions for the energies  $E_{01}$  and  $E_{10}$  when  $\epsilon = \omega_b + \eta$ . The expressions (2.35) and (2.36) neglect an extremely small leakage out of the  $\{|\overline{01}\rangle, |\overline{10}\rangle\}$  subspace. Neglecting this leakage, the evolution in the  $\{|\overline{01}\rangle, |\overline{10}\rangle\}$  subspace is unitary, leading to the phase condition

$$e^{i(\alpha - \beta')} + e^{i(\alpha' - \beta)} = 0. \quad (2.39)$$

Using (2.39) to eliminate  $\beta'$  leads to

$$|\overline{01}\rangle \rightarrow e^{-i\alpha} \sqrt{1 - \mathbb{E}_1} |\overline{01}\rangle + e^{-i(\beta + \phi)} \sqrt{\mathbb{E}_1} |\overline{10}\rangle, \quad (2.40)$$

$$|\overline{10}\rangle \rightarrow e^{-i\beta} \sqrt{1 - \mathbb{E}_1} |\overline{10}\rangle - e^{-i(\alpha - \phi)} \sqrt{\mathbb{E}_1} |\overline{01}\rangle, \quad (2.41)$$

where  $\phi \equiv \alpha' - \beta$ . The evolution of the eigentates  $|\overline{01}\rangle$  and  $|\overline{10}\rangle$  is therefore characterized by the cross-excitation probability  $\mathbb{E}_1$  and three phase angles  $\alpha$ ,  $\beta$ , and  $\phi$ .

Now we consider the  $\overline{|11\rangle}$  component. The  $\overline{|11\rangle}$  channel couples strongly with the  $\overline{|20\rangle}$  channel, as well as weakly with  $\overline{|02\rangle}$ . The simplest way to understand the dynamics of the  $\overline{|11\rangle}$  component is to use two different representations to describe these two effects. We will describe strong interaction with  $\overline{|20\rangle}$  in the bare basis and the weak, nonadiabatic coupling with  $\overline{|02\rangle}$  in the eigenstate basis. Suppose we begin with the qubit strongly detuned from the bus, so that  $\overline{|11\rangle} \approx |11\rangle$  (the detuned interacting eigenstate is well approximated by the bare  $|11\rangle$  state). Then we quickly switch  $\epsilon$  from  $\omega_{\text{off}}$  to  $\omega_b + \eta$ . By “quickly” we mean that we strongly mix with the  $\overline{|20\rangle}$  channel. The interaction with  $\overline{|02\rangle}$  is always weak, even in the sudden limit. This asymmetric excitation is possible because  $\overline{|20\rangle}$  is protected (separated in energy from  $\overline{|11\rangle}$ ) by an energy gap  $2\sqrt{2}g_b$ , whereas  $\overline{|02\rangle}$  is protected by a much larger gap of  $\eta - \sqrt{2}g_b$  (this expression accounts for level repulsion from  $\overline{|20\rangle}$ , and we have assumed that  $g_b \ll \eta$ ). We can informally say that the desired switching is nonadiabatic with respect to the energy scale  $g_b$ , but is adiabatic with respect to  $\eta$  [16].

Focusing first on the strong coupling to  $\overline{|20\rangle}$ , the suddenly switched  $|11\rangle$  state is no longer an eigenstate when  $\epsilon = \omega_{\text{on}}$ , as the relevant eigenfunctions at this setting are

$$\overline{|11\rangle} = \frac{|11\rangle - |20\rangle}{\sqrt{2}} \quad \text{and} \quad \overline{|20\rangle} = \frac{|11\rangle + |20\rangle}{\sqrt{2}}. \quad (2.42)$$

The nonstationary state

$$|11\rangle = \frac{\overline{|11\rangle} + \overline{|20\rangle}}{\sqrt{2}} \quad (2.43)$$

therefore rotates in the  $\{|11\rangle, |20\rangle\}$  subspace, and after a time duration  $t$  becomes

$$|\psi\rangle = e^{-iE_{11}t} \left[ \frac{\overline{|11\rangle} + e^{-i\Delta Et}\overline{|20\rangle}}{\sqrt{2}} \right] \quad (2.44)$$

$$= e^{-iE_{11}t} \left[ \left( \frac{1 + e^{-i\Delta Et}}{2} \right) |11\rangle - \left( \frac{1 - e^{-i\Delta Et}}{2} \right) |20\rangle \right], \quad (2.45)$$

where

$$\Delta E \equiv E_{20} - E_{11} = 2\sqrt{2}g_b. \quad (2.46)$$

Holding  $\epsilon$  fixed at  $\omega_b + \eta$  for a FWHM time (2.31), corresponding to a  $2\pi$  rotation, (2.45) becomes

$$|\psi\rangle = e^{-iE_{11}t_{\text{on}}}|11\rangle. \quad (2.47)$$

When  $\epsilon = \omega_b + \eta$ , the energy of eigenstate  $|\overline{11}\rangle$  is

$$E_{11} = 2\omega_b + \eta - \sqrt{2}g_b. \quad (2.48)$$

After detuning quickly we therefore obtain

$$|\overline{11}\rangle \rightarrow -\exp\left[-i\left(\pi\frac{2\omega_b + \eta}{\sqrt{2}g_b}\right)\right]|\overline{11}\rangle, \quad (2.49)$$

or, using expressions (2.37) and (2.38),

$$|\overline{11}\rangle \rightarrow -e^{-i(\alpha+\beta)}|\overline{11}\rangle. \quad (2.50)$$

The two phase angles  $\alpha$  and  $\beta$  can be cancelled by the application of independent auxiliary single-qubit  $z$  rotations

$$R_z(\gamma) \equiv \exp[-i(\gamma/2)\sigma^z] \quad (2.51)$$

to the qubit and bus. Qubit  $z$  rotations are implemented by frequency excursions, whereas resonator  $z$  rotations are implemented in software (they are compiled into future qubit rotations). Following the pulse sequence that leads to (2.34), (2.40), (2.41), and (2.50), with the operation

$$R_z(\gamma_1) \otimes R_z(\gamma_2), \quad (2.52)$$

where

$$\gamma_1 = -\beta \quad \text{and} \quad \gamma_2 = -\alpha, \quad (2.53)$$

leads to the map

$$\overline{|00\rangle} \rightarrow \overline{|00\rangle}, \quad (2.54)$$

$$\overline{|01\rangle} \rightarrow \sqrt{1 - \mathbb{E}_1} \overline{|01\rangle} + e^{-i\phi} \sqrt{\mathbb{E}_1} \overline{|10\rangle}, \quad (2.55)$$

$$\overline{|10\rangle} \rightarrow \sqrt{1 - \mathbb{E}_1} \overline{|10\rangle} - e^{i\phi} \sqrt{\mathbb{E}_1} \overline{|01\rangle}, \quad (2.56)$$

$$\overline{|11\rangle} \rightarrow -\overline{|11\rangle}, \quad (2.57)$$

apart from a global phase factor. The use of auxiliary  $z$  rotations is discussed further Sec. 2.3.3.

The minus sign in (2.57) is the key to the Strauch CZ gate. However, as mentioned above, the analysis leading to (2.57) neglected a weak nonadiabatic excitation of the  $\overline{|02\rangle}$  channel caused by the switching of  $\epsilon$ . Including this effect in (2.57) leads to the modification

$$\overline{|11\rangle} \rightarrow -\sqrt{1 - \mathbb{E}_2} \overline{|11\rangle} + \text{phase factor} \times \sqrt{\mathbb{E}_2} \overline{|02\rangle}, \quad (2.58)$$

where  $\mathbb{E}_2$  is another switching error. Both  $\mathbb{E}_1$  and  $\mathbb{E}_2$  vanish exponentially with  $\sigma$  (or  $t_{\text{ramp}}$ ), and for the regimes studied in this work  $\mathbb{E}_2$  is the dominant source of intrinsic gate fidelity loss. We note that the analysis leading to (2.58) assumed implementation of the *ideal* values [(2.30) and (2.31)] of  $\omega_{\text{on}}$  and  $t_{\text{on}}$ . Errors in these two control parameters, which we refer to as pulse shape errors and study in Sec. 2.3.7, lead instead to

$$\overline{|11\rangle} \rightarrow -e^{i\delta} \sqrt{1 - \mathbb{E}_2 - \mathbb{E}_\theta} \overline{|11\rangle} + \text{phase factor} \times \sqrt{\mathbb{E}_2} \overline{|02\rangle} + \text{phase factor} \times \sqrt{\mathbb{E}_\theta} \overline{|20\rangle}, \quad (2.59)$$

where the controlled-phase error angle  $\delta$  and rotation error  $\mathbb{E}_\theta$  depend on the errors in  $\omega_{\text{on}}$  and  $t_{\text{on}}$ , respectively.

Finally, it is also interesting to consider the fully adiabatic limit of the Strauch CZ gate. By this we mean that the switching is adiabatic with respect to both  $g_b$  and  $\eta$ . For the gate time to be competitive with the nonadiabatic gate, a larger coupling  $g_b$  is required, which might lead to significant higher-order and cross-coupling errors in a multi-qubit device, but in the fully adiabatic limit only *one* pulse control parameter—either  $\omega_{\text{on}}$  or  $t_{\text{on}}$ —needs to be optimized (two  $z$  rotations are still required). This is because adiabaticity now assures that the  $\overline{|11\rangle}$  population is preserved (apart from exponentially small switching errors), taking over the role previously played by  $t_{\text{on}}$ , and a single pulse shape parameter is sufficient to specify the controlled phase. A highly adiabatic CZ gate was demonstrated in Ref. [40].

There are a few important differences between the Strauch CZ gate applied to a pair of directly coupled qubits (as in Ref. [16]) and to the qubit-bus system considered here. These differences result from the harmonic spectrum of the resonator in the latter case and are discussed below in Sec. 2.3.8.

### 2.3.2 Gate design in eigenstate basis

The Hamiltonian (2.28) is written in the usual *bare* basis of uncoupled system eigenstates, but information processing itself is best performed in the basis of *interacting* eigenfunctions of  $H_{\text{idle}}$ , where  $H_{\text{idle}}$  is given by (2.28) with the qubits in a dispersive idling configuration [42]. This choice of computational basis assures that idling qubits suffer no population change in the decoherence-free limit, and evolve in phase in a way that can be almost exactly compensated for by an appropriate choice of rotating frames or local clocks, one for each qubit [42]. Here I briefly review this important concept.

In principal, any complete orthonormal basis of the physical Hilbert space that can be appropriately prepared, unitarily transformed, and measured—essentially, any basis where

one can implement the DiVincenzo criteria [8]—is a valid basis on which to run a quantum computation. Defining the computational states to be interacting system eigenfunctions gives them the simplifying property that the time evolution can be decomposed into a sequence of gates, between which (almost) no evolution occurs. In other words, idling between gates generates the identity operation. This property, which is implicitly assumed in the standard circuit model of quantum computation, could be realized in an architecture where the Hamiltonian  $H$  can be completely switched off between gates. However, it is not possible to set  $H = 0$  in a QVN architecture; nor can  $H$  itself be made negligibly small between gates. Therefore, nonstationary states such as uncoupled-qubit eigenstates accumulate errors (including population oscillations) between gates unless a correction protocol such as dynamical decoupling [43] is used. By defining computational states in terms of interacting system eigenfunctions  $\{|\psi\rangle\}$  at some predefined dispersive idling configuration (qubit frequencies), the only evolution occurring during an idle from time  $t_1$  to  $t_2$  is a pure phase evolution,

$$\overline{|\psi(t_1)\rangle} \rightarrow \overline{|\psi(t_2)\rangle} = e^{-iE(t_2-t_1)}\overline{|\psi(t_1)\rangle}, \quad (2.60)$$

where  $E$  is the exact energy eigenvalue (and we neglect decoherence). Furthermore, it is possible to *compensate* for—or effectively remove—the pure phase evolution in (2.60) by applying phase shifts (after the idle period) to each eigenfunction to cancel the  $e^{-iE(t_2-t_1)}$  phase factors; doing so would result in the ideal between-gate evolution

$$\overline{|\psi(t_1)\rangle} \rightarrow \overline{|\psi(t_2)\rangle} = \overline{|\psi(t_1)\rangle}. \quad (2.61)$$

The idling dynamics (2.61) is evidently equivalent to setting  $H = 0$  between gates. We will discuss below how the compensating phase shifts are actually implemented in practice.

This use of interacting system eigenfunctions and compensating phase shifts as described above provides a computational basis that evolves ideally between gates, but such an ap-

proach is not scalable; for example, there are  $2^{2n+1}$  such computational states in  $\text{QVN}_n$ . In Ref. [42] an approximate but scalable implementation of this approach was introduced. The idea is that the exact energy  $E$  of a computational state in  $\text{QVN}_n$  is, to an extremely good approximation, the sum of uncoupled qubit and resonator frequencies, i.e., essentially noninteracting. This is *not* simply a consequence of the dispersive regime energies (eigenvalues of  $H_{\text{idle}}$ ), which have non-negligible interaction corrections, but because only a special subset of the eigenfunctions are used for information processing: In the  $\text{QVN}_n$  system we only make use of  $H_{\text{idle}}$  eigenfunctions in which there are no more than  $n$  excitations present, and such that two directly coupled elements—qubits or resonators—are not simultaneously occupied (except during the CZ gate). For example, when the data is stored in memory, the residual memory-memory coupling is fourth order in the qubit-resonator coupling  $g$ . This leads to an eighth-order *conditional* frequency shift (order  $g^{16}$  idling error) [42]. Next, suppose an excitation is transferred from memory to a qubit via a MOVE gate. Now the dominant frequency shift is sixth order. And when an excitation is in the bus the largest shift is fourth order [42]. The largest idling error (associated with the phase compensation) is therefore eighth order in  $g$  and can be made negligible with proper system design.

The compensating phase shifts could be implemented through additional local  $z$  rotations, one for each qubit and resonator. However, these phase shifts evolve in time with very high ( $> 1$  GHz) frequency, and it is therefore experimentally more practical to introduce a local clock/rotating frame for each qubit and resonator. This is achieved by introducing a fixed-frequency microwave line for each qubit and resonator, and measuring each qubit and resonator *phase* relative to the phase of its reference. By choosing the frequency of the qubit (resonator) reference microwave equal to the idle frequency (resonator frequency), the component frequencies [and therefore the quantity  $E$  in (2.60)] are effectively zeroed, and no more than  $2n + 1$  different reference frequencies or local clocks are required. This procedure corresponds to implementing the experiment in a multi-qubit rotating frame. And,

in a further simplification, the local clocks/rotating frames for the resonators are replaced by additional qubit  $z$  rotations that are handled in software (i.e., combined with future rotations). Therefore, in practice only  $n$  local clocks/rotating frames are needed, one for each qubit. Because the CZ gate simulations reported in this work are already supplemented with local  $z$  rotations, these local clocks/rotating frames do not need to be included in those simulations; we simulate the lab frame. However, they are included in the pulse-shape error simulations reported in Sec. 2.3.7.

Having motivated the use of interacting system eigenfunctions for computational basis states, it is still necessary to establish that such states can actually be prepared and measured. Because we can assume the processor to initially start in its interacting ground state—a computational basis state—preparation of the other computational states can be viewed as a series of  $\pi$  pulses and MOVE gates. We expect that such operations on the interacting eigenfunctions can be performed at least as accurately as when applied to bare states. Eigenfunction readout is a more subtle (and model-dependent) question, but the analysis of Ref. [42] suggests that interacting-eigenfunction readout is actually better than bare-state readout (in the model considered there). We also note that the idling configuration and associated eigenstate basis generally changes between consecutive gates and, therefore, our entangling gate design is constrained by the requirement that we start and end in eigenstates of this particular  $H_{\text{idle}}$ .

The discussion above motivating the use of interacting eigenstates is based on their nearly ideal idling dynamics. It is still interesting, then, to consider whether the CZ gate can be generated equally well in either (bare or interacting eigenfunction) basis. We find that for the parameter regimes considered here, it is not possible to achieve better than about 99% fidelity in the bare basis with the same two-parameter pulse profile (it should be possible using more complex pulse shapes). The remaining error is consistent with the size of the perturbative corrections to the bare states in the idling configuration. This exercise

emphasizes the importance of performing quantum logic with the system eigenfunctions, which have the built-in protection of *adiabaticity* against unwanted transitions.

One might object to the use of interacting eigenfunctions as a design tool, the exact calculation of which is not scalable. However, approximate dispersive-regime eigenfunctions are efficiently computable. A particularly simple way to do this is to calculate the generator  $S$  of the diagonalizing transformation  $V = e^{-iS}$  by a power series in  $g_b$  and  $g_m$ . At the 99.99% fidelity level, it is sufficient to calculate  $S$  to first order. Writing  $H_{\text{idle}} = H_0 + \delta H$  leads to the condition  $i[S, H_0] + \delta H = 0$ , which is immediately solvable in the bare basis  $|q_1 q_2 \cdots m_1 m_2 \cdots b\rangle$ . Here  $q_i, m_i, b \in \{0, 1, 2, \dots\}$ . Other efficient eigenfunction approximation schemes are also possible.

In this work, for QVN $_n$  architecture we denote the exact or approximate  $H_{\text{idle}}$  eigenfunction perturbatively connected to the bare state  $|q_1 q_2 \cdots q_n m_1 m_2 \cdots m_n b\rangle$  by

$$\overline{|q_1 q_2 \cdots q_n m_1 m_2 \cdots m_n b\rangle}, \quad (2.62)$$

following the overline notation introduced above. Note that (2.62) is *not* a tensor product of single-qubit/resonator eigenstates as is usually the case.

### 2.3.3 Auxiliary $z$ rotations and equivalence class

The standard CZ gate in the bare two-qubit basis  $\{|00\rangle, |01\rangle, |10\rangle, |11\rangle\}$  is

$$\text{CZ} \equiv \begin{pmatrix} 1 & 0 & 0 & 0 \\ 0 & 1 & 0 & 0 \\ 0 & 0 & 1 & 0 \\ 0 & 0 & 0 & -1 \end{pmatrix}. \quad (2.63)$$

However in the QVN processor, local  $z$  rotations can be performed quickly and accurately, typically by brief qubit frequency excursions. Thus, we will consider the limit where  $SU(2)$  operations of the form  $\exp[-i(\theta/2)\sigma^z]$  can be done on the qubits and bus with negligible error and in a negligible amount of time (fidelity loss resulting from errors in these rotations are discussed in Sec. 2.3.7). We therefore want to define our entangling gate modulo these  $z$  rotations. We will do this by constructing a *local- $z$  equivalence class* for an arbitrary element (gate) in  $SU(4)$ , and then specialize to the CZ gate.

We define two elements  $U$  and  $U'$  of  $SU(4)$  to be equivalent, and write  $U' \doteq U$ , if

$$U' = u_{\text{post}} U u_{\text{pre}}, \quad (2.64)$$

where

$$u(\gamma_1, \gamma_2) \equiv R_z(\gamma_1) \otimes R_z(\gamma_2) = e^{i(\gamma_1+\gamma_2)/2} \begin{pmatrix} 1 & 0 & 0 & 0 \\ 0 & e^{-i\gamma_2} & 0 & 0 \\ 0 & 0 & e^{-i\gamma_1} & 0 \\ 0 & 0 & 0 & e^{-i(\gamma_1+\gamma_2)} \end{pmatrix}, \quad (2.65)$$

for some rotation angles  $\gamma_k$ . The local- $z$  equivalence class  $\{U\}$  corresponding to  $U$  is the set of elements  $u_{\text{post}} U u_{\text{pre}}$  for all  $u_{\text{pre}}, u_{\text{post}}$ . For a given gate  $U$ ,  $\{U\}$  typically occupies a four-dimensional manifold, depending on four rotation angles. But because (2.63) is diagonal,  $\{\text{CZ}\}$  instead forms a two-dimensional sheet,

$$\{\text{CZ}\} = \text{phase factor} \times \begin{pmatrix} 1 & 0 & 0 & 0 \\ 0 & e^{-i\gamma_2} & 0 & 0 \\ 0 & 0 & e^{-i\gamma_1} & 0 \\ 0 & 0 & 0 & -e^{-i(\gamma_1+\gamma_2)} \end{pmatrix}. \quad (2.66)$$

The CZ gate (2.63) can be obtained by reaching any point in the {CZ} plane and then performing auxiliary  $z$  rotations. And it is straightforward to confirm that [40]

$$\begin{pmatrix} -1 & 0 & 0 & 0 \\ 0 & 1 & 0 & 0 \\ 0 & 0 & 1 & 0 \\ 0 & 0 & 0 & 1 \end{pmatrix} \stackrel{\circ}{=} \begin{pmatrix} 1 & 0 & 0 & 0 \\ 0 & -1 & 0 & 0 \\ 0 & 0 & 1 & 0 \\ 0 & 0 & 0 & 1 \end{pmatrix} \stackrel{\circ}{=} \begin{pmatrix} 1 & 0 & 0 & 0 \\ 0 & 1 & 0 & 0 \\ 0 & 0 & -1 & 0 \\ 0 & 0 & 0 & 1 \end{pmatrix} \stackrel{\circ}{=} \begin{pmatrix} 1 & 0 & 0 & 0 \\ 0 & 1 & 0 & 0 \\ 0 & 0 & 1 & 0 \\ 0 & 0 & 0 & -1 \end{pmatrix}. \quad (2.67)$$

We note that bus rotations, which cannot be directly implemented with microwave pulses or frequency excursions, are compiled into future qubit rotations.

The discussion above assumed a pair of qubits or a qubit and resonator, but it applies to a QVN processor in the interacting eigenfunction basis (2.62) after a minor modification. In the bare basis, the CZ gate is typically defined through its action (2.63) on a pair of qubits (or a qubit and resonator). Then, action on a bare computational basis state such as  $|q_1 q_2 \cdots q_n m_1 m_2 \cdots m_n b\rangle$  follows from the tensor-product form of that bare state. In the eigenstate basis the CZ gate must be *defined* through its action on

$$\overline{|q_1 q_2 \cdots q_n m_1 m_2 \cdots m_n b\rangle}, \quad (2.68)$$

such as to reproduce the ideal action on the bare states to which they are perturbatively connected. For example, the CZ gate on qubit  $q_1$  and the bus acts ideally as

$$\begin{aligned} \text{CZ } \overline{|0q_2q_3q_4m_1m_2m_3m_40\rangle} &= \overline{|0q_2q_3q_4m_1m_2m_3m_40\rangle} \\ \text{CZ } \overline{|0q_2q_3q_4m_1m_2m_3m_41\rangle} &= \overline{|0q_2q_3q_4m_1m_2m_3m_41\rangle} \\ \text{CZ } \overline{|1q_2q_3q_4m_1m_2m_3m_40\rangle} &= \overline{|1q_2q_3q_4m_1m_2m_3m_40\rangle} \\ \text{CZ } \overline{|1q_2q_3q_4m_1m_2m_3m_41\rangle} &= -\overline{|1q_2q_3q_4m_1m_2m_3m_41\rangle}, \end{aligned}$$

where  $q_i, m_i \in \{0, 1, 2, \dots\}$ .

### 2.3.4 Pulse shape

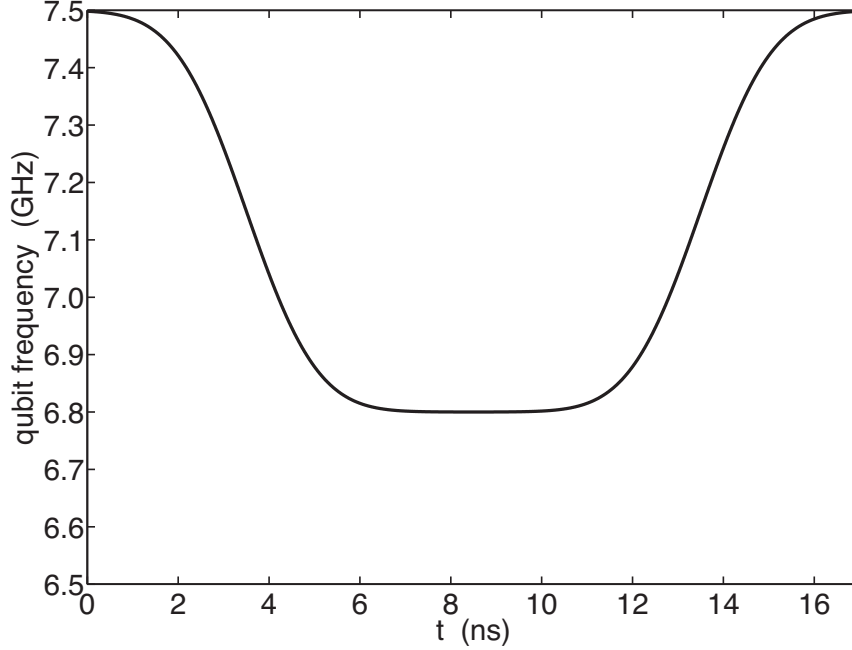


**Figure 2.9:** Two-parameter CZ pulse profile (2.69) for the case of  $\omega_{\text{on}}/2\pi = 6.8$  GHz,  $\omega_{\text{off}}/2\pi = 7.5$  GHz,  $t_{\text{ramp}} = 7$  ns,  $\sigma = 1.24$  ns, and  $t_{\text{on}} = 10$  ns. The total gate time excluding auxiliary  $z$  rotations is  $t_{\text{gate}} = 17$  ns. The example shown is representative of a 99.9% fidelity gate for a qubit with 300 MHz anharmonicity.

The two-parameter low frequency pulse profile we use throughout this work is

$$\epsilon(t) = \omega_{\text{off}} + \frac{\omega_{\text{on}} - \omega_{\text{off}}}{2} \left[ \text{Erf} \left( \frac{t - \frac{1}{2}t_{\text{ramp}}}{\sqrt{2}\sigma} \right) - \text{Erf} \left( \frac{t - t_{\text{gate}} + \frac{1}{2}t_{\text{ramp}}}{\sqrt{2}\sigma} \right) \right], \quad (2.69)$$

an example of which is shown in Fig. 2.9. Here  $\epsilon$  is the qubit frequency,  $\omega_{\text{off}}$  and  $\omega_{\text{on}}$  are the frequencies off and near resonance (with the bus), and the pulse switching time is determined by  $\sigma$ , the standard deviation of the Gaussians inside (2.69). The value of  $t_{\text{ramp}}$  determines

how the pulse is truncated at  $t = 0$  and  $t_{\text{gate}}$ . Throughout this work we assume that

$$t_{\text{ramp}} = 4\sqrt{2}\sigma. \quad (2.70)$$

The relation (2.70) allows the switching time to be alternatively characterized by  $t_{\text{ramp}}$ , which, as Fig. 2.9 illustrates, is a measure of the width of the ramps. The variable  $t_{\text{gate}}$  is the total execution time of the gate excluding  $z$  rotations. The two control parameters  $\omega_{\text{on}}$  and

$$t_{\text{on}} \equiv t_{\text{gate}} - t_{\text{ramp}} \quad (2.71)$$

are determined by the numerical optimization procedure described in Sec. 2.3.5. From (2.71) we infer that  $t_{\text{on}}$  is the time interval between the midpoints of the ramps, or the full-width at half-maximum (FWHM) of the pulse. We note that the optimal values of  $t_{\text{on}}$  are somewhat longer than the value

$$t_{\text{on}}^{\text{sudden}} \equiv \frac{\pi}{\sqrt{2}g_{\text{b}}} \quad (2.72)$$

that applies in the sudden,  $\sigma \rightarrow 0$  limit. In addition to  $\omega_{\text{on}}$  and  $t_{\text{on}}$ , two auxiliary local  $z$  rotations—on the qubit and resonator—are used to implement the CZ gate. As we explain below, adjusting the two control parameters  $\omega_{\text{on}}$  and  $t_{\text{on}}$  zeros the population left in the non-computational qubit  $|2\rangle$  state after the gate and (along with the auxiliary  $z$  rotations) sets the controlled phase equal to  $-1$ . The pulse shape (2.69) describes a rectangular current or voltage pulse sent to the qubit frequency bias through a Gaussian filter of width  $\sigma$ , and is believed to be an accurate (although not exact) representation of the actual profile seen by the qubits in Ref. [41].

In the qubit-resonator Hamiltonian (2.28), the qubit frequency  $\epsilon$  is the only available experimental control. [There is also a single-qubit term for the microwave pulse that is not shown in (2.28) and not used in this work.] During a CZ gate between a given qubit and the

resonator, the frequency of that qubit is varied according to (2.69), where

$$\text{Erf}(t) \equiv \frac{2}{\sqrt{\pi}} \int_0^t e^{-x^2} dx. \quad (2.73)$$

Two quantities related to the pulse switching— $\sigma$  and  $t_{\text{ramp}}$ —appear in the pulse profile function (2.69). We do this to emphasize that, in principal, two independent quantities could be used to quantify the shape of the switching profile. The first is the time duration (or width) of the switching, characterized by the standard deviation  $\sigma$ . The second is the truncation time of the pulse, measured from the center (half maximum) of the frequency switch, which is equal to  $t_{\text{ramp}}/2$ . However in this work we always use the (somewhat arbitrary) relation (2.70), which amounts to cutting off the pulse at  $2\sqrt{2}$  standard deviations from the switching midpoints.

If the pulse shape function (2.69) is used only when  $0 \leq t \leq t_{\text{gate}}$ , and  $\epsilon$  is set to  $\omega_{\text{off}}$  otherwise, there will be small pulse discontinuities at  $t = 0$  and  $t_{\text{gate}}$ , the size of which is determined by the condition (2.70). Assuming  $t_{\text{ramp}} \ll t_{\text{gate}}$ , we have

$$\epsilon(0) = \epsilon(t_{\text{gate}}) \approx \omega_{\text{off}} + \frac{\omega_{\text{on}} - \omega_{\text{off}}}{2} \left[ 1 - \text{Erf}(2) \right], \quad (2.74)$$

which differs from the asymptotic value  $\omega_{\text{off}}$  by an amount

$$\frac{\omega_{\text{on}} - \omega_{\text{off}}}{2} \left[ 1 - \text{Erf}(2) \right], \quad (2.75)$$

where  $1 - \text{Erf}(2) \approx 0.5\%$ . However, in an experiment these discontinuities are usually smoothed over by additional pulse shaping. Moreover, our simulations begin  $t = 0$  and end at  $t = t_{\text{gate}}$ , so the truncation only slightly affects the pulse shape: The initial and final detuned qubit frequency is actually a few MHz smaller than  $\omega_{\text{off}}$ . Having fixed the relation (2.70), there are then two measures of the pulse switching time,  $\sigma$  and  $t_{\text{ramp}}$ , with  $t_{\text{ramp}}$

providing a convenient measure of the time duration of the ramps. This property can be seen in the pulse shape example of Fig. 2.9.

### 2.3.5 Gate optimization

We numerically optimize the two pulse-shape control parameters  $\omega_{\text{on}}$  and  $t_{\text{on}}$ , as well as the two auxiliary  $z$  rotation angles,  $\gamma_1$  and  $\gamma_2$ , to maximize the average gate fidelity (2.7). All other pulse parameters ( $\omega_{\text{off}}$ ,  $\sigma$ ,  $t_{\text{ramp}}$ ) are fixed. The procedure to determine the values of  $\omega_{\text{off}}$  and  $t_{\text{ramp}}$  for QVN is described later, and  $\sigma$  is obtained through relation (2.70). The roles played by the control parameters  $\omega_{\text{on}}$  and  $t_{\text{on}}$  are discussed above in Sec. 2.3.1.

The fidelity optimization procedure is carried out in two stages: In the first stage we take  $\omega_{\text{on}}$  to be equal to its approximate value [see (2.30)]

$$\omega_{\text{b}} + \eta, \tag{2.76}$$

and optimize  $t_{\text{on}}$  to get close to the two-dimensional equivalence class  $\{\text{CZ}\}$  defined in (2.66). We do this by minimizing a sum of two positive errors, one measuring the deviation of the absolute values of the matrix elements of the evolution operator  $U$  from that of the four-dimensional identity matrix, the other measuring the deviation from the ideal relationship between the phases of the diagonal elements indicated in (2.66). This first stage yields an approximate value of  $t_{\text{on}}$ , as well as approximate rotation angles

$$\gamma_1 \approx \arg \overline{\langle 10|U|10\rangle} - \arg \overline{\langle 00|U|00\rangle}, \tag{2.77}$$

$$\gamma_2 \approx \arg \overline{\langle 01|U|01\rangle} - \arg \overline{\langle 00|U|00\rangle}. \tag{2.78}$$

In the second stage of optimization, we use the approximate values of  $\omega_{\text{on}}$ ,  $t_{\text{on}}$ ,  $\gamma_1$ , and  $\gamma_2$ , obtained from the first stage, as seeds for a full four-dimensional  $(\omega_{\text{on}}, t_{\text{on}}, \gamma_1, \gamma_2)$  nonlinear

maximization of the average fidelity (2.7) between

$$u(\gamma_1, \gamma_2) \times U \tag{2.79}$$

and the standard CZ gate (2.63). Here  $U$  is the projected evolution operator and  $u \in \text{SU}(2) \otimes \text{SU}(2)$  is defined in (2.65).

### 2.3.6 Switching error and fidelity estimate

Here we calculate the transition probability caused by a change of the qubit frequency during a CZ pulse, MOVE gate, or any other operation in a superconducting architecture. The problem will be treated quite generally and then applied to the Strauch CZ gate, resulting in a simple fidelity estimator for that gate.

Imagine that we have prepared an initial interacting system eigenfunction  $|\overline{a}\rangle$  prior to performing a CZ operation or other gate that involves changing the frequency of one or more qubits. We assume that the ideal (target) behavior during the frequency switch or ramp itself is the *identity* map (times a phase factor), and that the  $|\overline{a}\rangle$  channel does not cross any others in the system. The population loss during the ramp will therefore be exponentially suppressed if the switching time is long enough.

In a multi-qubit system there is typically a large number of nonresonant channels coupled to  $|\overline{a}\rangle$  that can be excited by the frequency switch. However, when the ramp fidelity is high and the probabilities of the undesired transitions

$$|\overline{a}\rangle \rightarrow |\overline{b}\rangle, |\overline{b'}\rangle, |\overline{b''}\rangle, \dots \tag{2.80}$$

are small, they can be individually estimated perturbatively (neglecting interference), thereby

reducing the problem to a sum of independent two-channel problems

$$\begin{aligned}
\overline{|a\rangle} &\longrightarrow \overline{|b\rangle} \\
\overline{|a\rangle} &\longrightarrow \overline{|b'\rangle} \\
\overline{|a\rangle} &\longrightarrow \overline{|b''\rangle} \\
&\vdots
\end{aligned}
\tag{2.81}$$

each characterized by a time-dependent detuning  $\Delta$  and a coupling  $G$ . Without loss of generality we can shift the energy of a given two-channel problem so that the bare final state has zero energy. Each nonadiabatic transition can therefore be described by a general two-channel model of the form

$$H = \begin{pmatrix} \Delta(t) & G \\ G & 0 \end{pmatrix},
\tag{2.82}$$

in the bare basis spanned by  $\{|a\rangle, |b\rangle\}$ . The undesired final state  $|b\rangle$  has a fixed energy 0 and the energy of  $|a\rangle$  varies in time with detuning  $\Delta$ . The coupling  $G$  is assumed to be a real, positive constant.

The instantaneous eigenstates of (2.82) are

$$\overline{|a\rangle} = \cos \frac{\chi}{2} |a\rangle + \sin \frac{\chi}{2} |b\rangle,
\tag{2.83}$$

$$\overline{|b\rangle} = \cos \frac{\chi}{2} |b\rangle - \sin \frac{\chi}{2} |a\rangle,
\tag{2.84}$$

where

$$\chi \equiv \arctan \left( \frac{2G}{\Delta} \right).
\tag{2.85}$$

The instantaneous energies are

$$E_a = \frac{\Delta}{2} + \sqrt{\left(\frac{\Delta}{2}\right)^2 + G^2}
\tag{2.86}$$

and

$$E_b = \frac{\Delta}{2} - \sqrt{\left(\frac{\Delta}{2}\right)^2 + G^2}. \quad (2.87)$$

The  $|\overline{b}\rangle$  channel is initially unoccupied at time  $t=0$ , and we are interested in the probability  $p_{\text{sw}}$  that the system, prepared in  $|\overline{a}\rangle$ , is found in  $|\overline{b}\rangle$  after changing the detuning  $\Delta$  from one value to another. We refer to this probability as the nonadiabatic switching error, which we calculate by expanding the wave function in the basis of instantaneous eigenstates (2.83) and (2.84), as

$$|\psi\rangle = \sum_{m=a,b} \psi_m e^{-i \int_0^t E_m d\tau} |\overline{m}\rangle. \quad (2.88)$$

This leads to

$$\frac{d\psi_b}{dt} = -e^{-i \int_0^t (E_a - E_b) d\tau} \langle \overline{b} | \frac{\partial}{\partial \Delta} | \overline{a} \rangle \frac{d\Delta}{dt} \psi_a, \quad (2.89)$$

where

$$\langle \overline{b} | \frac{\partial}{\partial \Delta} | \overline{a} \rangle = -\frac{G}{\Delta^2} \times \frac{1}{1 + \left(\frac{2G}{\Delta}\right)^2}. \quad (2.90)$$

The nonadiabatic matrix element (2.90) has been written so that the second term approaches unity in the  $G \ll \Delta$  perturbative limit.

At time  $t=0$ ,  $\psi_a = 1$ . An approximate expression for

$$p_{\text{sw}} \equiv |\psi_b(t_{\text{final}})|^2 \quad (2.91)$$

can be obtained from (2.89) by assuming that  $|\psi_b| \ll 1$  throughout the evolution, so that  $\psi_a \approx 1$  for all  $t$ . Then

$$p_{\text{sw}} = \left| \int \frac{G \dot{\Delta} e^{-i \int_0^t \Omega d\tau}}{\Omega^2} dt \right|^2 = \frac{1}{4} \left| \int \dot{\chi} e^{-i \int_0^t \Omega d\tau} dt \right|^2, \quad (2.92)$$

where

$$\Omega \equiv E_a - E_b = \sqrt{\Delta^2 + 4G^2} \quad (2.93)$$

is the instantaneous splitting. We can simplify (2.92) further by assuming  $G \ll \Delta$ , which will be the case for the applications considered below. In this perturbative limit we therefore obtain

$$p_{\text{sw}} = \left| \int \frac{G\dot{\Delta}}{\Delta^2} e^{-i \int_0^t \Delta d\tau} dt \right|^2. \quad (2.94)$$

We emphasize that the form (2.94) assumes that  $\Delta$  does not pass through zero, which would cause Landau-Zener tunneling and invalidate the perturbative analysis.

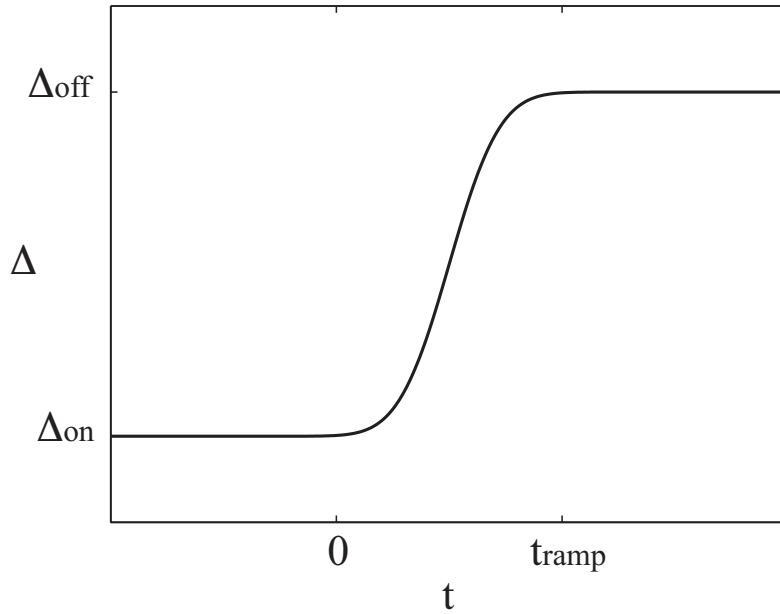


**Figure 2.10:** Detuning pulse profile (2.95) for a single frequency switch.

In this work we are specifically interested in  $p_{\text{sw}}$  for a single switch of the detuning from  $\Delta_{\text{on}}$  to  $\Delta_{\text{off}}$  (or the reverse) according to the smooth, error-function based profile

$$\Delta(t) = \frac{\Delta_{\text{off}} + \Delta_{\text{on}}}{2} + \frac{\Delta_{\text{off}} - \Delta_{\text{on}}}{2} \text{Erf} \left( \frac{t - \frac{1}{2}t_{\text{ramp}}}{\sqrt{2}\sigma} \right), \quad (2.95)$$

shown in Fig. 2.10. The standard deviation  $\sigma$  characterizes the switching time of the pulse and  $t_{\text{ramp}}$  [related to  $\sigma$  through (2.70)] specifies its truncation, as discussed in Sec. 2.3.4. We

use this switching profile for both CZ and MOVE gates. The switching error for the single switch profile defined in (2.95) (and shown in Fig. 2.10) can be expressed as

$$p_{\text{sw}} = \left( \frac{G}{\Delta_{\text{on}}} \right)^2 |A|^2, \quad (2.96)$$

where

$$A(\Delta_{\text{on}}, \Delta_{\text{off}}, \sigma) \equiv \Delta_{\text{on}} \int_0^{t_{\text{ramp}}} \frac{\dot{\Delta}}{\Delta^2} e^{-i \int_0^t \Delta d\tau} dt. \quad (2.97)$$

The dimensionless quantity  $|A|^2$  is plotted in Fig. 2.11 for five instances of  $\Delta_{\text{on}}$  and  $\Delta_{\text{off}}$  relevant to this work. We note that  $p_{\text{sw}}$  evidently decreases as an exponential function of  $\sigma$ , as expected for a nonadiabatic process. However, the dependence of  $|A|^2$  on  $\sigma$  for large  $\sigma$  is somewhat intricate, a consequence of the error-function ramp shape. For very large values of  $\sigma$ —not shown in Fig. 2.11—the decay of  $|A|^2$  becomes slower (the location of the crossover depends on the details of the pulse truncation). Although an approximate analytic expression for  $|A|^2$  can be derived for this large- $\sigma$  limit expanding it iteratively with integration-by-parts, the formula is not useful for the regimes of interest here.

We now turn to the application of the switching error formula (2.96) to the CZ gate. We observe that the dominant intrinsic error is contributed by the leakage  $\overline{|11\rangle} \rightarrow \overline{|02\rangle}$ . It is possible to understand this dominant  $\overline{|11\rangle} \rightarrow \overline{|02\rangle}$  leakage error in a further simplified two-channel model that only includes the channels  $\overline{|11\rangle}$  and  $\overline{|02\rangle}$ . Given the strong interaction of the bare  $|11\rangle$  state with  $|20\rangle$ , it is not at all obvious that such a simplification is possible. However, during most of the switching, the detuning between  $|11\rangle$  and  $|20\rangle$  is much larger than their interaction strength  $\sqrt{2}g_{\text{b}}$ , so they are effectively decoupled. (And while the qubit sits at the  $\omega_{\text{on}}$  frequency, the Hamiltonian is time-independent.) Therefore a two-channel description should be possible, although it will slightly overestimate the excitation of  $\overline{|02\rangle}$ . Numerical investigation confirms that the  $\overline{|20\rangle}$  channel can indeed be disregarded except for the level repulsion it produces on the  $\overline{|11\rangle}$  state (see below), which is crucial for obtaining

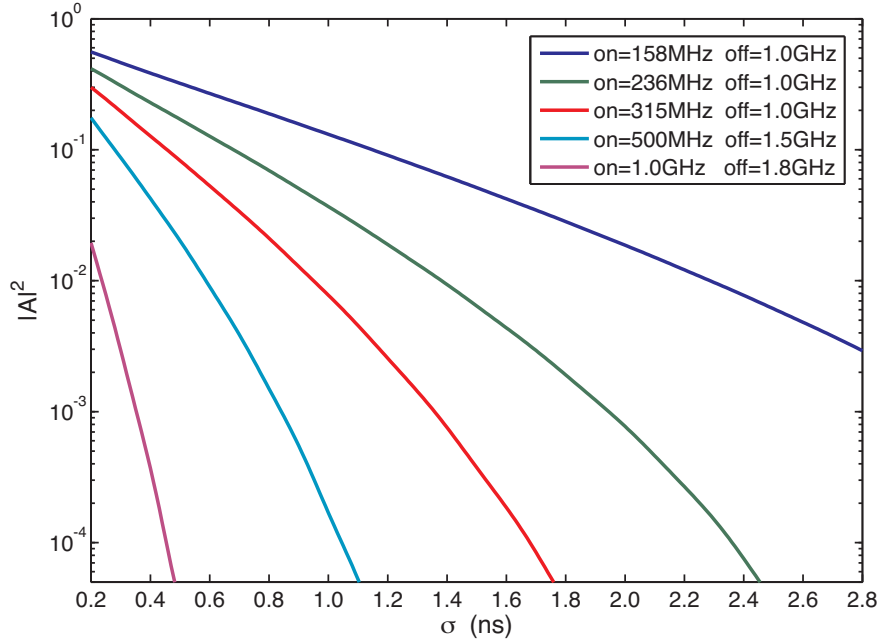


**Figure 2.11:** (Color online)  $|A|^2$  versus switching time  $\sigma$  for indicated values of  $\Delta_{\text{on}}$  and  $\Delta_{\text{off}}$ .

an accurate fidelity estimate.

In the bare  $\{|11\rangle, |02\rangle\}$  basis, (2.28) reduces to

$$H = \begin{pmatrix} \epsilon & \sqrt{2}g_b \\ \sqrt{2}g_b & \omega_b \end{pmatrix} + \text{const.} \quad (2.98)$$

At the beginning of the CZ pulse, the qubit frequency is 1.0 GHz above the bus.  $\epsilon$  then decreases to  $\omega_{\text{on}} \approx \omega_b + \eta$  and returns to the detuned configuration in the manner of Fig. 2.9. The total leakage to  $\overline{|02\rangle}$  can be estimated as twice—because there are two switching events, which we assume to contribute incoherently—the value of  $p_{\text{sw}}$ . Therefore the error  $\mathbb{E}_2$  introduced in (2.58) is given by

$$\mathbb{E}_2 = 2p_{\text{sw}}. \quad (2.99)$$

To evaluate the switching error in this case, we use (2.96) with the parameter values

$$G = \sqrt{2}g_b, \quad (2.100)$$

$$\Delta_{\text{on}} = \eta - \sqrt{2}g_b, \quad (2.101)$$

$$\Delta_{\text{off}} = \omega_{\text{off}} - \omega_b. \quad (2.102)$$

The value of  $\Delta_{\text{on}}$  accounts for the level repulsion caused by the neglected  $|20\rangle$  state, which causes the  $|\overline{11}\rangle$  channel to shift downwards towards  $|\overline{02}\rangle$ ; this large effect is evident in Fig. 2.8. [We ignore here a smaller repulsion by  $|\overline{02}\rangle$ , which would lead to the addition of a small positive correction to (2.101).]  $\Delta_{\text{off}}/2\pi$  is always 1.0 GHz for the gates and the required  $|A|^2$  values are obtained from Fig. 2.11.

The minimum fidelity estimate is, therefore,

$$F_{|\overline{11}\rangle}^{(\text{est})} \equiv 1 - \mathbb{E}_2 = 1 - 2p_{\text{sw}}. \quad (2.103)$$

We find that (2.103) is a reliable predictor of the worst-case fidelity  $F_{|\overline{11}\rangle}$  in QVN<sub>4</sub> system (discussed in the next section), confirming that the nonadiabatic switching error is the dominant fidelity loss mechanism here. Although this error will always be present, it can be exponentially suppressed by increasing the switching time.

Finally, we briefly comment on the nonadiabatic switching errors between the  $|\overline{01}\rangle$  and  $|\overline{10}\rangle$  eigenstates, which we have argued to be subdominant to the excitation of  $|\overline{02}\rangle$ , but which naively are of the same order. There are two reasons why the  $|\overline{01}\rangle$  and  $|\overline{10}\rangle$  switching errors are considerably smaller: First, the matrix element coupling  $|\overline{01}\rangle$  and  $|\overline{10}\rangle$  is a factor of  $\sqrt{2}$  smaller than that between  $|\overline{11}\rangle$  and  $|\overline{02}\rangle$ , and this factor gets squared in (2.96). And the second—but quantitatively more important—reason is that while level repulsion considerably enhances the  $|\overline{02}\rangle$  excitation [recall (2.101)], it (slightly) suppresses transitions between  $|\overline{01}\rangle$

and  $\overline{|10\rangle}$ .

We can estimate the switching errors between the  $\overline{|01\rangle}$  and  $\overline{|10\rangle}$  channels during a CZ gate by using (2.96) with parameters

$$G = g_b, \quad (2.104)$$

$$\Delta_{\text{on}} = \eta + \frac{2g_b^2}{\eta}, \quad (2.105)$$

and with  $\Delta_{\text{off}}/2\pi = 1$  GHz as before. The expression (2.105) for  $\Delta_{\text{on}}$  accounts for the level repulsion between  $\overline{|01\rangle}$  and  $\overline{|10\rangle}$ , which suppresses the switching error, in contrast with the strong enhancement indicated in (2.101).

### 2.3.7 Pulse shape errors

In Sec. 2.3.6 we discussed the intrinsic error of the qubit-resonator CZ gate—assuming an optimal pulse shape—and identified its dominant source as a nonadiabatic switching error  $\mathbb{E}_2$ . In this section we discuss and quantify the fidelity loss caused by pulse shape and auxiliary  $z$  rotation errors. By a pulse shape error we mean that the correct functional form (2.69) is seen by the qubit, but with values of the parameters  $t_{\text{on}}$  and  $\omega_{\text{on}}$  that deviate from the optimal values. It is possible to develop simple analytic models for these error mechanisms (supported by numerical simulation) by noting that when the fidelity is very close to unity, the different error mechanisms present contribute independently and can be calculated separately. We then use these results to estimate the experimental pulse-control precision required during the implementation of a given 99.9% or 99.99% CZ gate to keep any accompanying pulse shape error less than the base  $10^{-3}$  or  $10^{-4}$  gate error.

The simplest situation to consider is that where the correct values of  $t_{\text{on}}$  and  $\omega_{\text{on}}$  are used, but where the local  $z$  rotation angles  $\gamma_k$  ( $k = 1, 2$ ) applied experimentally deviate from their optimal values by amounts  $\varphi_k \ll 1$ . We estimate the resulting fidelity loss by imagining that

we have achieved a perfect CZ-class gate

$$U = \begin{pmatrix} 1 & 0 & 0 & 0 \\ 0 & e^{i\Theta_2} & 0 & 0 \\ 0 & 0 & e^{i\Theta_1} & 0 \\ 0 & 0 & 0 & -e^{i(\Theta_1+\Theta_2)} \end{pmatrix}, \quad (2.106)$$

for some phase angles  $\Theta_k$ , but then apply  $z$  rotation angles

$$\gamma_k = \Theta_k + \varphi_k \quad (2.107)$$

that have errors  $\varphi_k$ . From (2.7) we find that this leads to a leading order error  $\mathbb{E} \equiv 1 - F_{\text{ave}}$  given by

$$\mathbb{E} = \frac{\varphi_1^2 + \varphi_2^2}{5}. \quad (2.108)$$

Next we consider  $t_{\text{on}}$  and  $\omega_{\text{on}}$  errors. An error in either  $t_{\text{on}}$  or  $\omega_{\text{on}}$  has two consequences, the first is to modify the accumulated phases  $\Theta_k$  in (2.106), and the second is to cause population and phase errors on the  $\overline{|11\rangle}$  channel. Therefore we consider two types of pulse shape errors, the first where  $t_{\text{on}}$  or  $\omega_{\text{on}}$  is changed with no compensating changes in the auxiliary  $z$  rotation angles, and the second where the  $\gamma_k$  are reoptimized.

In the first case, in which the error is clearly the largest, the resulting error is dominated by the  $z$  rotation angle error itself, which can be estimated from (2.108). Changing  $t_{\text{on}}$  by an amount  $\delta t_{\text{on}}$ , or  $\omega_{\text{on}}$  by an amount  $\delta \omega_{\text{on}}$ , changes the accumulated phase of the qubit (recall discussion of the qubit reference frame in Sec. 2.3.2) by

$$\varphi_1 = (\omega_{\text{on}} - \omega_{\text{off}}) \delta t_{\text{on}} + \delta \omega_{\text{on}} t_{\text{on}}, \quad (2.109)$$

and that of the resonator by

$$\varphi_2 = 0. \quad (2.110)$$

We note that  $\delta t_{\text{on}}$  and  $\delta \omega_{\text{on}}$  can be positive or negative here, and that the total gate time  $t_{\text{gate}}$  is also (slightly) changed by  $\delta t_{\text{on}}$ . The additional accumulated phase (2.109) can be regarded as a rotation angle error because, by assumption, it is not compensated by the applied  $z$  rotations (hence the notation). The error angle  $\varphi_2$  is zero because of our choice of the local clock/reference frame for a resonator. Therefore, an error in either  $t_{\text{on}}$  or  $\omega_{\text{on}}$  with no compensating adjustment of the auxiliary  $z$  rotation angles leads to a leading-order fidelity loss of

$$\mathbb{E} = \frac{(\omega_{\text{off}} - \omega_{\text{on}})^2}{5} \delta t_{\text{on}}^2 + \frac{t_{\text{on}}^2}{5} \delta \omega_{\text{on}}^2. \quad (2.111)$$

For an order-of-magnitude estimate it is sufficient to approximate  $\omega_{\text{on}}$  here by  $\omega_{\text{b}}$  and  $t_{\text{on}}$  by  $t_{\text{on}}^{\text{sudden}}$  [see (2.72)], leading to the simpler estimate

$$\mathbb{E}' = \frac{(\omega_{\text{off}} - \omega_{\text{b}})^2}{5} \delta t_{\text{on}}^2 + \frac{(t_{\text{on}}^{\text{sudden}})^2}{5} \delta \omega_{\text{on}}^2. \quad (2.112)$$

Next we consider the case where there is an error in  $t_{\text{on}}$  or  $\omega_{\text{on}}$ , but the auxiliary  $z$  rotation angles are optimal. Here the analysis closely follows that of Sec. 2.3.1, which is based on the qubit-resonator model (2.28). In this situation the fidelity loss is dominated by deviations from the ideal evolution

$$\text{CZ } \overline{|11\rangle} = -\overline{|11\rangle} \quad (2.113)$$

of the  $\overline{|11\rangle}$  channel. Pulse shape errors will lead to both population and phase errors on the

right-hand-side of (2.113). We therefore parameterize the nonideal CZ gate by

$$U = \text{phase factor} \times \begin{pmatrix} 1 & 0 & 0 & 0 \\ 0 & 1 & 0 & 0 \\ 0 & 0 & 1 & 0 \\ 0 & 0 & 0 & -e^{i\delta} \cos \frac{\theta}{2} \end{pmatrix}. \quad (2.114)$$

In (2.114) we have assumed perfect auxiliary  $z$  rotations and have neglected the subdominant errors in the  $|\overline{00}\rangle$ ,  $|\overline{01}\rangle$ , and  $|\overline{10}\rangle$  channels. The population error has been written in terms of a rotation angle error  $\theta$ , which will be interpreted (see below) as the deviation from  $2\pi$  of the rotation angle in the two-dimensional subspace spanned by  $|11\rangle$  and  $|20\rangle$ . The expression (2.114) does not include switching errors because we are evaluating the effect of pulse-shape errors on an otherwise perfect, large- $\sigma$  CZ gate. The average fidelity loss  $\mathbb{E} \equiv 1 - F_{\text{ave}}$  associated with (2.114) is, to leading order,

$$\mathbb{E} = \frac{3}{20} \delta^2 + \frac{1}{16} \theta^2. \quad (2.115)$$

What remains is to express the controlled phase error  $\delta$  and rotation error angle  $\theta$  in terms of  $\delta t_{\text{on}}$  and  $\delta \omega_{\text{on}}$ . This involves only the two channels  $|\overline{11}\rangle$  and  $|\overline{20}\rangle$  of the qubit-resonator model (2.28), and we will use the same small- $\sigma$  approximation used in Sec. 2.3.1 for our analysis of the  $|\overline{11}\rangle$  channel dynamics. In the  $\{|11\rangle, |20\rangle\}$  basis, (2.28) can be written as

$$H = \begin{pmatrix} \epsilon + \omega_{\text{b}} & \sqrt{2}g_{\text{b}} \\ \sqrt{2}g_{\text{b}} & 2\epsilon - \eta \end{pmatrix}. \quad (2.116)$$

The eigenstates of (2.116) are

$$\overline{|11\rangle} = \cos \frac{\zeta}{2} |11\rangle - \sin \frac{\zeta}{2} |20\rangle, \quad (2.117)$$

$$\overline{|20\rangle} = \cos \frac{\zeta}{2} |20\rangle + \sin \frac{\zeta}{2} |11\rangle, \quad (2.118)$$

where

$$\zeta \equiv \arctan \left( \frac{2\sqrt{2}g_b}{\epsilon - \omega_{\text{on}}} \right), \quad (2.119)$$

and the energies are

$$E_{11} = \epsilon + \omega_b + \frac{\epsilon - \omega_{\text{on}}}{2} - \sqrt{\left(\frac{\epsilon - \omega_{\text{on}}}{2}\right)^2 + (\sqrt{2}g_b)^2}, \quad (2.120)$$

$$E_{20} = \epsilon + \omega_b + \frac{\epsilon - \omega_{\text{on}}}{2} + \sqrt{\left(\frac{\epsilon - \omega_{\text{on}}}{2}\right)^2 + (\sqrt{2}g_b)^2}. \quad (2.121)$$

Here we have used the expression (2.30) for  $\omega_{\text{on}}$ , which is appropriate for the model (2.116).

The analysis below follows that of the  $\overline{|11\rangle}$  channel evolution given Sec. 2.3.1, except here we introduce a timing error  $\delta t_{\text{on}}$  and a tuning error  $\delta\omega_{\text{on}}$ . Starting in the strongly detuned configuration with  $\epsilon - \omega_{\text{on}} \gg g_b$  in the eigenstate  $\overline{|11\rangle} \approx |11\rangle$ , and quickly switching to  $\epsilon = \omega_{\text{on}} + \delta\omega_{\text{on}}$ , leaves the system in the state

$$|11\rangle = \cos \frac{\zeta_{\text{on}}}{2} \overline{|11\rangle} + \sin \frac{\zeta_{\text{on}}}{2} \overline{|20\rangle}. \quad (2.122)$$

Here  $\zeta_{\text{on}} \equiv \arctan(2\sqrt{2}g_b/\delta\omega_{\text{on}})$ , and the eigenstates in (2.122) are for  $\epsilon = \omega_{\text{on}} + \delta\omega_{\text{on}}$ . Note that (2.122) reduces to (2.43) in the  $\delta\omega_{\text{on}} \rightarrow 0$  limit. Evolution with  $\epsilon$  fixed at  $\omega_{\text{on}} + \delta\omega_{\text{on}}$  for a time

$$\frac{2\pi}{E_{20} - E_{11}} = \frac{\pi}{\sqrt{(\delta\omega_{\text{on}}/2)^2 + (\sqrt{2}g_b)^2}} \quad (2.123)$$

would implement a  $2\pi$  rotation in the  $\{|11\rangle, |20\rangle\}$  subspace, returning to  $|11\rangle$  with a phase

shift that depends on  $\delta\omega_{\text{on}}$ . We intentionally introduce a  $t_{\text{on}}$  pulse shape error and instead evolve for a time

$$t = \frac{\pi}{\sqrt{(\delta\omega_{\text{on}}/2)^2 + (\sqrt{2}g_{\text{b}})^2}} + \delta t_{\text{on}}, \quad (2.124)$$

after which we detune and find the final state

$$-e^{i\delta} \cos \frac{\theta}{2} |11\rangle + \text{phase factor} \times \sqrt{\mathbb{E}_\theta} |20\rangle \approx -e^{i\delta} \cos \frac{\theta}{2} \overline{|11\rangle} + \text{phase factor} \times \sqrt{\mathbb{E}_\theta} \overline{|20\rangle}, \quad (2.125)$$

where

$$\delta = -\frac{\pi \delta\omega_{\text{on}}}{2\sqrt{2}g_{\text{b}}} \quad (2.126)$$

and

$$\mathbb{E}_\theta \equiv \sin^2 \frac{\theta}{2} = 2g_{\text{b}}^2 \delta t_{\text{on}}^2. \quad (2.127)$$

These expressions are valid to leading order in  $\delta\omega_{\text{on}}$  or  $\delta t_{\text{on}}$ , neglecting cross terms. Here  $\mathbb{E}_\theta$  is the probability of leakage to  $\overline{|20\rangle}$  resulting from a  $t_{\text{on}}$  error, which, as discussed above, causes a rotation error of angle  $\theta$ . An alternative estimate for  $\theta$  (and hence  $\mathbb{E}_\theta$ ) is

$$\theta \approx \frac{\delta t_{\text{on}}}{t_{\text{on}}} \times 2\pi, \quad (2.128)$$

which also gives (2.127) [after using the sudden limit result (2.72) for  $t_{\text{on}}$ ]. Note that the leakage error  $\mathbb{E}_\theta$  is independent of  $\delta\omega_{\text{on}}$  (to this order), enabling the phase  $\delta$  to be intentionally adjusted by varying  $\omega_{\text{on}}$  only. Doing this generates (approximately) gates of the form

$$\begin{pmatrix} 1 & 0 & 0 & 0 \\ 0 & 1 & 0 & 0 \\ 0 & 0 & 1 & 0 \\ 0 & 0 & 0 & e^{i(\pi+\delta)} \end{pmatrix}, \quad (2.129)$$

for small  $\delta$ , with alternative controlled phases [44]. Gates (approximately) of the form (2.129) with arbitrary—not necessarily small—values of  $\delta$  can be implemented by varying both  $\omega_{\text{on}}$  and  $t_{\text{on}}$  away from their optimal values.

Finally, it is interesting to use the above estimates to bound the magnitude of the allowable  $t_{\text{on}}$  and  $\omega_{\text{on}}$  errors, such that the resulting pulse shape errors (2.115) are subdominant to the  $10^{-3}$  or  $10^{-4}$  base gate error. This is done in Table 2.4. For example, a 99.9% CZ gate with a  $t_{\text{on}}$  error of 160 ps will have an additional intrinsic error of  $10^{-3}$  (and a total error of about  $2 \times 10^{-3}$ ). Current experimental limitations on the control of  $t_{\text{on}}$  and  $\omega_{\text{on}}$  are considerably better than that required to suppress pulse shape errors below the  $10^{-4}$  level.

**Table 2.4:** CZ pulse shape precision requirements. The bounds listed in the  $t_{\text{on}}$  column assume that this is the only type of pulse parameter inaccuracy present, with an (estimated) error given in the first column, and that the auxiliary  $z$  rotation angles are reoptimized and implemented perfectly. The  $\omega_{\text{on}}$  bounds are defined analogously. The error  $\mathbb{E}$  is defined in (2.115).

$\mathbb{E}$	$t_{\text{on}}$ precision	$\omega_{\text{on}}$ precision
$10^{-3}$	160 ps	4 MHz
$10^{-4}$	50 ps	1 MHz

### 2.3.8 Controlled- $\sigma^z$ gate between directly coupled qubits: A comparison

So far, the main focus of this thesis has been the CZ gate between a directly coupled qubit and resonator. However many of our results—especially the error analysis—will also be relevant for hardware designs incorporating pairs of directly coupled superconducting qubits, the system originally considered by Strauch et al. [16]. We shall discuss the CZ gate between directly coupled qubits later in Sec. 3.2.1 in the context of ancilla-assisted qubit measurement and show the energy level diagram. Here we summarize the principal differences between the qubit-bus CZ gate of Sec. 2.3.1 and the directly coupled qubit-qubit gate. For the latter case

we assume qubits with anharmonic detunings  $\eta_1$  and  $\eta_2$  and a purely transverse (off-diagonal) capacitive coupling with interaction strength  $g$ .

The first difference concerns a *frequency asymmetry* of the qubit-bus gate. Recall from Sec. 2.3.1 that the CZ gate is implemented by *decreasing* the qubit frequency  $\epsilon$  from a value far above  $\omega_b$  to (approximately)

$$\epsilon = \omega_b + \eta, \quad (2.130)$$

where  $\eta > 0$  is the qubit anharmonicity. By contrast, the qubit-qubit CZ gate can be implemented either by decreasing the frequency  $\epsilon_1$  of qubit 1 from a value far *above* that of a second qubit with a (fixed) frequency  $\epsilon_2$ , until

$$\epsilon_1 = \epsilon_2 + \eta_1, \quad (2.131)$$

which is directly analogous to (2.130), or from *below* by increasing to

$$\epsilon_1 = \epsilon_2 - \eta_2. \quad (2.132)$$

The conditions (2.131) and (2.132) specify the crossings of the bare  $|11\rangle$  state with  $|20\rangle$  and  $|02\rangle$ , respectively (in the basis  $|q_1 q_2\rangle$ ). The frequency asymmetry of the qubit-bus gate is a consequence of the harmonic spectrum of the bus and can be understood from Fig. 2.8, which shows that when  $|11\rangle$  reaches the  $|02\rangle$  crossing from below,  $|01\rangle$  and  $|10\rangle$  also become degenerate [as expected from (2.132) when  $\eta_2 \rightarrow 0$ ]. This would result in unwanted phase shifts of the  $\overline{|01\rangle}$  and  $\overline{|10\rangle}$  channels, as well as large switching errors between them.

The second major difference between the qubit-bus and qubit-qubit gates is that the additional anharmonicity in the latter case further suppresses the nonadiabatic switching errors and leads to better gate performance. This can be understood from the analysis of Sec. 2.3.6, noting that in the qubit-qubit case, adiabaticity of the  $\overline{|11\rangle}$  channel is protected

by an energy gap of size  $\eta_1 + \eta_2 - \sqrt{2}g$ , where  $g$  is the qubit-qubit interaction strength. Let's estimate the  $\overline{|11\rangle} \rightarrow \overline{|02\rangle}$  switching error  $\mathbb{E}_2$  for a qubit-qubit CZ gate at the upper frequency (2.131), with  $\eta_1 = \eta_2 = 2\pi \times 300$  MHz,  $g = 45$  MHz, and  $t_{\text{ramp}} = 7$  ns. In this application we use formula (2.96) with parameter values

$$G = \sqrt{2}g, \quad (2.133)$$

$$\Delta_{\text{on}} = \eta_1 + \eta_2 - \sqrt{2}g, \quad (2.134)$$

$$\Delta_{\text{off}} = 2\pi \times 1 \text{ GHz}. \quad (2.135)$$

We note from (2.134) that the anharmonicity suppressing the  $\overline{|11\rangle} \rightarrow \overline{|02\rangle}$  switching error is effectively doubled in the qubit-qubit system. With these parameters we obtain  $|A|^2 = 5.8 \times 10^{-6}$  and  $p_{\text{sw}} = 8.2 \times 10^{-8}$ .

Although the  $\overline{|11\rangle} \rightarrow \overline{|02\rangle}$  switching error is greatly reduced in the qubit-qubit CZ gate, the actual gate fidelity does not fully benefit from this reduction. This is because the dominant intrinsic error in the qubit-qubit gate is the switching error  $\mathbb{E}_1$  between  $\overline{|01\rangle}$  and  $\overline{|10\rangle}$ , or the reverse, which is subdominant in the qubit-bus case (see Sec. 2.3.6). In fact, the  $\overline{|01\rangle} \leftrightarrow \overline{|10\rangle}$  switching error estimate also applies to the qubit-qubit system (with  $\eta_1 = \eta_2 = 2\pi \times 300$  MHz,  $g = 45$  MHz, and  $t_{\text{ramp}} = 7$  ns), resulting in an estimated minimum fidelity of

$$F_{\text{min}}^{(\text{est})} \equiv 1 - \mathbb{E}_1 = 1 - 2p_{\text{sw}} = 99.991\%. \quad (2.136)$$

## 2.4 Controlled- $\sigma^z$ gate in QVN architecture <sup>1</sup>

In this section, I describe QVN architecture in detail that has already been introduced briefly in Sec. 2.3, and then discuss CZ gates between various elements of QVN. In this architecture, superconducting qubits are capacitively coupled both to individual memory resonators as well as a common bus, as illustrated in Fig. 2.7. The key feature of this architecture is that information (data) is stored in memory resonators that are isolated by *two* detuned coupling steps from the bus. Qubits are used to transfer information to and from the bus or entangle with it, and to implement single-qubit operations, but are otherwise kept in their ground states. No more than one qubit (attached to the same bus) is to be occupied at any time. Such an approach significantly improves the effective on/off ratio without introducing the added complexity of nonlinear tunable coupling circuitry. The spectral crowding problem of the usual qubit-bus architecture is greatly reduced because the four-step coupling between memory resonators is negligible. And an added benefit of the QVN approach is that the longer coherence times of the memory elements reduce the overall decoherence rate of the device. (In Ref. [42], the architecture we consider is referred to as the resonator-zero-qubit architecture, but here we will follow the QVN terminology of [41].)

We, however, emphasize that the QVN architecture of Mariani *et al.* [41] is not, by itself, capable of large-scale, fault-tolerant quantum computation, nor is it known how multiple QVN devices might be integrated into a scalable design. The problem of designing scalable, fault-tolerant architectures for superconducting qubits is of great interest and importance [1, 45], but is still in its infancy. We chose QVN as an example of multi-qubit architecture in order to demonstrate the robustness of our CZ gate beyond a two-qubit or a qubit-resonator device. We also expect the gate design approach discussed here to be appli-

---

<sup>1</sup>J. Ghosh, A. Galiutdinov, Z. Zhou, A. N. Korotkov, J. M. Martinis, and M. R. Geller, *Physical Review A* **87**, 022309 (2013) [Copyrighted material reprinted in this section as per transfer of copyright agreement with the publisher].

cable to future architecture designs incorporating qubits coupled to resonators, and perhaps beyond.

Along with high-fidelity single-qubit rotations [10,46], quantum computing with the QVN processor requires two additional types of operations. The first is state transfer between the different physical components, which has to be performed frequently during a computation. The simplest case of state transfer is between a qubit and its associated memory (or the reverse). This case is investigated in Ref. [42], where two important observations are made: First, in contrast with the usual SWAP or iSWAP operation, which must be able to simultaneously transfer quantum information in two directions, only unidirectional state transfers are required in the QVN system. This is because adjacent qubits and resonators are—by agreement—never simultaneously populated. Second, the phase of a transferred  $|1\rangle$  state is immaterial, as it can always be adjusted by future qubit  $z$  rotations [47,48]. These two simplifications allow the resulting state transfer operation, called a MOVE gate, to be carried out with extremely high intrinsic fidelity—perfectly for a truncated model—with a simple four-parameter pulse profile. By intrinsic fidelity we mean the process fidelity (defined earlier) in the absence of noise or decoherence. The need for four control parameters immediately follows from the requirement that after a MOVE gate, the probability amplitudes must vanish on two device components, the component ( $q$  or  $m$ ) the state is leaving, and the bus  $b$ . Each zero imposes two real parameters, and no other probability amplitudes acquire weight (in the truncated model). Fixing the phase of the MOVE gate, if desired, requires one additional control parameter in the form of a local  $z$  rotational angle. State transfer between a qubit and the bus (or the reverse) can be analyzed in the same way, although in this case more pulse-shape parameters are required. In an  $n$ -qubit QVN processor (consisting of  $n$  qubits,  $n$  memory resonators, and the bus), zero-amplitude conditions must be enforced on the additional  $n - 1$  qubits, leading to a total of  $2(n + 1)$  pulse parameters, plus one  $z$  rotation angle. This makes quasi-exact state transfer to and from the bus a considerably

more challenging operation. Simpler three-parameter approximate transfers, however, can still be implemented with very high fidelity, even when the coupling is strong.

### 2.4.1 QVN architecture

The QVN<sub>*n*</sub> processor consists of *n* superconducting qubits capacitively coupled to *n* memory resonators and to a common bus resonator. Here we assume parameters appropriate either for phase qubits [49] or transmon qubits [13, 50] with tunable transition frequencies. We write the qubit angular frequencies as  $\epsilon_i$ , with  $i = 1, \dots, n$ . These are the only controllable parameters in the QVN Hamiltonian, as far as two-qubit operations are concerned. The memory frequencies are written as  $\omega_{mi}$ , and the bus frequency is  $\omega_b$ . The (bare) frequencies of all resonators are assumed here to be fixed.

Because we are interested in very high fidelities, a realistic model is required. However, we have shown (in unpublished work) that the CZ performance is extremely robust with respect to the model details, so we only report results for a simplified Hamiltonian; the approximations used are discussed below. For the qubit-bus CZ simulations, the Hilbert space is truncated to allow for up to three excitations. The CZ gate naively involves no more than two excitations, so to properly account for leakage we include up to three. Therefore, four-level qubits and resonators (which include the  $|3\rangle$  states) are required in the model. The

QVN Hamiltonian we use is

$$\begin{aligned}
H = & \sum_{i=1}^n \left[ \begin{pmatrix} 0 & 0 & 0 & 0 \\ 0 & \epsilon_i & 0 & 0 \\ 0 & 0 & 2\epsilon_i - \eta & 0 \\ 0 & 0 & 0 & 3\epsilon_i - \eta' \end{pmatrix}_{qi} + \begin{pmatrix} 0 & 0 & 0 & 0 \\ 0 & \omega_{mi} & 0 & 0 \\ 0 & 0 & 2\omega_{mi} & 0 \\ 0 & 0 & 0 & 3\omega_{mi} \end{pmatrix}_{mi} + g_m Y_{qi} \otimes Y_{mi} + g_b Y_{qi} \otimes Y_b \right] \\
& + \begin{pmatrix} 0 & 0 & 0 & 0 \\ 0 & \omega_b & 0 & 0 \\ 0 & 0 & 2\omega_b & 0 \\ 0 & 0 & 0 & 3\omega_b \end{pmatrix}_b, \tag{2.137}
\end{aligned}$$

excluding single-qubit terms for microwave pulses that are not used in this work. Here  $\eta$  and  $\eta'$  are qubit anharmonic detuning frequencies,  $g_m$  and  $g_b$  are the qubit-memory and qubit-bus interaction strengths, and

$$Y \equiv \begin{pmatrix} 0 & -i & 0 & 0 \\ i & 0 & -\sqrt{2}i & 0 \\ 0 & \sqrt{2}i & 0 & -\sqrt{3}i \\ 0 & 0 & \sqrt{3}i & 0 \end{pmatrix}. \tag{2.138}$$

The matrices in (2.137) act nontrivially in the spaces indicated by their subscripts, and as the identity otherwise. The matrix  $Y$  results from a harmonic oscillator approximation for the qubit eigenfunctions. Factors of  $\hbar$  are suppressed throughout.

The main approximations leading to (2.137) are the neglect of the  $\epsilon$ -dependence of the interaction strengths  $g_m$  and  $g_b$ , and the neglect of a small direct coupling between the memories and bus [51]. We have verified that including these does not change the main conclusions of this work. The  $\epsilon$ -dependence of the anharmonicities  $\eta$  and  $\eta'$ , and small anharmonic corrections to the interaction terms in (2.137), are also neglected.

The parameter values we use in our simulations are provided in Table 2.3. We assume  $\eta' = 3\eta$ , which is appropriate for cubic anharmonicity. The value of the bus coupling  $g_b$  is chosen to give the shortest CZ gate time for a range of fidelities (discussed later in detail). We simulate  $n = 4$  qubits. The fidelities quoted in here are numerically exact for the model (2.137); the rotating-wave approximation is not used.

Although the CZ and MOVE gates considered here do not involve microwave pulses, the single-qubit gates are assumed to be implemented with microwaves in the usual manner at the qubit frequency  $\omega_{\text{off}}$ . This frequency is also used to define an experimental “rotating” reference frame or local clock for each qubit: All qubit frequencies are defined relative to  $\omega_{\text{off}}$  [41], as discussed in Sec. 2.3.2.

## 2.4.2 System optimization for Controlled- $\sigma^z$ gate

In this section we discuss an approach for choosing optimal QVN $_n$  device parameters. This is a complex global optimization problem that we will solve in a simple but approximate way, emphasizing the main ideas of the procedure instead of its most precise implementation.

First we consider resonator frequencies. The QVN $_n$  processor includes  $n$  memory resonators, with frequencies  $\omega_{m1}, \omega_{m2}, \dots$ . These need to be mutually detuned (to lift degeneracies), and for simplicity we space them by 100 MHz (a smaller value could be used). The band of memory frequencies itself needs to be well detuned from the bus to keep the idle error (to be discussed below) in check.

Because the qubit frequency during a qubit-bus CZ gate must approach the bus frequency from above (Sec. 2.3.8), the bus frequency must be below the memory band. The choice of bus frequency therefore determines the lowest transition frequency that needs to be accessible by a qubit. Specifically, the qubits will need to tune 500 MHz or so below the bus. However, the minimum transition frequency may be constrained by qubit design (in addition to other considerations). In the tunable- $E_J$  transmon, for example, this minimum frequency

depends on the qubit anharmonicity  $\eta$ . Here we will choose a minimum qubit frequency and corresponding bus frequency appropriate for a transmon with 300 MHz anharmonicity. This leads to our choice of 6.5 GHz for the bus frequency. Optimal resonator frequencies for smaller  $\eta$  are unchanged, whereas for larger  $\eta$  they need to be rigidly shifted upward in frequency. In particular, system frequencies for a 400 MHz transmon will be shifted upward in frequency by about 2 GHz. Apart from this large but simple change, we expect the system optimization results, such as  $g_b$  values, to be valid for the 400 MHz case as well.

The frequency  $\omega_{\text{off}}$  can be viewed as defining a boundary between **MOVE** and **CZ** gates, or between consecutive **MOVE** gates. It is also natural to perform single-qubit operations with microwave pulses at the qubit frequency  $\omega_{\text{off}}$ . If  $\omega_{\text{off}}$  is too low, the error of the (approximate two-parameter) **MOVE** to/from memory gate becomes significant (this is determined by the qubit-bus detuning because the dominant error is nonadiabatic leakage to the bus), whereas if  $\omega_{\text{off}}$  is too high the fidelity of the qubit-bus **CZ** degrades (because  $d\epsilon/dt$  increases). We find that 7.5 GHz works well. At least 500 MHz is required between  $\omega_{\text{off}}/2\pi$  and the memory band to keep the **MOVE** errors (to/from the bus) under control. Thus we arrive at the memory frequencies given in Table 2.3.

Having obtained prospective resonator frequencies, we turn to couplings. The most frequently used gate is expected to be the **MOVE** to/from memory, which must be as fast as possible. The gate time for this operation is approximately

$$\frac{\pi}{2g_m} + t_{\text{ramp}} + 1 \text{ ns}. \quad (2.139)$$

The first term is the  $\pi$  rotation time, and the second and third are switching times (the detuning ramp can be fast because the qubit is unoccupied). Choosing  $g_m/2\pi = 100$  MHz makes the first term 2.5 ns. It might be possible to increase  $g_m$  further, but suppressing the resulting idling error (see below) would require an even higher empty-qubit parking fre-

quency. The value of  $t_{\text{ramp}}$  is determined by the desired MOVE gate fidelity. Because the dominant error is nonadiabatic excitation of the bus, we can estimate it using our expression (2.96) for the switching error  $p_{\text{sw}}$ , with  $G = g_{\text{b}}$ ,  $\Delta_{\text{on}}/2\pi = 1.0$  GHz, and  $\Delta_{\text{off}}/2\pi = 1.8$  GHz (corresponding to  $m_4$ , the worst case). These values depend on our initial resonator frequency assignments. From Fig. 2.11 we obtain  $|A|^2 = 0.03$  ( $9.8 \times 10^{-4}$ ) for a 1 ns (2 ns) ramp. Considering the largest (worst case) value for  $g_{\text{b}}/2\pi$  of 60 MHz gives  $p_{\text{sw}} = 1.1 \times 10^{-4}$  ( $3.5 \times 10^{-6}$ ) for a 1 ns (2 ns) ramp. Thus we conclude that the MOVE to/from memory can be done in about 5 ns if  $g_{\text{m}}/2\pi = 100$  MHz. (Here we assumed the simplest 2+1-parameter MOVE to/from memory gate, having two pulse-shape parameters and one auxiliary  $z$  rotation angle. It is also possible to implement this gate with even higher fidelity with 4+1 parameters [42].)

The bus coupling is found by the following “ $g$ -optimization” procedure: Consider the set of discretized  $g_{\text{b}}/2\pi$  values, varying from 10 to 100 MHz in steps of 1 MHz. For each value of  $g_{\text{b}}$ , calculate the minimum value of  $t_{\text{ramp}}$  and the associated  $t_{\text{gate}}$  required to achieve a target fidelity, say 99.9%. We do this by stepping through  $t_{\text{ramp}}$  values, estimating the fidelity using (2.96) and (2.103) from Sec. 2.3.6, which is very efficient, then confirming through a full optimization on  $\text{QVN}_1$ . We then obtain, for each  $g_{\text{b}}$ , the gate time of a 99.9% CZ gate, or equivalently, the function

$$t_{\text{gate}}^{(99.9\%)}(g_{\text{b}}). \quad (2.140)$$

The function (2.140) gives the time required for a CZ gate with a given target fidelity as a function of  $g_{\text{b}}$ . Strict  $g$ -optimization requires choosing  $g_{\text{b}}$  to minimize  $t_{\text{gate}}$ , and this procedure leads to the best performance in any given situation.

Having obtained prospective resonator frequencies and couplings, we choose the empty qubit parking frequency  $\omega_{\text{park}}$  to control the idle error

$$\mathbb{E} = (\Omega_{\text{ZZ}}t)^2 n^2, \quad (2.141)$$

where  $\Omega_{ZZ}$  is the effective  $\sigma^z \otimes \sigma^z$  coupling frequency between a memory resonator and the bus, induced by their shared qubit [42]. The  $n$ -dependence in (2.141) assumes the worst case. Assuming  $\omega_{\text{park}}/2\pi = 10$  GHz,  $g_{\text{b}}/2\pi = 60$  MHz (the worst case), and  $\eta/2\pi = 400$  MHz (also the worst case) leads to

$$\frac{\Omega_{ZZ}}{2\pi} = -0.881 \text{ kHz}. \quad (2.142)$$

It will be necessary to keep (2.141) less than the fault-tolerant threshold during a (potentially) long error correction cycle. If we assume  $t = 1 \mu\text{s}$ , the idle error in  $\text{QVN}_4$  is  $4.9 \times 10^{-4}$ , which is acceptable. Reducing the parked qubit frequency to 9.5 GHz (9.0 GHz) increases the idle error to  $3.8 \times 10^{-3}$  ( $7.3 \times 10^{-2}$ ).

We are now able to calculate the gate time of the **MOVE** to/from bus operation. The gate time is approximately

$$\frac{\pi}{2g_{\text{b}}} + t_{\text{ramp}} + 1 \text{ ns}, \quad (2.143)$$

where the first term is between 4 and 8 ns for the bus couplings considered in this work. As before,  $t_{\text{ramp}}$  is determined by the desired gate fidelity. The dominant error is nonadiabatic transition to memory, which we estimate using (2.96) with  $G = g_{\text{m}}$ ,  $\Delta_{\text{on}}/2\pi = 0.5$  GHz (the worst case), and  $\Delta_{\text{off}}/2\pi = 1.5$  GHz. Note that this error is enhanced by the large value of  $g_{\text{m}}$ . From Fig. 2.11 we obtain  $|A|^2 = 5.9 \times 10^{-2}$  ( $1.6 \times 10^{-2}$ ) for a 2 ns (3 ns) ramp. Then  $p_{\text{sw}} = 2.4 \times 10^{-4}$  ( $6.4 \times 10^{-4}$ ) for a 2 ns (3 ns) ramp. Thus we conclude that the **MOVE** to/from bus takes between 7 and 12 ns, depending on the actual value of  $g_{\text{b}}$  and on the desired fidelity.

Finally, we confirm that the assumed qubit parameters are compatible with transmons. In the large  $E_{\text{J}}/E_{\text{C}}$  transmon regime, the qubit frequency  $\epsilon$  and anharmonicity  $\eta$  are given by [13]

$$\epsilon = \sqrt{8E_{\text{J}}E_{\text{C}}} - E_{\text{C}} \quad (2.144)$$

and

$$\eta = E_{\text{C}}. \quad (2.145)$$

We assume a split-junction flux-biased Cooper-pair box so that  $E_J$  is tunable [40]. (Note that the tunable- $E_J$  transmon is sensitive to flux noise, which will degrade  $T_2$ .) Combining (2.144) and (2.145) leads to the relation  $\epsilon = \eta(\sqrt{8E_J/E_C} - 1)$  plotted in Fig. 2.12 for 300 and 400 MHz anharmonicity. Because  $E_J/E_C$  needs to be above about 50 to effectively suppress charge noise, we see that the 300 MHz transmon can have a transition frequency as small as 5.5 GHz, whereas the 400 MHz transmon has a minimum frequency of about 7.5 GHz. Our choice of bus frequency is indeed consistent with the 300 MHz transmon, whereas  $\omega_b/2\pi$  and the entire spectrum of device frequencies would have to be increased by about 2 GHz for the 400 MHz transmon.

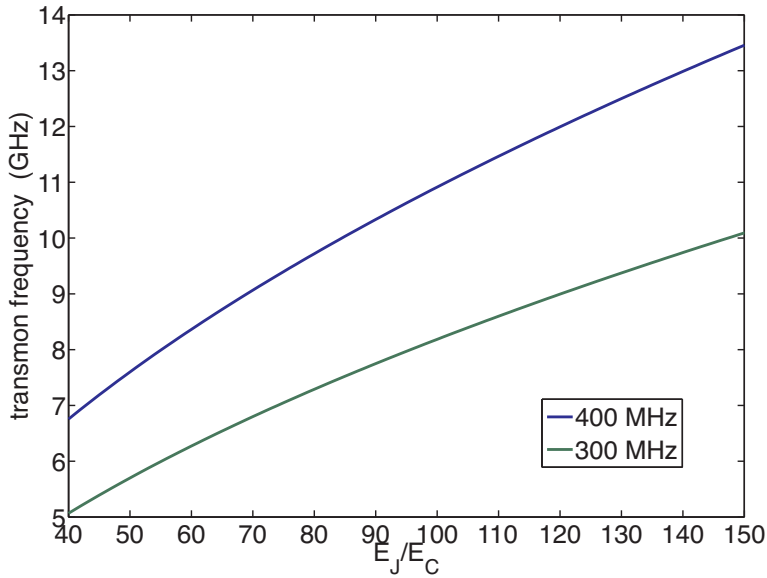


**Figure 2.12:** (Color online) Transition frequency for transmon with 300 and 400 MHz anharmonicity.

### 2.4.3 Controlled- $\sigma^z$ between a qubit and bus

Here I discuss the performance of our CZ gate between a qubit and the bus resonator of QVN architecture. We find that very high intrinsic fidelities—in the range of 99.9% to 99.99% and with corresponding total gate times in the range of 17 to 23 ns—can indeed be obtained with

a four-parameter gate. Two control parameters are pulse-shape parameters and two are auxiliary local  $z$  rotation angles. We emphasize that only low-frequency pulses are required, and that the number of control parameters does not depend on the number of qubits in the QVN device. The results quoted above assume four phase or transmon qubits with 300 MHz anharmonicity; other values of anharmonicity are considered below. The CZ gate referred to here is between qubit  $q_1$  and the bus (see Fig. 2.7), not between a pair of qubits as is usually considered.

**Table 2.5:** Optimal state-averaged process fidelity  $F_{\text{ave}}$  for the Strauch CZ gate between qubit  $q_1$  and the bus, in the QVN<sub>4</sub> processor of Fig. 2.7. No decoherence or noise is included here. Specifications for 99.9% and 99.99% gates are provided for three values of qubit anharmonicity  $\eta$ . The parameters  $t_{\text{ramp}}$  and  $\sigma$  characterize the pulse switching time, and  $t_{\text{gate}}$  is the total gate time excluding auxiliary  $z$  rotations.  $F_{|11\rangle}$  is the minimum fidelity, which is also the fidelity of the  $|11\rangle$  state if it is occupied initially. Data after double vertical lines give the nonadiabatic switching error and minimum fidelity estimates; these quantities are defined and discussed in Sec. 2.3.6.

$\eta/2\pi$	$g_b/2\pi$	$g_m/2\pi$	$t_{\text{on}}^{\text{sudden}}$	$t_{\text{ramp}}$	$\sigma$	$t_{\text{on}}$	$t_{\text{gate}}$	$F_{\text{ave}}[\%]$	$F_{ 11\rangle}[\%]$	$ A ^2$	$p_{\text{sw}}$	$F_{ 11\rangle}^{(\text{est})}[\%]$
200 MHz	30 MHz	100 MHz	11.8 ns	11 ns	1.94 ns	15.8 ns	26.8 ns	99.901	99.613	$2.1 \times 10^{-2}$	$1.5 \times 10^{-3}$	99.692
				16 ns	2.83 ns	18.3 ns	34.3 ns	99.992	99.975	$2.8 \times 10^{-3}$	$2.0 \times 10^{-4}$	99.960
300 MHz	45 MHz	100 MHz	7.9 ns	7 ns	1.24 ns	9.9 ns	16.9 ns	99.928	99.714	$1.7 \times 10^{-2}$	$1.2 \times 10^{-3}$	99.761
				11 ns	1.94 ns	11.8 ns	22.8 ns	99.995	99.979	$9.9 \times 10^{-4}$	$7.2 \times 10^{-5}$	99.986
400 MHz	60 MHz	100 MHz	5.9 ns	5 ns	0.88 ns	7.0 ns	12.0 ns	99.950	99.804	$1.4 \times 10^{-2}$	$1.0 \times 10^{-3}$	99.799
				7 ns	1.24 ns	7.8 ns	14.8 ns	99.991	99.966	$2.1 \times 10^{-3}$	$1.5 \times 10^{-4}$	99.970

The frequency diagram of the CZ gate between the qubit and bus is given in Fig. 2.13 and our main results are given in Table 2.5. Here  $\eta$  is the qubit anharmonicity. The 200 MHz results apply to the phase qubits of Ref. [41], while the larger anharmonicities might be relevant for future implementations with transmons. The bus couplings  $g_b$  are determined by the “ $g$  optimization” procedure described in Sec. 2.4.2, which leads to the simple formula

$$\frac{g_b}{\eta} = 0.15, \quad (2.146)$$

for the (approximately) optimal bus coupling. QVN <sub>$n$</sub>  refers to a quantum von Neumann processor with  $n$  qubits coupled to  $n$  memory resonators and a bus; the Hamiltonian for

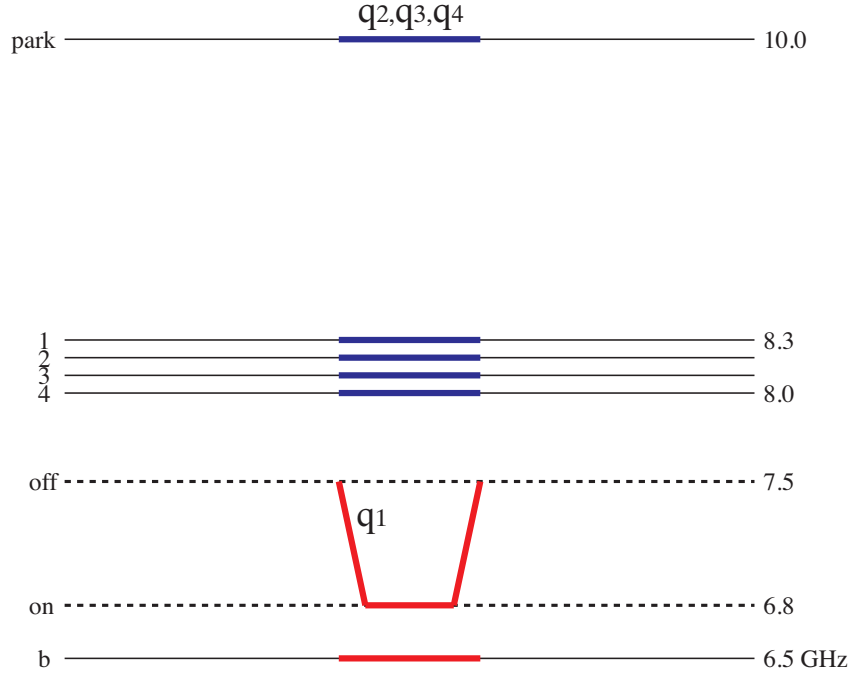


**Figure 2.13:** (Color online) Frequency diagram for the CZ gate between  $q_1$  and bus. This diagram describes the gate of Table 2.5. The lines 1–4 correspond to 4 memory resonators and horizontal axis corresponds time.

such a device is discussed in Sec. 2.4.1. As indicated in Table 2.5, the memory resonators are always strongly coupled to allow for fast (less than 5 ns) MOVE operations in and out of memory. CZ fidelities well above 99.99% are also obtainable (see below). Table 2.5 shows that the time required for a qubit-bus CZ gate with fixed intrinsic fidelity is inversely proportional to the qubit anharmonicity, namely

$$t_{\text{gate}}^{(99.9\%)} \approx \frac{5.2}{\eta/2\pi} \quad \text{and} \quad t_{\text{gate}}^{(99.99\%)} \approx \frac{6.7}{\eta/2\pi}. \quad (2.147)$$

These expressions indicate that CZ gates with very high intrinsic fidelity can be implemented in about 20 ns with existing superconducting qubits, a conclusion which applies not only to  $\text{QVN}_n$  but also to a wide range of similar resonator-based architectures. The intrinsic gate (or process) fidelity  $F_{\text{ave}}$  is the squared overlap of ideal and realized final states, averaged over initial states (see Sec. 2.1). By *intrinsic* we mean that noise and decoherence are not included in the gate simulation. The fidelity estimate is developed in Sec. 2.3.6. The results given in Table 2.5 apply specifically to the  $n=4$  processor, but similar results are expected for other (not too large) values of  $n$ . Two strategies are critical for obtaining this high performance: Separating two control parameters in the form of auxiliary local  $z$  rotations, and defining the computational states in terms of *interacting* system eigenfunctions. These strategies were used in Ref. [42] and are discussed in more detail below. The gate fidelities achievable with a transmon-based QVN device are in line with that required for fault-tolerant quantum computation with topological stabilizer codes [52, 53]. Qubit anharmonicity is an important resource that will help us achieve that goal.

My main focus in this thesis has been the CZ gate between qubit  $q_1$  and the bus in the  $\text{QVN}_4$  processor. Results for the other qubits are very similar, with the worst case being  $q_4$ , because the detuning to memory during the gate is slightly smaller. We find that the intrinsic fidelity of the 99.9% CZ gate for the 300 MHz qubit given in Table 2.5 changes from 99.928% to 99.925% if qubit  $q_4$  is used instead of  $q_1$ .

Higher fidelities are also possible with the pulse shape (2.69) if we increase the adiabaticity. An example is provided in Table 2.6 for the 300 MHz qubit. For this design we did not perform a separate  $g_b$  optimization for this higher fidelity, but instead used the value from Table 2.5 optimized for the lower fidelities.

**Table 2.6:** Optimal QVN<sub>4</sub> gate fidelity for a Strauch CZ gate between qubit  $q_1$  and the bus.

$\eta/2\pi$	$g_b/2\pi$	$g_m/2\pi$	$t_{\text{ramp}}$	$\sigma$	$t_{\text{gate}}$	$F_{\text{ave}}$
300 MHz	45 MHz	100 MHz	13 ns	2.30 ns	25.7 ns	99.999%

#### 2.4.4 Controlled- $\sigma^z$ between two qubits

In this section I explain how to perform a CZ gate between two qubits—or more precisely, between two *memories*—in the QVN architecture. Such an operation is not elementary, as it can be composed of the qubit-bus CZ combined with MOVE gates. (There are also proposals for the direct implementation of a qubit-qubit CZ gate in a QVN device [54, 55].) Figure 2.14 shows the experimental protocol for implementing the gate CZ<sub>23</sub> between qubits  $q_2$  and  $q_3$ , suppressing auxiliary  $z$  rotations, and with all data starting and ending in memory. This mode diagram shows the time-dependence of all 9 device frequencies. The color indicates whether the qubit or resonator would be in the ground state (blue) or possibly excited state (red) in the weakly coupled limit. Modes are colored red if there is a finite occupation of the  $|1\rangle$  state (in the weakly coupled limit), for some choice of initial conditions. All qubits are initially parked at the strongly detuned frequency of 10 GHz. Horizontal lines 1-4 represent memories, and  $b$  is the bus. No red or red and blue lines with first-order *or* second-order couplings cross (to avoid Landau-Zener transitions), and no more than one qubit is occupied at any time (to avoid second-order qubit-qubit interactions mediated by the bus).

Beginning with the four memory registers in an arbitrary (possibly entangled) state, the bus is loaded by a 5 ns MOVE gate from  $m_3 \rightarrow q_3$  followed by a 10 ns MOVE to the bus. These are approximate gate times (time estimates for these gates are given in Sec. 2.4.2 and a concrete example is provided below). Qubit  $q_2$  is then loaded and tuned to the frequency  $\omega_{\text{on}}$  determined by optimization. This central portion of the gate is close but not exactly the

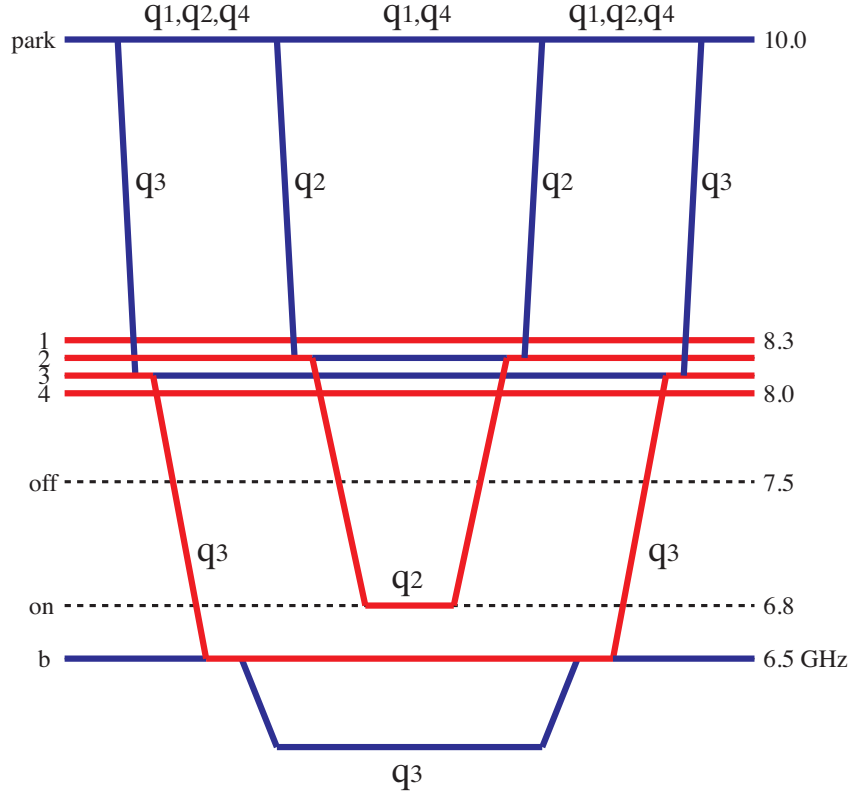


**Figure 2.14:** (Color online) QVN<sub>4</sub> mode diagram for the CZ<sub>23</sub> gate. Gaussian filtering of the pulse is not shown.

same as the qubit-bus CZ gate of Table 2.5 (See Fig. 2.13 for comparison).

We simulated the gate CZ<sub>23</sub> shown in Fig. 2.14, using the 99.99% CZ of Table 2.5 for a 300 MHz qubit, and starting with the memory register in the GHZ state

$$\frac{\overline{|0000\rangle} + \overline{|1111\rangle}}{\sqrt{2}}. \quad (2.148)$$

The MOVE gates also have fidelities around 99.99%. Note that  $H_{\text{idle}}$  and the associated

computational basis states (interacting eigenfunctions of  $H_{\text{idle}}$ ) are different at the beginning and end of each **MOVE** gate. The total **CZ**<sub>23</sub> gate time is

$$t_{\text{gate}} = 55 \text{ ns}, \quad (2.149)$$

and the final state fidelity (overlap squared) is

$$F = 99.94\%. \quad (2.150)$$

In addition to the 23 ns qubit-bus **CZ** gate, there are four **MOVE** to/from memory operations, each taking about 3.5 ns, and two **MOVE** to/from bus gates, each taking about 9 ns. There are also local  $z$  rotations (not shown) between each gate.

A few remarks about the encouraging result (2.150) are in order: The seven elementary gates making up the **CZ**<sub>23</sub> operation are optimized individually to an error of about  $10^{-4}$ , and then combined without any additional optimization of the composite pulse sequence or control parameters, respecting the modularity required by scalable, gate-based quantum computation. And the total intrinsic error  $\mathbb{E} \equiv 1 - F = 6 \times 10^{-4}$  implied by (2.150) is consistent with a linear (incoherent) accumulation of errors with number of elementary steps  $\mathbb{E}_{\text{inc}} \cong 7 \times 10^{-4}$ , but is not consistent with a quadratic (coherent) accumulation  $\mathbb{E}_{\text{coh}} \cong 7^2 \times 10^{-4}$ .

# Chapter 3

## Ancilla-assisted Qubit Measurement

*Observations not only disturb what is to be measured, they produce it.*

– Pascual Jordan

In this chapter, I explore the signature and consequences of leakage errors on ancilla-assisted Pauli operator measurement in superconducting devices. We consider a realistic coupled-qutrit model and simulate the repeated measurement of a single  $\sigma^z$  operator. Such a measurement process consists of a single CZ and two pre and post Hadamard gates, and in this work we parameterize the CZ gate discussed in the previous chapter. Typically, a data-qubit leakage event manifests itself by producing a “noisy” ancilla qubit that randomly reads  $|0\rangle$  or  $|1\rangle$  from cycle to cycle. Although the measurement operation is compromised, the presence of the leakage event is apparent and detectable. However, there is also the possibility of a less typical but more dangerous type of leakage event, where the ancilla becomes *paralyzed*, rendering it oblivious to data-qubit errors for many consecutive measurement cycles and compromising the fault-tolerance. Certain dynamical phases associated with the entangling gate determine which type of leakage event will occur in practice. Leakage errors occur in most qubit realizations and our model and results are especially relevant for stabilizer-based topological error-correcting codes.

Topological quantum error-correcting codes (discussed in the next chapter), such as surface and toric codes, are attracting attention because of their high error thresholds and realistic designs that only require nearest-neighbor interactions [52, 53, 56–58]. While the robustness of standard fault-tolerant topological codes to discrete Pauli errors is a subject of active research [45, 59–61], the effect of leakage to non-computational states still remains an open question and is relevant for most quantum computing architectures. Understanding the effect of such leakage errors is important for superconducting qubits not only because higher energy states  $|2\rangle, |3\rangle, \dots$  are present, as is the case with most other qubit realizations, but also because they can be utilized to implement two-qubit entangling operations such as the Strauch CZ gate [16, 62]. One way to suppress the effects of leakage is to adopt the topological cluster-state approach [52, 58, 63], where each qubit is repeatedly initialized, operated on by gates, and measured: This approach systematically removes leakage errors from all qubits in the array, at the cost of some additional operations. Another approach might be to use a stabilizer-based topological error-correcting code for *qudits*, and theoretical progress has been made in this direction [64–70].

In this chapter, however, we consider the standard stabilizer-based approach for qubits—but applied to three-level qutrits—and regard any population transfer to the  $|2\rangle$  state of the ancilla or data qutrit as a potential error. We investigate the origin and signature of such leakage errors for an ancilla-assisted measurement of the data qutrit, identify a potentially dangerous regime where data errors are invisible to the ancilla, and discuss its consequences for topological error correction. We describe the ideal measurement protocol in Sec. 3.1. In Sec. 3.2 we describe our physical model and consider ancilla-assisted measurement in the presence of decoherence. The non-ideal CZ gate is discussed in Sec. 3.3.1. Leakage errors and ancilla paralysis are discussed in Sec. 3.3.2. We discuss the implications of our results for the design of error-corrected superconducting quantum computers in Sec. 3.4.

## 3.1 Measurement protocol

In this section, I describe the measurement circuit first and then discuss how an ancilla-assisted measurement works ideally in absence of any error.

### 3.1.1 Measurement circuit

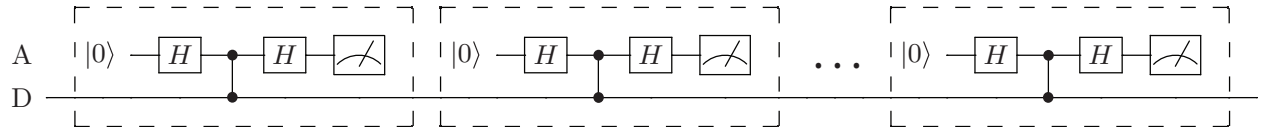


**Figure 3.1:** Protocol for ancilla-assisted  $\sigma^z$  measurement.

Figure 3.1 shows the circuit for our protocol. Here “A” is the ancilla qubit and “D” the data qubit. Each cycle (shown by dashed box) consists of a reset of the ancilla to the  $|0\rangle$  state, a Hadamard gate H on the ancilla, a CZ gate, and another Hadamard followed by ancilla readout in the diagonal basis. The readout result is recorded and the cycle is repeated indefinitely. The data qubit never gets measured or reset.

### 3.1.2 Ideal case

Let’s now review how this circuit 3.1 works in the ideal limit: Initially, the data qutrit D is assumed to be in some pure qubit (not qutrit) state

$$|\psi_D\rangle = a|0\rangle + b|1\rangle, \quad (3.1)$$

while the ancilla A is initialized to  $|0\rangle$ . We perform the gate operations shown, record the measurement outcome, reset the ancilla to  $|0\rangle$ , and repeat this cycle many times. Throughout this work, the Hadamard gate (H) is assumed to be ideal and to act as the identity on the

third level of the qutrit,

$$H \equiv \begin{bmatrix} \frac{1}{\sqrt{2}} & \frac{1}{\sqrt{2}} & 0 \\ \frac{1}{\sqrt{2}} & -\frac{1}{\sqrt{2}} & 0 \\ 0 & 0 & 1 \end{bmatrix}. \quad (3.2)$$

The Hadamards and CZ combine to produce a CNOT gate that copies the data qubit to the ancilla, but here we implement this CNOT with the gates shown in Fig. 3.1 because we believe that the CZ gate can be implemented in superconducting architectures with very high fidelity, as discussed in the last chapter [62]. For an initial D state (3.1), the state of the system after the second H gate is, in the  $|AD\rangle$  basis,

$$a|00\rangle + b|11\rangle. \quad (3.3)$$

Thus, in the absence of any errors, the readout projects the data qubit into the observed eigenstate of the ancilla. And once the data qubit is projected to a computational basis state, it remains there forever.

## 3.2 Coupled qutrit model

In this section we describe our model, and for a warm-up, show how the ancilla-assisted measurement protocol works with ideal gates, but in the presence of decoherence.

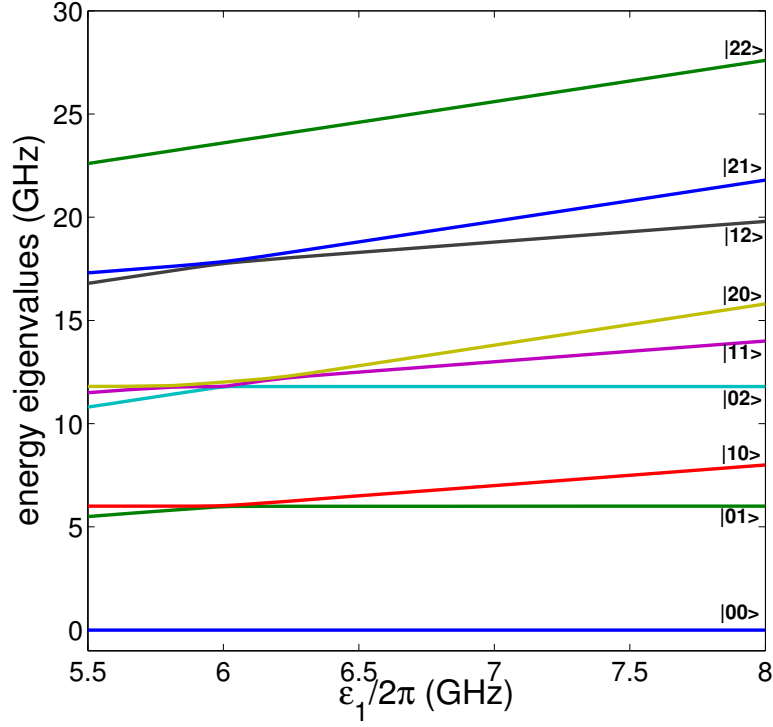


**Figure 3.2:** (Color online) Energies of various levels, in the  $|AD\rangle$  basis, as a function of  $\epsilon_1/2\pi$ . Here  $\epsilon_2/2\pi = 6$  GHz, the coupling strength is  $g/2\pi = 25$  MHz, and  $\eta_1/2\pi = \eta_2/2\pi = 200$  MHz.

### 3.2.1 Hamiltonian

The Hamiltonian for a pair of capacitively coupled transmon or phase qutrits is given by

$$H(t) = \begin{bmatrix} 0 & 0 & 0 \\ 0 & \epsilon_1 & 0 \\ 0 & 0 & 2\epsilon_1 - \eta_1 \end{bmatrix}_{q_1} + \begin{bmatrix} 0 & 0 & 0 \\ 0 & \epsilon_2 & 0 \\ 0 & 0 & 2\epsilon_2 - \eta_2 \end{bmatrix}_{q_2} + g Y \otimes Y, \quad (3.4)$$

where

$$Y \equiv \begin{bmatrix} 0 & -i & 0 \\ i & 0 & -i\sqrt{2} \\ 0 & i\sqrt{2} & 0 \end{bmatrix}. \quad (3.5)$$

Qutrit 1 is the ancilla qutrit and qutrit 2 is the data qutrit. In (3.5) we have assumed harmonic qutrit eigenfunctions. The time-dependence of the Hamiltonian (3.4) is embedded in the qubit frequencies  $\epsilon_1$  and  $\epsilon_2$ ; the Hadamard gates are implemented with microwaves via terms not shown in (3.4). For the CZ gate protocol, we assume the frequency of the data qubit to be fixed at 6 GHz, while the ancilla's frequency is varied. The anharmonicities  $\eta_i/2\pi$  are assumed to be equal, frequency-independent, and fixed at 200 MHz. Figure 3.2 shows the energies of several relevant eigenstates as a function of  $\epsilon_1$ , with  $\epsilon_2/2\pi = 6$  GHz and coupling strength  $g/2\pi = 25$  MHz. Note that the only anticrossing at  $\epsilon_1 = \epsilon_2 + \eta_1$  ( $\epsilon_1/2\pi = 6.2$  GHz in Fig. 3.2) is between the  $|11\rangle$  and  $|20\rangle$  channels; we use this anticrossing for our CZ gate [16, 62].

### 3.2.2 Parameterizing ideal Controlled- $\sigma^z$ gate

The CZ gate, both ideal and non-ideal, is parameterized in this work via its *generator*. A generator of any unitary matrix  $U$  is defined as a Hermitian matrix  $S$  such that  $U = e^{iS}$ . For a two-qutrit system, the generator of the ideal CZ gate is a Hermitian matrix  $S$ , whose matrix representation in the basis

$$|\text{AD}\rangle = \{ |00\rangle, |01\rangle, |02\rangle, |10\rangle, |11\rangle, |12\rangle, |20\rangle, |21\rangle, |22\rangle \} \quad (3.6)$$

is

$$S = \begin{bmatrix} 0 & 0 & 0 & 0 & 0 & 0 & 0 & 0 & 0 \\ 0 & 0 & 0 & 0 & 0 & 0 & 0 & 0 & 0 \\ 0 & 0 & \xi_1 & 0 & 0 & 0 & 0 & 0 & 0 \\ 0 & 0 & 0 & 0 & 0 & 0 & 0 & 0 & 0 \\ 0 & 0 & 0 & 0 & \pi & 0 & 0 & 0 & 0 \\ 0 & 0 & 0 & 0 & 0 & \xi_2 & 0 & 0 & 0 \\ 0 & 0 & 0 & 0 & 0 & 0 & \pi & 0 & 0 \\ 0 & 0 & 0 & 0 & 0 & 0 & 0 & \xi_3 & 0 \\ 0 & 0 & 0 & 0 & 0 & 0 & 0 & 0 & \xi_4 \end{bmatrix}. \quad (3.7)$$

Note that within the computational subspace,  $e^{iS}$  acts as a standard CZ gate, while non-computational basis states acquire phases  $e^{i\xi_i}$ . We emphasize that any extension of an ideal CZ gate to qutrits is dependent on the assumed model and gate protocol. For the Strauch CZ gate, auxiliary  $\sigma^z$  rotations on the ancilla and data qubits nullify the phases acquired by the  $|01\rangle$  and  $|10\rangle$  channels. Since we use the anticrossing between  $|11\rangle$  and  $|20\rangle$ , they acquire a phase of angle  $\pi$ . We assume that the gate is in the adiabatic regime, and that the parameters  $\xi_i$  are dynamical phases, which can then be expressed as

$$\begin{aligned} \xi_1 &\approx - \int_0^{t_{\text{gate}}} E_{02} dt = - \int_0^{t_{\text{gate}}} (2\epsilon_2 - \eta_2) dt, \\ \xi_2 &\approx - \int_0^{t_{\text{gate}}} E_{12} dt = - \int_0^{t_{\text{gate}}} (2\epsilon_2 - \eta_2) dt - \int_0^{t_{\text{gate}}} \epsilon_1 dt, \\ \xi_3 &\approx - \int_0^{t_{\text{gate}}} E_{21} dt = - \int_0^{t_{\text{gate}}} \epsilon_2 dt - \int_0^{t_{\text{gate}}} (2\epsilon_1 - \eta_1) dt, \\ \xi_4 &\approx - \int_0^{t_{\text{gate}}} E_{22} dt = - \int_0^{t_{\text{gate}}} (2\epsilon_2 - \eta_2) dt - \int_0^{t_{\text{gate}}} (2\epsilon_1 - \eta_1) dt. \end{aligned} \quad (3.8)$$

Here  $t_{\text{gate}}$  is the operation time for the CZ gate (including auxiliary  $z$  rotations), and  $E_{ij}$  is the energy of eigenstate  $|ij\rangle$ , shown in Fig. 3.2. To keep our analysis general we do not assume specific values for the  $\xi_i$ . They depend on the details of the CZ gate implementation but remain fixed throughout a given experiment or simulation (unless one changes  $t_{\text{gate}}$  or the pulse shape). As we will explain below, the difference

$$\theta \equiv \xi_2 - \xi_1 = - \int_0^{t_{\text{gate}}} \epsilon_1 dt \quad (3.9)$$

determines if the ancilla becomes paralyzed during a leakage event. Note that  $\theta$  can be varied during an experiment by changing the gate time.

### 3.2.3 Ancilla-assisted measurement with decoherence

As shown in Fig. 3.1, each measurement cycle consists of ancilla initialization, three gate operations, and ancilla readout. Assuming ideal gates, the data qutrit after the first cycle is projected to a computational  $|0\rangle$  or  $|1\rangle$  state depending on the observed state of the ancilla [recall (3.3)]. In the absence of any errors, the measurement outcome of the ancilla remains unaltered thereafter. However, the situation is different in the presence of decoherence.

In order to model the effects of decoherence on the measurement outcomes of the ancilla, we assume that the readout and reset operations are instantaneous, while the Hadamard and CZ gates take 10 and 25 ns respectively. We also assume that amplitude damping is the only source of decoherence, in which case the single-qutrit Kraus matrices can be written as

$$E_1 = \begin{bmatrix} 1 & 0 & 0 \\ 0 & \sqrt{1-\lambda_1} & 0 \\ 0 & 0 & \sqrt{1-\lambda_2} \end{bmatrix}, \quad E_2 = \begin{bmatrix} 0 & \sqrt{\lambda_1} & 0 \\ 0 & 0 & 0 \\ 0 & 0 & 0 \end{bmatrix}, \quad E_3 = \begin{bmatrix} 0 & 0 & \sqrt{\lambda_2} \\ 0 & 0 & 0 \\ 0 & 0 & 0 \end{bmatrix}. \quad (3.10)$$

For an operation of time duration  $\Delta t$ ,

$$\lambda_m = 1 - e^{-m \Delta t / T_1}. \quad (3.11)$$

These Kraus operators [9] describe the time-evolution of a single-qutrit density matrix  $\rho$  as,

$$\rho \rightarrow \sum_{k=1}^3 E_k \rho E_k^\dagger. \quad (3.12)$$

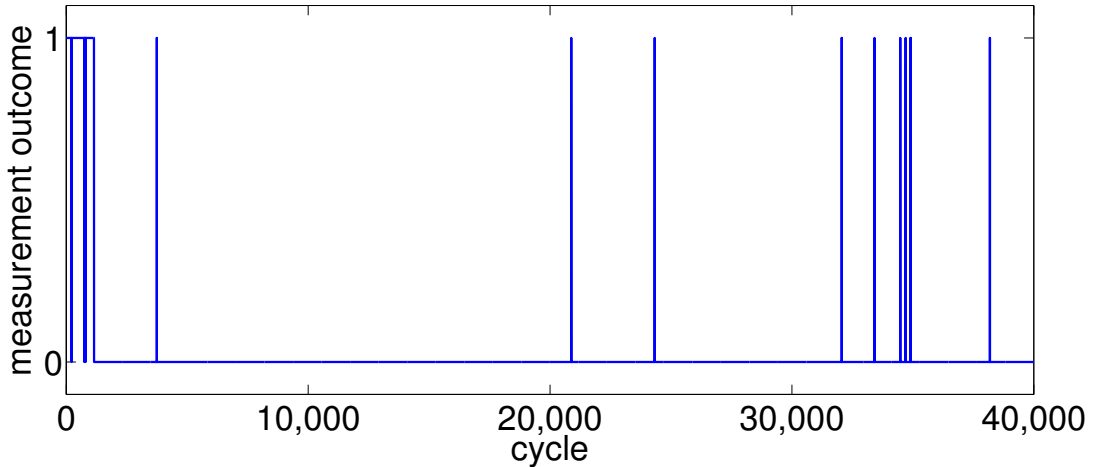


**Figure 3.3:** (Color online) Simulated repeated readout of the ancilla qutrit in the presence of amplitude damping. Single peaks, upward or downward, indicate errors on the ancilla. Data errors result in steps; an example is shown near cycle 1000. In this simulation we assume  $T_1 = 40 \mu\text{s}$ ,  $T_2 = 2T_1$ , and  $t_{\text{cycle}} = 45 \text{ ns}$ .

We simulate the ancilla-assisted measurement protocol for an ideal CZ gate but in the presence of decoherence, for 40,000 consecutive cycles, and Fig. 3.3 shows a typical outcome. The duration  $t_{\text{cycle}}$  of each complete measurement cycle is 45 ns (one CZ gate plus two Hadamards). Initially, the data qutrit is in state  $|1\rangle$ , and a single downward peak denotes an error on the ancilla. Near the 1000<sup>th</sup> cycle the data qutrit relaxes to  $|0\rangle$  due to decoherence, and once in the ground state it stays there forever. The remaining upward peaks are caused by decoherence on the ancilla qutrit. Since the ancilla gets reset at the end of every cycle,

such errors are manifested as single peaks. Note that if the initial state of the two-qutrit system is inside the computational subspace, it does not leak to non-computational states and therefore Fig. 3.3 is insensitive to the values of the  $\xi_i$ .

### 3.3 Non-ideal Controlled- $\sigma^z$ gate

In this section, I first discuss how a non-ideal CZ gate is parameterized and then investigate its action on the ancilla-assisted qubit measurement.

#### 3.3.1 Parameterization of non-ideal Controlled- $\sigma^z$ gate

Let us first give a brief review of the dominant intrinsic error mechanisms that are relevant for the Strauch CZ gate [62]; the Hadamards are always assumed to be ideal [see (3.2)]. The CZ gate of Strauch *et al.* [16] is performed by using the anticrossing between the  $|11\rangle$  and  $|20\rangle$  states at  $\epsilon_1 = \epsilon_2 + \eta_1$ . Although the other states are detuned from each other at this anticrossing point, a small amount of nonadiabatic population transfer is unavoidable, and these nonadiabatic excitations dominate the intrinsic gate errors. These errors can be thought of as producing a second unitary matrix whose generator  $S'$  can be parameterized,

in the basis (3.6), as

$$S' = \begin{pmatrix} 0 & 0 & 0 & 0 & 0 & 0 & 0 & 0 & 0 \\ 0 & \zeta_1 & 0 & i\chi_1 e^{i\phi_1} & 0 & 0 & 0 & 0 & 0 \\ 0 & 0 & 0 & 0 & i\chi_2 e^{i\phi_2} & 0 & 0 & 0 & 0 \\ 0 & -i\chi_1 e^{-i\phi_1} & 0 & \zeta_2 & 0 & 0 & 0 & 0 & 0 \\ 0 & 0 & -i\chi_2 e^{-i\phi_2} & 0 & \zeta_3 & 0 & i\chi_3 e^{i\phi_3} & 0 & 0 \\ 0 & 0 & 0 & 0 & 0 & 0 & 0 & i\chi_4 e^{i\phi_4} & 0 \\ 0 & 0 & 0 & 0 & -i\chi_3 e^{-i\phi_3} & 0 & \zeta_4 & 0 & 0 \\ 0 & 0 & 0 & 0 & 0 & -i\chi_4 e^{-i\phi_4} & 0 & 0 & 0 \\ 0 & 0 & 0 & 0 & 0 & 0 & 0 & 0 & 0 \end{pmatrix}. \quad (3.13)$$

The complete non-ideal CZ gate is

$$U_{\text{CZ}} = e^{i(S+S')}, \quad (3.14)$$

where  $S$  is the generator (3.7) of the ideal CZ gate. The parameters  $\chi_i$  and  $\zeta_i$  in (3.13) are small, while the angles  $\phi_i$  take arbitrary values between 0 and  $2\pi$ .  $\zeta_1$  and  $\zeta_2$  parameterize the errors occurring during pre and post  $\sigma^z$  rotations, and  $\zeta_3$  and  $\zeta_4$  denote the controlled-phase error for the  $|11\rangle$  and  $|20\rangle$  channels. In our simulations we assume  $\chi_i = \zeta_i = 10^{-2}$  for all  $i = 1, \dots, 4$ . Because population transfer probability scales with  $|\chi_i|^2$ , our choice of parameters bounds the intrinsic gate errors to about  $10^{-4}$ .

### 3.3.2 Signature of data qubit leakage and ancilla paralysis

The CZ gate (3.14) produces, on any  $|11\rangle$  input component, a small amplitude of  $|02\rangle$  (the amount determined by  $\chi_2$ ) and  $|20\rangle$  (determined by  $\chi_3$ ). A  $|20\rangle$  component either results in the possibility of an ancilla readout of  $|2\rangle$ —if the readout protocol distinguishes  $|1\rangle$  and

$|2\rangle$ —or the possibility of an isolated ancilla error if it does not. Neither case compromises fault-tolerance. The parameter  $\chi_2$  is responsible for data qubit leakage events. By a leakage *event* we mean a near-unity population of the data  $|2\rangle$  state.

The principal mechanism producing a leakage event is the abrupt, nonlinear transformation on the data qutrit induced by the ancilla measurement. We denote these transformations by  $\mathbf{T}_0$ ,  $\mathbf{T}_1$ , and  $\mathbf{T}_2$ , where the subscript corresponds to the ancilla readout result. Repeatedly measuring the ancilla applies a random sequence of the  $\mathbf{T}$  maps to the data qutrit.

For the model, gate implementation, and parameter values considered in this work, the map  $\mathbf{T}_0$  is primarily responsible for the observed leakage events. Although the general form of  $\mathbf{T}_0$  is quite complex, it is possible to construct a simple special case of it that exhibits the essential features. To do this we choose simplified parameter values

$$\begin{aligned}
 \xi_1 &= \pi, \\
 \phi_i &= 0, \\
 \zeta_i &= 0, \\
 \chi_3 &= 0, \\
 \chi_4 &= 0,
 \end{aligned} \tag{3.15}$$

and calculate the action of the non-ideal measurement circuit on an arbitrary data qutrit state

$$|\psi_{\text{D}}\rangle = a|0\rangle + b|1\rangle + c|2\rangle. \tag{3.16}$$

We find (in the  $|AD\rangle$  basis) that

$$\begin{aligned}
& a|00\rangle + b|01\rangle + c|02\rangle \rightarrow |0\rangle \otimes \left[ \left( \frac{a}{2} + \frac{a}{2} \cos \chi_1 + \frac{b}{2} \sin \chi_1 \right) |0\rangle \right. \\
& + \left( \frac{b}{2} \cos \chi_1 - \frac{a}{2} \sin \chi_1 - \frac{b}{2} \cos \chi_2 - \frac{c}{2} \sin \chi_2 \right) |1\rangle + \left( \frac{c}{2} + \frac{b}{2} \sin \chi_2 \right. \\
& \left. \left. - \frac{c}{2} \cos \chi_2 \right) |2\rangle \right] + |1\rangle \otimes \left[ \left( \frac{a}{2} - \frac{a}{2} \cos \chi_1 - \frac{b}{2} \sin \chi_1 \right) |0\rangle + \left( \frac{b}{2} \cos \chi_1 \right. \right. \\
& \left. \left. - \frac{a}{2} \sin \chi_1 + \frac{b}{2} \cos \chi_2 + \frac{c}{2} \sin \chi_2 \right) |1\rangle - \left( \frac{c}{2} - \frac{b}{2} \sin \chi_2 + \frac{c}{2} \cos \chi_2 \right) |2\rangle \right]. \quad (3.17)
\end{aligned}$$

An ancilla readout result of  $|0\rangle$  then induces the map  $\mathbf{T}_0$  given by

$$\begin{aligned}
a \rightarrow a' &= \frac{a + a \cos \chi_1 + b \sin \chi_1}{\sqrt{\mathcal{N}}}, \\
b \rightarrow b' &= \frac{b \cos \chi_1 - a \sin \chi_1 - b \cos \chi_2 - c \sin \chi_2}{\sqrt{\mathcal{N}}}, \\
c \rightarrow c' &= \frac{c + b \sin \chi_2 - c \cos \chi_2}{\sqrt{\mathcal{N}}}, \quad (3.18)
\end{aligned}$$

where

$$\begin{aligned}
\mathcal{N} &\equiv |a + a \cos \chi_1 + b \sin \chi_1|^2 + |b \cos \chi_1 - a \sin \chi_1 - b \cos \chi_2 - c \sin \chi_2|^2 \\
&+ |c + b \sin \chi_2 - c \cos \chi_2|^2. \quad (3.19)
\end{aligned}$$

Using (3.18) we find that in the limit  $\chi_1 = 0$  and  $\chi_2 \rightarrow 0$  the data qutrit prepared in the  $|1\rangle$  state transforms as

$$\mathbf{T}_0 |1\rangle = |2\rangle. \quad (3.20)$$

Our simulations confirm that the dominant mechanism for producing a leakage event is the process (3.20).

Once leaked, the data qutrit remains in the  $|2\rangle$  state (for many cycles) until it either undergoes a nonadiabatic “reverse-leakage” transition or it relaxes back to the computational

subspace. The behaviour of the ancilla during a leakage event depends on the values of  $\xi_1$  and  $\xi_2$  in (3.7). While the data qubit is in the  $|2\rangle$  state, the two-qutrit system is restricted to the subspace spanned by

$$\{ |02\rangle, |12\rangle \}, \quad (3.21)$$

because the  $|22\rangle$  state is decoupled and remains unoccupied. In this subspace, the CZ gate (3.14) acts as

$$\exp \left[ i \begin{pmatrix} \xi_1 & 0 \\ 0 & \xi_2 \end{pmatrix} \right], \quad (3.22)$$

and therefore performs a  $z$  rotation on the ancilla by an angle (3.9). The Hadamards in Fig. 3.1 convert this to an  $x$  rotation [see (3.9)]

$$e^{-i(\theta/2)\sigma^x} \quad (3.23)$$

acting on the initial ancilla state  $|0\rangle$ . Therefore, during a leakage event, while the data qubit is locked in the  $|2\rangle$  state, the state of the ancilla after every cycle is

$$\cos \frac{\theta}{2} |0\rangle + \sin \frac{\theta}{2} |1\rangle, \quad (3.24)$$

and upon measurement the ancilla qubit reads  $|0\rangle$  with probability  $\cos^2(\theta/2)$ .

For example, if

$$\theta \bmod \pi = \frac{\pi}{2}, \quad (3.25)$$

we will observe random ancilla outcomes with equal probabilities for observing  $|0\rangle$  and  $|1\rangle$ . This type of leakage event is simple to detect (and possibly correct). However, if

$$\theta \bmod \pi = 0, \quad (3.26)$$

then the ancilla will always read  $|0\rangle$ , cycle after cycle, giving no indication of the data error and thereby compromising fault-tolerance. We refer to this dangerous phenomena as ancilla *paralysis*.

Figure 3.4 shows the readout values generated from the sequential measurements of the ancilla qubit for different choices of  $\theta$ , including all error process contained in the non-ideal CZ gate (3.14). While we observe random oscillations for larger values of  $\theta$ , no such signature is present for  $\theta = 0$ . In order to quantify the paralysis of the ancilla we define a metric  $W$ , which is the average spacing—number of cycles—between consecutive readouts of  $|1\rangle$ . In the absence of decoherence, we can estimate it [see (3.24)] as

$$W = \csc^2(\theta/2), \quad (3.27)$$

which agrees well with the numerical simulations.

The detectability of a leakage event depends on whether  $W$  is small enough to be observed in the presence of a background value  $W^*$  resulting from decoherence (and possibly other errors). For example, in the simulations of Fig. 3.4, which have  $T_1 = 40 \mu s$  and  $T_2 = 2T_1$ , the average spacing between ancilla  $|1\rangle$  peaks away from the leakage events is 2381 cycles, which is not too far from the crude theoretical estimate

$$W^* \approx \frac{2T_1}{t_{\text{cycle}}} = 1778, \quad (3.28)$$

using  $t_{\text{cycle}} = 45 \text{ ns}$ . The estimate in (3.28) can be derived from the Pauli twirling approximation for qubit decoherence [45], which predicts  $\sigma^x$  and  $\sigma^y$  errors on the ancilla with probability  $p_X = p_Y = t_{\text{cycle}}/4T_1$ , leading to a total bit-flip probability  $p_X + p_Y$  of  $t_{\text{cycle}}/2T_1$ . We can use (3.27) to estimate the critical value of  $\theta$  separating the region of dangerous ancilla

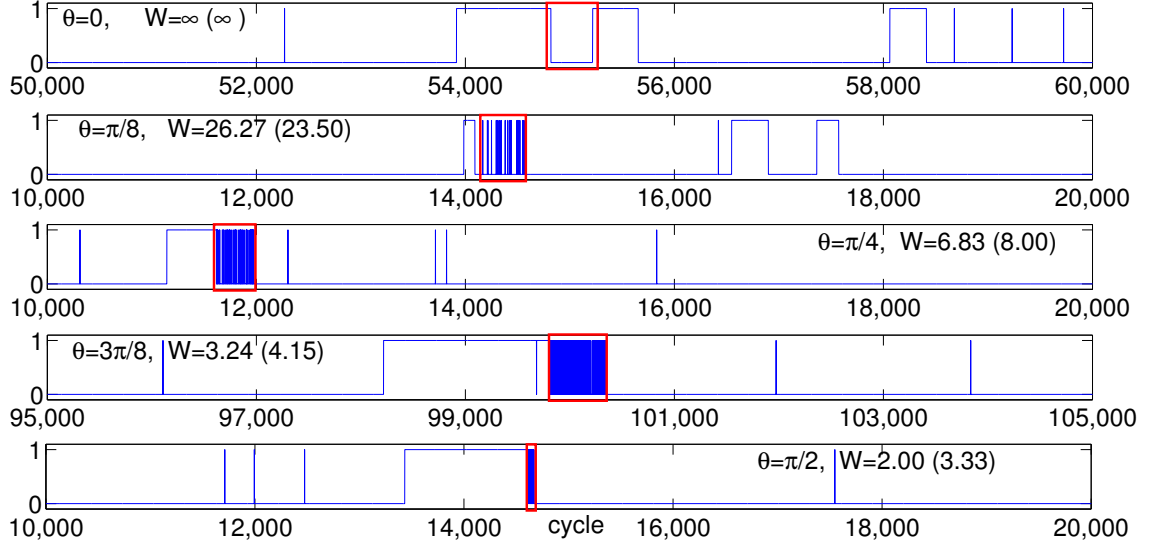


**Figure 3.4:** (Color online) Simulated sequential measurements of the ancilla qubit. The readout values  $|0\rangle$  or  $|1\rangle$  are shown as a function of measurement cycle number. Red rectangles signify leakage events, where the data  $|2\rangle$  state probability is close to unity. Random ancilla oscillations during the leakage events are observed except when  $\theta \approx 0$ . Two values of  $W$  are given for each trace: the theoretical value from (3.27) and a value, shown in parentheses, numerically computed from the simulation. The simulations assume  $T_1 = 40 \mu\text{s}$ ,  $T_2 = 2T_1$ ,  $\chi_i = \zeta_i = 10^{-2}$  for all  $i = 1, \dots, 4$ , and random values of phase angle parameters consistent with the indicated values of  $\theta$ .

paralysis and that of ordinary leakage, namely

$$\theta^* = 2 \csc^{-1} \sqrt{W^*} \approx 2 \csc^{-1} \left( \sqrt{\frac{2T_1}{t_{\text{cycle}}}} \right), \quad (3.29)$$

which is  $\theta^* = 0.04$  in the simulations reported here. CZ gates with  $\theta \bmod \pi < \theta^*$  are susceptible to undetectable leakage events.

### 3.4 Consequences for fault-tolerant quantum computation

We have studied the basic ancilla-assisted measurement circuit in the presence of leakage errors, and identified a rare but potentially dangerous ancilla paralysis effect that could compromise the error-detecting ability of a stabilizer measurement operation. Whether or not undetectable paralysis will occur depends on the difference (3.9) of phase angles produced by the CZ gate. Although fault-tolerance is compromised with either type of leakage event, the ability to detect such an event might allow one to reset the affected qubit to recover from it. We note that the value of  $\theta^*$  is likely to be larger in a multi-qubit Pauli measurement because the cycle time is longer (the background value  $W^*$  is larger). Our results suggest that leakage be addressed either at the hardware level, by periodically removing any  $|2\rangle$  state probability, or by using an architecture such as the 2D topological cluster code, where every qubit gets measured during the error-correction cycle. In addition, it is of course advantageous to adjust  $\theta \bmod \pi$  to a safe value near  $\pi/2$ .

# Chapter 4

## Analysis of Fault-tolerant Architectures <sup>1</sup>

*In all science, error precedes the truth, and it is better it should go first than last.*

– Hugh Walpole

In this chapter, I consider realistic, multi-parameter error models and investigate the performance of the surface code for three possible fault-tolerant superconducting quantum computer architectures. The amplitude and phase damping are mapped to a diagonal Pauli “depolarization” channel via the Pauli Twirling Approximation, and the logical error rate is obtained as a function of the qubit  $T_{1,2}$  and state preparation, gate, and readout errors. A numerical Monte Carlo simulation is performed to obtain the logical error rates, and a leading-order analytic formula is derived to estimate their behavior below threshold. Although our approach is valid for large qubit arrays, we especially focus on first-generation implementations with code distances (for surface code ‘distance’ is equivalent to the max-

---

<sup>1</sup>J. Ghosh, A. G. Fowler, and M. R. Geller, *Physical Review A* **86**, 062318 (2012) [Copyrighted material reprinted in this chapter as per transfer of copyright agreement with the publisher].

imum number of data qubits along a horizontal line)  $d = 3$  and  $d = 5$ , and show that an experimental demonstration of a small- $d$  topological quantum memory should be possible with existing superconducting devices; the  $d = 5$  case already exhibits a pronounced quantum memory enhancement with current transmon  $T_1$  values. Our results suggest that scalable fault-tolerant quantum computation should be possible with existing superconducting devices.

We analyze these different architectures by fixing the intrinsic errors and gate times to estimated realistic values and calculating the logical error rate as a function of the qubit coherence time  $T_1$ . For tunable transmon qubits, the  $T_2$  time is assumed to be equal to  $T_1$ , while for fixed-frequency transmons we assume that  $T_2 = 2T_1$ . The logical error rate is calculated by mapping amplitude and phase damping to the asymmetric “depolarization” channel (ADC), a single-qubit error channel that is diagonal in the Pauli basis. This is explained in Sec. 4.1. The depolarization channel error model is widely used in the quantum error correction literature, and the symmetric case allows simple comparison (especially of fault-tolerant error-threshold values) between different error-correcting codes. The action of the depolarization channel on stabilizer states can be efficiently simulated with a classical computer, enabling the direct calculation of logical error rates for large distance codes, and it accurately captures pure dephasing (but only approximately describes the decoherence found in real superconducting qubits). In Sec. 4.2 we derive a leading-order analytic expression for the logical error rate that estimates the below-threshold scaling behavior (for small code distances). Section 4.3 gives the approximate performance of the three fault-tolerant architectures discussed above, using both the leading-order analytic formula and classical Monte Carlo simulation. There are many ways to implement a surface code with superconducting qubits, and the design details of any given fault-tolerant architecture will surely be improved and optimized over time; in this sense the architectures considered here mainly serve as examples of our approach and indicate that large-scale quantum computers

should be possible with existing superconducting devices (assuming the simple error models considered here).

## 4.1 Mapping decoherence to a diagonal Pauli channel

In this section we discuss the use of Pauli twirling [71–75] to approximately model qubit decoherence by an asymmetric depolarization channel, which—by the Gottesman-Knill theorem—makes efficient classical Monte Carlo simulation possible.

### 4.1.1 Amplitude and phase damping

Quantum systems coupled to an environment undergo spontaneous dissipation of energy, which is usually modeled by the amplitude damping (AD) channel. For a single qubit this has the form

$$\rho \rightarrow \mathcal{E}_{\text{AD}}(\rho) = E_1^{\text{AD}} \rho E_1^{\text{AD}\dagger} + E_2^{\text{AD}} \rho E_2^{\text{AD}\dagger}, \quad (4.1)$$

where

$$E_1^{\text{AD}} = \begin{pmatrix} 1 & 0 \\ 0 & \sqrt{1-p_{\text{AD}}} \end{pmatrix} \text{ and } E_2^{\text{AD}} = \begin{pmatrix} 0 & \sqrt{p_{\text{AD}}} \\ 0 & 0 \end{pmatrix}. \quad (4.2)$$

The  $E_m^{\text{AD}}$  are Kraus matrices for the amplitude damping channel, and  $p_{\text{AD}}$  can be interpreted as the probability of a single photon emission from the qubit.

Phase damping (PD) or pure dephasing is a decoherence process generated by random phase kicks on a single qubit. Assuming the phase kick angle is a Gaussian-distributed random variable, the Kraus matrices for this process are

$$E_1^{\text{PD}} = \begin{pmatrix} 1 & 0 \\ 0 & \sqrt{1-p_{\text{PD}}} \end{pmatrix} \text{ and } E_2^{\text{PD}} = \begin{pmatrix} 0 & 0 \\ 0 & \sqrt{p_{\text{PD}}} \end{pmatrix}. \quad (4.3)$$

The combined channel of amplitude and phase damping can also be described by a set of three Kraus matrices,

$$\begin{aligned}
E_1^{\text{D}} &= \begin{pmatrix} 1 & 0 \\ 0 & \sqrt{1-\gamma-\lambda} \end{pmatrix} = \frac{1+\sqrt{1-\gamma-\lambda}}{2}\mathbb{I} + \frac{1-\sqrt{1-\gamma-\lambda}}{2}\sigma^z, \\
E_2^{\text{D}} &= \begin{pmatrix} 0 & \sqrt{\gamma} \\ 0 & 0 \end{pmatrix} = \frac{\sqrt{\gamma}}{2}\sigma^x + \frac{i\sqrt{\gamma}}{2}\sigma^y, \\
E_3^{\text{D}} &= \begin{pmatrix} 0 & 0 \\ 0 & \sqrt{\lambda} \end{pmatrix} = \frac{\sqrt{\lambda}}{2}\mathbb{I} - \frac{\sqrt{\lambda}}{2}\sigma^z,
\end{aligned} \tag{4.4}$$

where,  $\gamma \equiv p_{\text{AD}}$  and  $\lambda \equiv (1-p_{\text{AD}})p_{\text{PD}}$ . Next we represent the parameters  $p_{\text{AD}}$  and  $p_{\text{PD}}$  in terms of the single-qubit relaxation time  $T_1$  and dephasing time  $T_2$ ,

$$1 - p_{\text{AD}} = e^{-t/T_1}, \tag{4.5}$$

$$\sqrt{(1-p_{\text{AD}})(1-p_{\text{PD}})} = e^{-t/T_2}. \tag{4.6}$$

The combination of amplitude and phase damping on a single qubit transforms the density matrix as,

$$\rho \rightarrow \mathcal{E}_{\text{D}}(\rho) = \begin{pmatrix} 1 - \rho_{11}e^{-t/T_1} & \rho_{01}e^{-t/T_2} \\ \rho_{01}^*e^{-t/T_2} & \rho_{11}e^{-t/T_1} \end{pmatrix}. \tag{4.7}$$

### 4.1.2 Asymmetric depolarization channel

Classical simulation of Eq. (4.7) is inefficient for a multi-qubit system. For example, the textbook architecture requires 25 physical qubits for  $d=3$  and 81 physical qubits for  $d=5$ . The dimension of the Hilbert space is more than 33 million for  $d=3$  and more than  $10^{24}$  for  $d=5$ . This motivates one to construct a simplified error model which is tractable via some efficient classical simulation.

The Asymmetric Depolarization Channel (ADC) is such a model, where a decoherent qubit is assumed to suffer from discrete Pauli  $X$  (bit-flip) errors,  $Z$  (phase flip) errors, or  $Y$  (both):

$$\mathcal{E}_{\text{ADC}}(\rho) = (1 - p_{\Sigma})\rho + p_X X\rho X + p_Y Y\rho Y + p_Z Z\rho Z, \quad (4.8)$$

where  $p_{\Sigma} \equiv p_X + p_Y + p_Z$ . A special case of (4.8) is the symmetric depolarization channel, where  $p_X = p_Y = p_Z$ . The ADC is not sufficient to exactly capture the combined effects of amplitude and phase damping, as no choice of  $p_X$ ,  $p_Y$ , and  $p_Z$  lead to  $\mathcal{E}_{\text{ADC}}(\rho) = \mathcal{E}_{\text{D}}(\rho)$ . However, the advantage of the ADC is that it can be efficiently simulated with a classical computer. Therefore we construct an ADC that approximates (4.7).

### 4.1.3 Pauli twirling approximation

We approximate the combined amplitude damping and dephasing with an ADC via *twirling* [71–75]. Twirling is used in quantum information to study the average effect of arbitrarily general noise models via their mapping to more symmetric ones. Alternative approximate approaches have also been recently proposed [76, 77].

Using the Kraus matrices (4.4), we can rewrite (4.7) in terms of Pauli matrices as [74],

$$\begin{aligned} \mathcal{E}_{\text{D}}(\rho) &= \frac{2 - \gamma + 2\sqrt{1 - \gamma - \lambda}}{4} \mathbb{I}\rho\mathbb{I} + \frac{\gamma}{4} X\rho X + \frac{\gamma}{4} Y\rho Y + \frac{2 - \gamma - 2\sqrt{1 - \gamma - \lambda}}{4} Z\rho Z \\ &+ \frac{\gamma}{4} \mathbb{I}\rho Z + \frac{\gamma}{4} Z\rho\mathbb{I} + \frac{\gamma}{4i} X\rho Y - \frac{\gamma}{4i} Y\rho X. \end{aligned} \quad (4.9)$$

Twirling over the Pauli group removes the off-diagonal terms [72] from (4.9), leading to the ADC (4.8) with error probabilities [74]

$$p_X = p_Y = \frac{1 - e^{-t/T_1}}{4} \quad \text{and} \quad p_Z = \frac{1 - e^{-t/T_2}}{2} - \frac{1 - e^{-t/T_1}}{4}. \quad (4.10)$$

If  $T_2 = T_1$ , the ADC reduces to the symmetric depolarization channel.

We refer to the approximate reduction of any quantum channel to the ADC in this manner as the *Pauli twirling approximation* (PTA). The PTA corresponds to expanding the Kraus matrices in terms of Pauli matrices (and the identity), performing the Kraus summation, and keeping only terms that are diagonal in the Pauli basis. Equivalently, only the diagonal elements of the  $\chi$  matrix in the Pauli basis are retained. Because of its simplicity and wide applicability, we expect the PTA to be a good starting point for refinements that might (approximately) account for the neglected non-diagonal terms.

## 4.2 Physical and logical errors

In this section, I discuss the assumptions of our error model and the logical error rate in the surface code. I also describe the error correction cycle and review the concept of a distance-dependent error threshold.

### 4.2.1 Error model

While superconducting qubits promise scalability, they suffer from various error mechanisms caused by gate errors and decoherence [10, 42, 62, 78]. In order to model quantum noise for various surface code architectures we assume that the errors are Markovian (noise affects each individual gate operation independently) and uncorrelated (noise affects each individual qubit separately).

With these assumptions we now describe the dominant error mechanisms relevant for our purpose. We classify these mechanisms as follows:

1. *Decoherence.* We consider amplitude damping and dephasing as the dominant sources of decoherence, characterized by the relaxation time  $T_1$  and dephasing time  $T_2$  of the qubits. Decoherence is introduced here via the PTA as described above, which allows us to express the single qubit  $X$ ,  $Y$ , and  $Z$  error probabilities as (4.10), where  $t$  is the

operation time. Similarly, with the assumption of uncorrelated errors, one can quantify the error probabilities for various two qubit Pauli channels as

$$\begin{aligned}
p_{IX} &= p_{IY} = p_{XI} = p_{YI} = p_X(1 - p_X - p_Y - p_Z), \\
p_{XX} &= p_{XY} = p_{YX} = p_{YY} = p_X p_Y, \\
p_{XZ} &= p_{ZX} = p_{YZ} = p_{ZY} = p_X p_Z, \\
p_{IZ} &= p_{ZI} = p_Z(1 - p_X - p_Y - p_Z), \\
p_{ZZ} &= p_Z p_Z.
\end{aligned}
\tag{4.11}$$

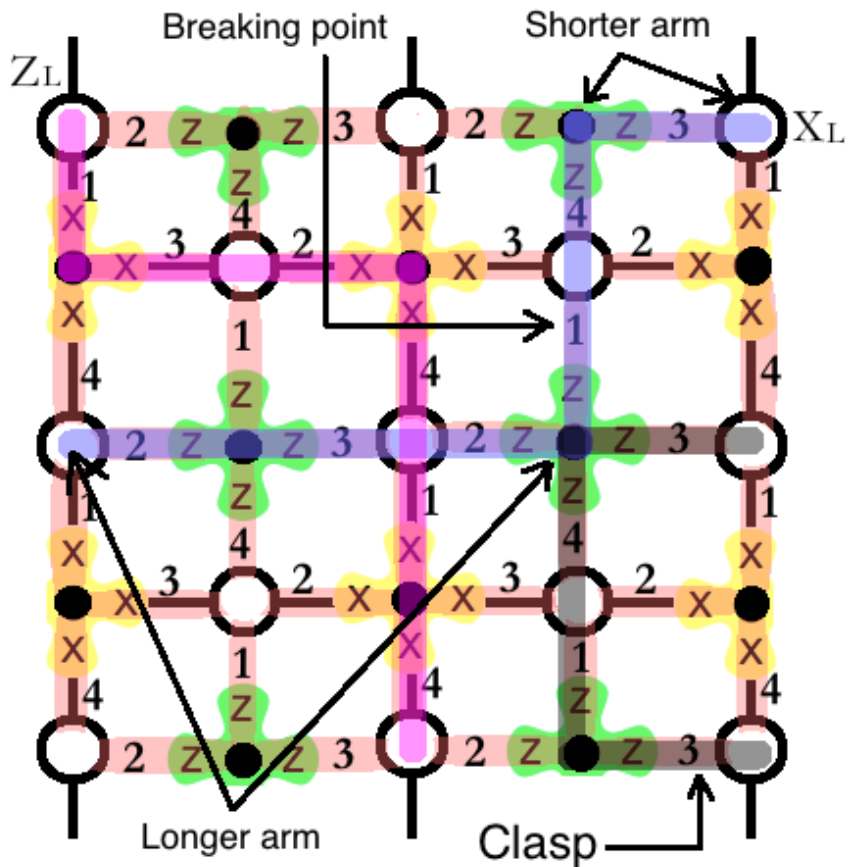
Also notice that our assumptions guarantee that any error ( $X$ ,  $Y$ , or  $Z$ ) in one of the qubits for a two qubit operation can be retrieved when errors on another qubit are traced out; for example  $p_X = p_{XI} + p_{XX} + p_{XY} + p_{XZ}$ .

2. *Unitary rotation error.* Incorrect unitary operations give rise to a type of intrinsic error. By *intrinsic* we mean an error not resulting from noise or decoherence. For single qubit operations, such errors can always be diagonalized in Pauli  $X$ ,  $Y$  or  $Z$  basis. An estimate suggests that with the use of DRAG pulse shapes [10], these errors are ignorable with respect to the intrinsic two-qubit gate errors. Two-qubit gate errors depend on the architecture, and gate protocol.
3. *Leakage.* Leakage is an intrinsic error that populates a quantum state outside of the computational subspace. As far as the single qubit operations are concerned it is possible to suppress leakage below the level of any considerable effect (in comparison to other dominant errors) using quantum control techniques. More quantitatively, it's possible to show that higher-order DRAG pulse is capable to suppress single qubit leakage error below  $10^{-8}$  (theoretically) in 5 ns for superconducting qubits [10].

In the present analysis, however, our primary focus is to investigate the effect of decoherence on logical error rates and therefore, we do not consider leakage or unitary errors

rigorously. Instead, we compute the average intrinsic error of two-qubit gates for the three architectures and distribute it equally to all possible Pauli channels, while decoherence is treated via the PTA.

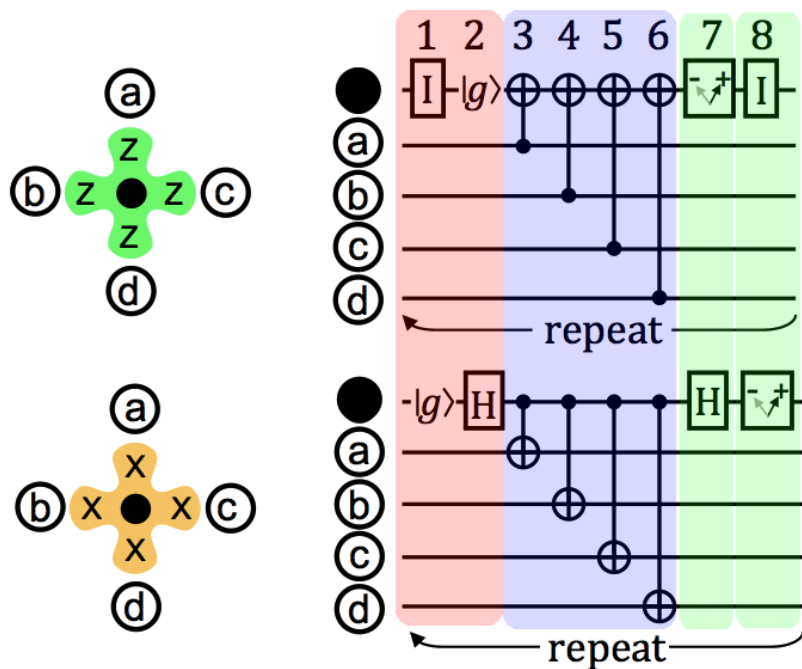
### 4.2.2 Logical error rate in the surface code



**Figure 4.1:** (Color online) A schematic diagram of distance-3 surface code is shown. Two possible error chains,  $X_L$  (purple and horizontal) and  $Z_L$  (magenta and vertical), are displayed and various terminologies used in here are illustrated. Syndrome  $Z$  operators are shown in green (labelled by  $Z$ ) and syndrome  $X$  operators are in yellow (labelled by  $X$ ). An error chain starting and ending at the same boundary is referred to as a ‘clasp’ and is shown in gray color.

In this section we discuss the use of the surface code as a single-logical-qubit quantum memory and describe the error correction cycle. A distance 3 quantum memory is shown

in Fig. 4.1. The open circles are data qubits and filled circles are ancillary qubits used for syndrome measurements. A bit-flip on any data qubit results in an eigenvalue change of adjacent  $Z$  stabilizers and a phase-flip does the same on neighboring  $X$  stabilizers. Therefore, Pauli  $X$ (bit-flip),  $Y$ (bit and phase-flip) and  $Z$  (phase-flip) errors are detectable (and therefore correctable) by sequential measurements of the stabilizer group generators, unless a misidentification in error-detection leads to the formation of a chain starting from one boundary and ending at another. Such error chains commute with all stabilizers but cannot be written as a product of them and therefore remain undetected. The larger the array (or higher the code distance) the lower the probability of formation of these error chains.



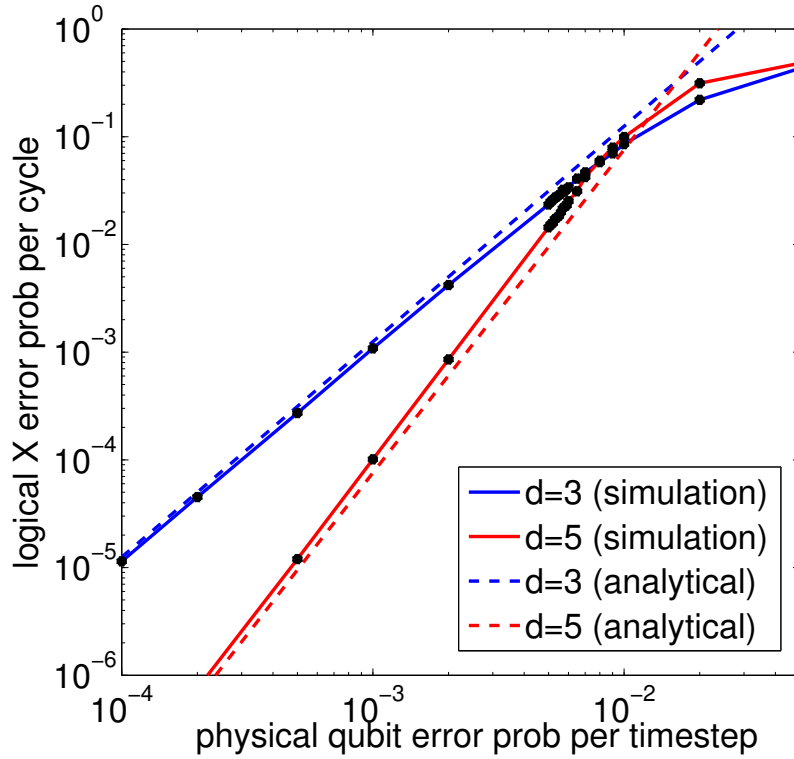
**Figure 4.2:** (Color online) A schematic diagram of a surface code error correction cycle is shown. The red region (dark gray leftmost region) contains state preparation, the blue region (medium gray middle part) contains four consecutive CNOT operations and the green region (light gray) highlights the measurements of syndrome  $Z$  and  $X$  qubits.

Fig. 4.2 shows the steps that a single surface code error correction cycle is comprised of. The first step is the initial state preparation for the syndrome qubits (state  $|0\rangle$  for syndrome  $Z$  and  $|+\rangle$  for syndrome  $X$ ). While there exists multiple approaches for a qubit

state preparation, we here assume that this is done via an ideal projective measurement and a subsequent local rotation ( $\sigma^x$  or Hadamard), if necessary. The state preparation is followed by four CNOT operations with four adjacent data qubits. The order of these CNOT operations is important and in fact from the reference of a syndrome qubit the clockwise and anti-clockwise orders do not work as they lead to unwanted entanglement among the syndrome qubits [57]. We here adopt north-west-east-south protocol without any loss of generality. Notice that while for syndrome  $Z$  measurements data qubits act as control qubits, for syndrome  $X$  measurements data qubits are the targets. These four CNOT operations are followed by measurements for the syndrome  $Z$  case and requires a Hadamard operation before syndrome  $X$  qubits get measured. Such an error correction cycle can be shown to be equivalent to measuring the four-qubit operators  $XXXX$  and  $ZZZZ$ , and are repeated successively.

The data collected via the measurements of syndrome  $Z$  and  $X$  qubits at the end of every cycle are stored in a classical computer. A classical minimum-weight perfect matching algorithm is used to match (up to a homology) syndrome events to identify various error chains [56, 57]. The most likely logical errors occur when a misidentification by the classical software leads to the formation of an error chain starting from one boundary and ending at another of the same type. Such error chains are referred to as homologically nontrivial error chains and are responsible for logical  $X$  or  $Z$  operations on the encoded logical qubit. The logical error rate contributed by these error chains can be determined via classical Monte Carlo simulations.

An analytical leading order estimate of the logical  $X$  or  $Z$  error rates for an asymmetric depolarization channel error model in a surface code is also derived in Appendix A, and its performance is compared against the numerical Monte Carlo simulation (as obtained in Ref. [57]) in Fig. 4.3 . As observed in Refs. [79, 80], there exists an additional mechanism for logical errors originating from error propagation via CNOT operations—the *diagonal* error



**Figure 4.3:** (Color online) Plot of analytic estimate of logical  $X$  error probability per cycle vs. single physical qubit error probability per timestep. Solid lines denote numerical estimates via Monte-Carlo simulation while dashed lines are obtained from our analytical formula given by Eq. (A.6).

chains. We neglect such diagonal error chains in the derivation of our analytic formula and therefore it underpredicts the logical error rates. However, a close correspondence between our analytic estimate and numerical simulation is observed for small distance and below threshold, as shown in Fig. 4.3, since the contributions from the diagonal error chains are negligible in that regime. Thus the approximate analytic formula is sufficient for the regimes of interest in this work. The convergence of the curves indicate that below the cross-over point, surface code error correction helps as we go from  $d = 3$  to  $d = 5$  and above it hurts. We define that transition point as the distance-dependent error threshold.

### 4.3 Architecture performance

In this section we perform an analysis of the logical error rate with numerical Monte Carlo simulation (using AUTOTUNE [63]), and also compare the result to our analytical estimate for the three superconducting architectures. We emphasize that while the numerical Monte-carlo simulation captures all possible error mechanisms, our analytical approach neglects the diagonal error chains as described in Ref. [79, 80]; it therefore underpredicts the numerical result. However, the analytic formula enables a simple and immediate extension to alternative candidate architectures, error models, and parameter values. Table 4.1 shows the parameters used to estimate the logical error rate for the three architectures. We assume tunable transmons for the textbook and Helmer architectures and use two-qubit gate designs that use this tunability. CNOT gates are performed via cross-resonance protocol in the DiVincenzo architecture, which uses transmons operating at the flux sweet spot. Tunable transmons have an additional source of dephasing and therefore we assume  $T_2 = T_1$  for the textbook and Helmer architectures. State preparation of syndrome qubits is assumed to be done via projective measurement followed by a conditional local rotation (as shown in Fig. 4.2) and therefore  $t_{\text{QSP}} = t_{\text{meas}} + t_{\text{loc}}$  in Table 4.1.

**Table 4.1:** Parameters assumed for the three fault-tolerant architectures.

quantity	description	architectures		
		textbook	Helmer	DiVincenzo
$T_1$	qubit relaxation time	1-10 $\mu s$	1-10 $\mu s$	1-40 $\mu s$
$T_2$	qubit dephasing time	$T_1$	$T_1$	$2T_1$
$t_{\text{QSP}}$	state preparation time	40 ns	40 ns	40 ns
$t_{\text{loc}}$	local rotation time	5 ns	5 ns	5 ns
$t_{\text{meas}}$	measurement time	35 ns	35 ns	35 ns
$t_{\text{CNOT}}$	CNOT gate time	21 ns	20 ns	20 ns
$t_{\text{cycle}}$	time duration of a single cycle	164 ns	160 ns	400 ns
$p_{\text{intr}}$	leakage probability for CNOT	$10^{-4}$	$10^{-3}$	$10^{-3}$
$p_{\text{meas}}$	measurement error probability	$10^{-2}$	$10^{-2}$	$10^{-2}$
$p_{\text{QSP}}$	state preparation error probability	$10^{-2}$	$10^{-2}$	$10^{-2}$

### 4.3.1 Approximate logical error rate

Here we construct an approximate analytic formula to estimate the logical error rates below threshold. We use the assumptions of our error model and add the individual error probabilities on data and syndrome qubits for each step to obtain the bit-flip and phase-flip error probabilities *per cycle* as

$$\begin{aligned}
p_{\text{bf}} &= p_X(t_{\text{cycle}}) + p_Y(t_{\text{cycle}}) + 4\frac{8p_{\text{intr}}}{15}, \\
q_{\text{bf}} &= p_{\text{QSP}} + p_X(t_{\text{middle}}) + p_Y(t_{\text{middle}}) + p_{\text{meas}} + 4\frac{8p_{\text{intr}}}{15}, \\
p_{\text{pf}} &= p_Z(t_{\text{cycle}}) + p_Y(t_{\text{cycle}}) + 4\frac{8p_{\text{intr}}}{15}, \\
q_{\text{pf}} &= p_{\text{QSP}} + p_Z(2t_{\text{loc}} + t_{\text{middle}}) + p_Y(2t_{\text{loc}} + t_{\text{middle}}) + p_{\text{meas}} + 4\frac{8p_{\text{intr}}}{15},
\end{aligned} \tag{4.12}$$

where  $t_{\text{middle}} \equiv t_{\text{cycle}} - (t_{\text{QSP}} + t_{\text{loc}} + t_{\text{meas}})$ ,  $p_{\text{bf}}$  and  $q_{\text{bf}}$  ( $p_{\text{pf}}$  and  $q_{\text{pf}}$ ) are the bit-flip (phase-flip) error rates per cycle in the data qubits and syndrome qubits, respectively. The functions  $p(t)$  in (4.12) refer to the expressions (4.10) evaluated with operation time  $t$ . Furthermore,  $t_{\text{QSP}}$  is the time required to complete the initial state preparation for syndrome qubits, and  $p_{\text{QSP}}$  is the error probability that a wrong state is prepared.  $p_{\text{intr}}$  is the intrinsic error of a CNOT gate averaged over the Hilbert space of all input states, and  $p_{\text{meas}}$  is the error probability that a wrong eigenvalue is reported in the readout process. Note that the intrinsic gate error (described by  $p_{\text{intr}}$ ) is assumed to be equally distributed over all 15 two-qubit Pauli errors and therefore the probability of a bit flip (occurs with  $X$  or  $Y$  errors) or phase flip (occurs with  $Z$  or  $Y$  errors) of any qubit during CNOT due to the intrinsic error is  $8p_{\text{intr}}/15$ . When we add each probability we are ignoring all higher-order contributions and also the coherence of these error mechanisms (although our numerical simulation takes the higher-order effects into account). We use these bit and phase flip probabilities in Eq. (A.6) and Eq. (A.7) of

Appendix A to obtain analytical estimates of logical  $X$  and  $Z$  error rates.

### 4.3.2 Textbook architecture

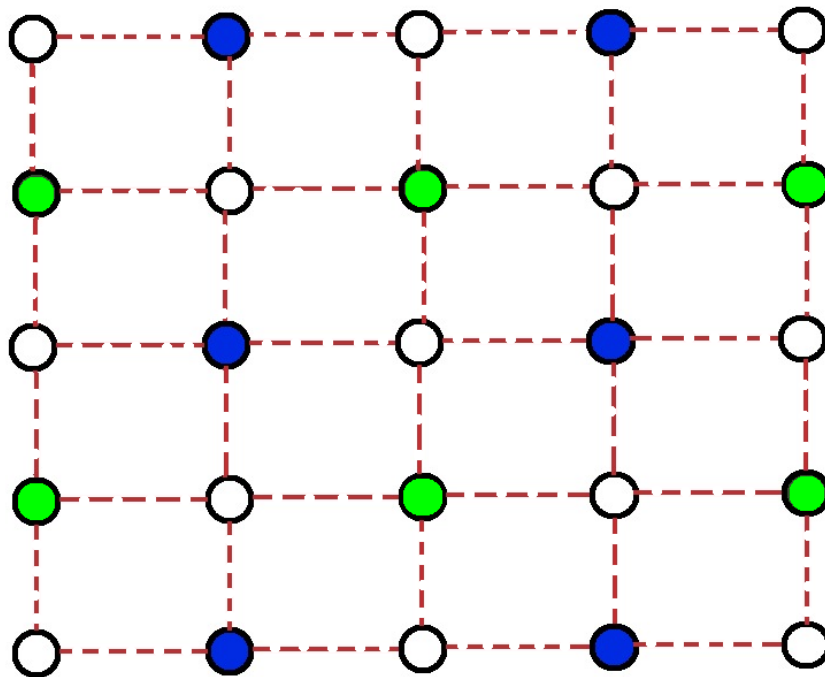


**Figure 4.4:** (Color online) Layout of the distance-3 surface code considered here. Open circles denote data qubits, and light green (dark blue) filled circles denote  $X$ -type ( $Z$ -type) syndrome qubits. The dashed lines denote tunable qubit-qubit coupling. We refer to this hardware design as the textbook architecture.

The textbook architecture consists of a two-dimensional square lattice (as shown in Fig. 4.4) of superconducting qubits—tunable transmons—with nearest-neighbor tunable couplings having infinite on-off ratio. The CNOT operations in this architecture are performed using the protocol discussed in Ref. [62]. We assume that the idle data qubit frequencies are 6 GHz and syndrome qubit frequencies are 8 GHz. The optimal parameters for a CNOT operation, shown in Table B.1, are determined in Appendix B by modeling amplitude and phase damping. As mentioned earlier,  $T_1 = T_2$  is assumed for tunable transmons, as they have an additional source of dephasing that degrades their  $T_2$ .

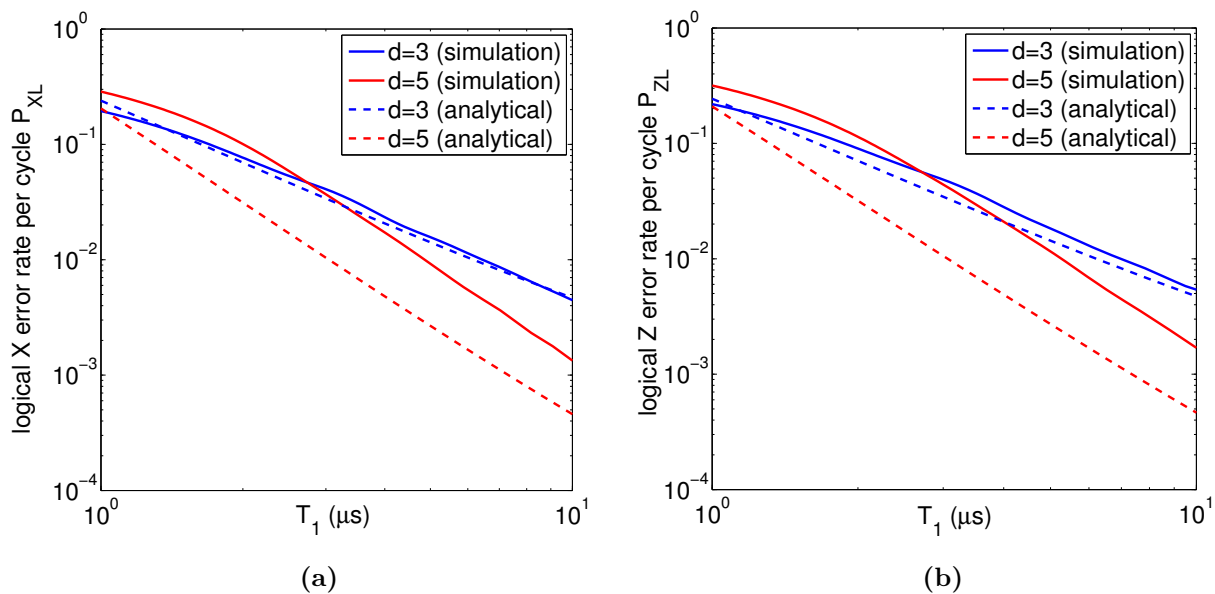


**Figure 4.5:** (Color online) Logical  $X$  and  $Z$  error rate per cycle is shown as a function of coherence time  $T_1$  for the textbook architecture. Plots for  $d = 3$  are shown in blue and those for  $d = 5$  are shown in red.

We use Eq. (4.12) along with Eq. (A.6) and Eq. (A.7) to compute the logical  $X$  and  $Z$  error rates ( $P_{XL}$  and  $P_{ZL}$ ) for the textbook architecture. For the numerical Monte Carlo simulation, we use AUTOTUNE [63] to simulate the circuit shown in Fig. 4.2 for every syndrome qubit.

In Fig. 4.5 we show the graphs (both analytical and numerical) of the logical  $X$  and  $Z$  error probabilities per cycle with  $d = 3$  and  $d = 5$  codes, versus the relaxation time  $T_1$ . Note that for  $d = 3$  our analytic formula closely reproduces the numerical simulation, while for  $d = 5$  it underpredicts as we expect. From the numerical plots we observe that the threshold is at  $\approx 2.6 \mu s$ , where all other parameters are kept fixed as listed in Table 4.1. This result signifies that if we construct this architecture with qubits having  $T_1$  (or  $T_2$ ) more than  $\approx 2.6 \mu s$ , then surface code error correction helps as we increase the distance from  $d = 3$  to  $d = 5$ ; otherwise it hurts.

### 4.3.3 Helmer architecture

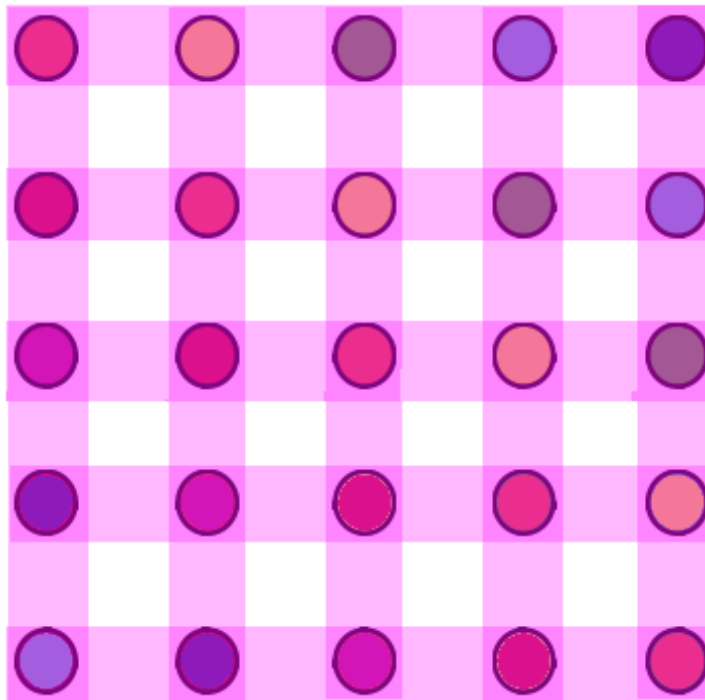


**Figure 4.6:** (Color online) Schematic diagram of the distance-3 Helmer architecture. The circles represent superconducting qubits, with “idle” frequencies indicated by their colors. The horizontal and vertical magenta (gray) rectangles are resonators. All horizontal (vertical) resonators have the same frequency.

In this section we discuss the architecture proposed by Helmer *et al.* [81], where superconducting qubits are arranged in a two-dimensional square lattice and each qubit is coupled to one horizontal and one vertical cavity as shown in Fig. 4.6. The rectangular blocks (horizontal and vertical) are cavities, circles represent qubits and the colors denote their idle (between gate) frequencies. As pointed out in Ref. [81], the minimum frequency range required to allocate the frequencies of all qubits in this architecture is proportional to square root of the number of qubits. While this architecture is not scalable, it is suitable for implementing the distance 3 and 5 surface code, which is a main focus here.

The CNOT gates are performed between a pair of adjacent qubits by tuning them into mutual resonance and waiting for a while somewhere near cavity frequency and thereby

utilizing the effective flip-flop interaction between qubits. The waiting time for this gate is inversely proportional to the magnitude of the effective flip-flop interaction strength and for parameters used in Ref. [81] we estimate  $t_{\text{CNOT}} \approx 20$  ns for this protocol. The dominant source of intrinsic errors for such a CNOT emerges from the higher-order Landau-Zener transitions during tuning and detuning and are estimated to be in the order of  $10^{-3}$  [81]. As specified earlier, the parallel CNOT operations involving the same resonator also cost fidelity due to the higher-order couplings in this architecture. However, in the low distance limit we assume that the total intrinsic error is bound by the fixed (distance-independent) value mentioned above. These parameters are shown in Table 4.1 and used to estimate the logical error probability per cycle for this architecture.

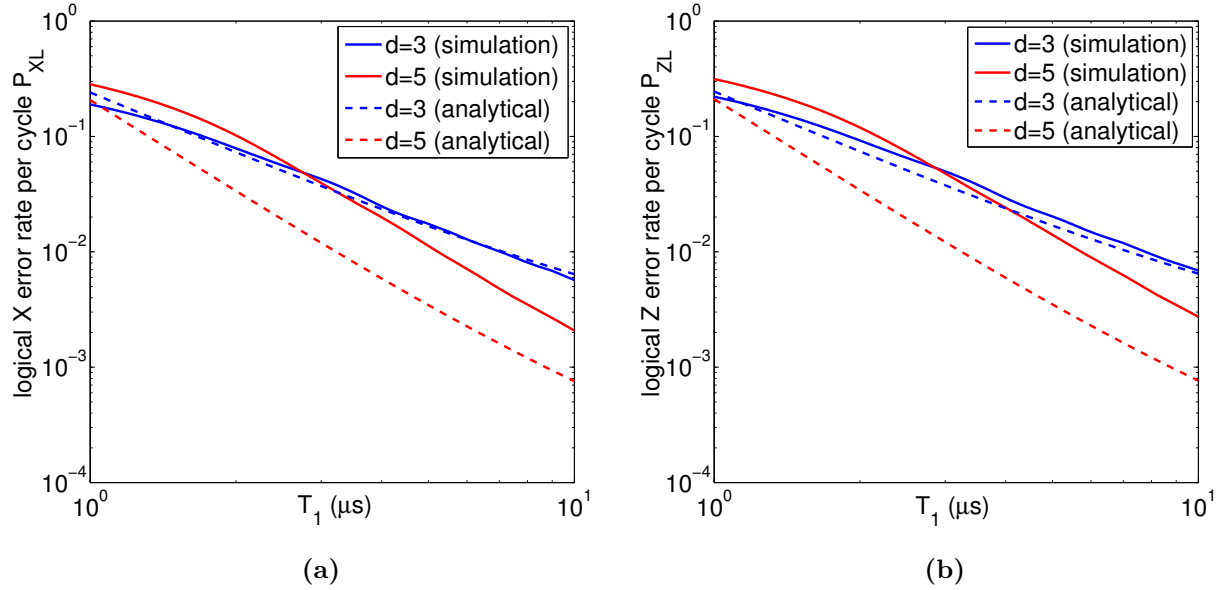


**Figure 4.7:** (Color online) Logical  $X$  and  $Z$  error rate per cycle is shown as a function of coherence time  $T_1$  for the Helmer architecture. Plots for  $d = 3$  are shown in blue and those for  $d = 5$  are shown in red.

The bit-flip and phase-flip error probabilities per cycle for data and syndrome qubits in this architecture are given by (4.12) with  $t_{\text{cycle}} = 160$  ns and  $t_{\text{middle}} = (4 \times 20)$  ns = 80 ns. With a similar analysis we obtain Fig. 4.7, which shows the plots of logical  $X$  and  $Z$  error

probabilities per cycle for  $d = 3$  and 5 error correction with respect to  $T_1$ , and we observe that the threshold is at  $\approx 2.8 \mu s$ .

### 4.3.4 DiVincenzo architecture

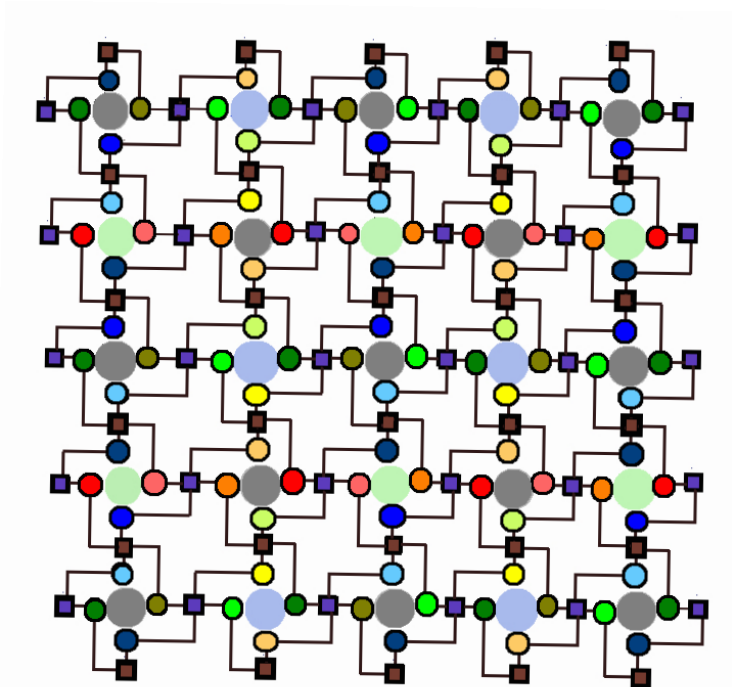


**Figure 4.8:** (Color online) Schematic diagram of the architecture discussed by DiVincenzo [1] for code distance  $d = 3$ . The filled circles with boundaries represent qubits, squares with boundaries represent resonators, and colors of both denote their fixed frequencies. The unbounded circles are for the eye and indicate whether a given block is for data (dark gray),  $X$ -type syndrome (light green), or  $Z$ -type syndrome (blue). A possible frequency allocation for all the components is shown.

Here we analyze the architecture (shown in Fig. 4.8) proposed by DiVincenzo [1], in which each qubit is dispersively coupled to two resonators, while each resonator couples four such qubits. In this architecture every data or syndrome qubit consists of four physical qubits where one of them is primary and the remaining three act as ancillary qubits. The CNOT operations in this architecture are performed via the virtual cross resonance protocol where qubits always remain dispersively coupled to the resonators while microwaves drive

**Table 4.2:** Time duration for each step in the error-correction cycle for DiVincenzo architecture.

operation	time duration
state preparation	40 ns
first CNOT (north)	100 ns
second CNOT (west)	60 ns
third CNOT (east)	60 ns
fourth CNOT (south)	100 ns
local rotation plus readout	40 ns

the population transition between two qubits [27, 29, 31]. Notice that this architecture is fully scalable and the frequency allocation does not depend on the number of qubits.

We first estimate the time required to complete a single surface code cycle in this architecture. As mentioned earlier, for each block one out of four qubits acts as a principal qubit and without loss of generality we assume the eastern qubit to be the principal one for every block. Table 4.2 shows the time required for each individual step in this architecture. The state preparation and read out takes 40 and 35 ns, respectively, as for previous architectures. The first CNOT is performed between a syndrome block and its north data qubit block and this is performed by doing a CNOT between the eastern qubit of the syndrome block and the western qubit of the data block. This CNOT must be accompanied by pre- and post-SWAP operations in the data block where the quantum state of the eastern qubit is transferred to the western one. As discussed, the CNOT operations are performed via the cross-resonance protocol and we assume the gate time for such a CNOT to be  $\approx 20$  ns [27]. SWAP operations between two qubits coupled via resonator is also assumed to be performed in 20 ns. The intrinsic error  $p_{\text{intr}}$  for such CNOT gates is estimated to be in the order of  $10^{-3}$  [31]. These results give us the time durations required for each step in the error correction cycle, shown in Table 4.2. These estimate the duration of a single cycle in this architecture to be 400 ns long.

Following the same argument as in the textbook architecture and using (4.12) for the bit-flip and phase-flip error probabilities with  $t_{\text{cycle}} = 400$  ns and  $t_{\text{middle}} = (100 + 60 + 60 + 100)$  ns = 320 ns, we compute logical  $X$  and  $Z$  error rates. Fig. 4.9 shows the total logical  $X$  and  $Z$  error probabilities per cycle for  $d = 3$  and 5. Note that the condition,  $T_2 = 2T_1$ , leads to  $p_X + p_Y \approx 2(p_Z + p_Y)$  (assuming  $T_{1,2} \gg t_{\text{cycle}}$ ), which means that the bit-flip error rate is almost twice as large as the phase-flip error rate. Since, the logical  $X$  error rate mostly depends on bit-flip probability and logical  $Z$  on phase-flip, we expect  $P_X > P_Z$  for this case. This asymmetry between logical  $X$  and  $Z$  error rates imply a larger error threshold for logical  $X$  error in comparison to logical  $Z$ . We observe from our numerical simulation that logical  $Z$  errors can be suppressed if  $T_1 > 5 \mu\text{s}$ , while in order to suppress logical  $X$  errors we need  $T_1 > 10 \mu\text{s}$ , which is consistent with the above argument.

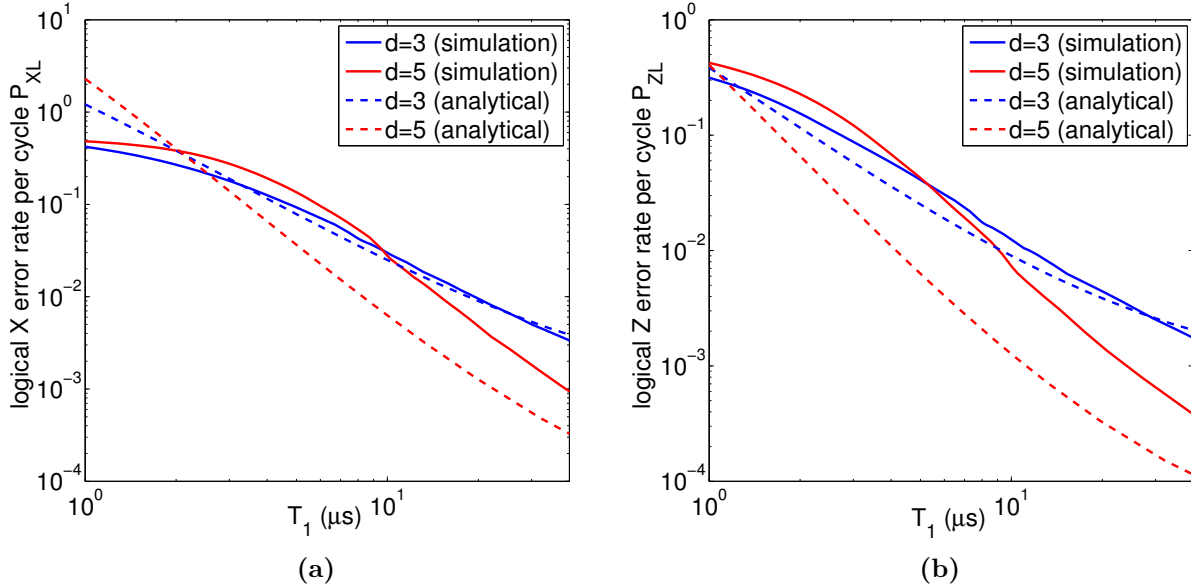


**Figure 4.9:** (Color online) Logical  $X$  and  $Z$  error rate per cycle is shown as a function of coherence time  $T_1$  for the DiVincenzo architecture. Plots for  $d = 3$  are shown in blue and those for  $d = 5$  are shown in red.

### 4.3.5 Other possible architectures

We also discuss some other possible architectures based on fixed coupling elements, as shown in Fig. 4.10. As per our convention, the squares denote resonators, circles denote qubits, and solid lines denote fixed couplings. For gate protocols (CNOT or SWAP) that require tuning and detuning qubits in and out of resonance, the greatest challenge is the frequency allocation such that first-order Landau-Zener transitions can be avoided. We observe that with DC control-based gate protocols [16,62], none of these architectures can avoid first order Landau-Zener transitions. This fact is an inherent property of the topology of these architectures. However, we note that with microwave-control-based gate protocols (for example, cross-resonance), these unwanted transitions can be avoided.

The crucial role of the Landau-Zener transition on the error mechanisms for these architectures motivates us to estimate this error: For any two level system Landau-Zener formula predicts the diabatic transition probability as

$$P_{\text{LZ}} = \exp\left(-2\pi \frac{g^2}{\hbar|\dot{\epsilon}(t^*)|}\right), \quad (4.13)$$

where  $g$  is the coupling between the levels,  $\epsilon(t)$  is the time-dependent energy level separation and  $t^*$  is the time when the levels are in resonance. Assuming parameters relevant for superconducting architectures ( $g \approx 45$  MHz and  $\dot{\epsilon}(t^*) \approx 2$  GHz/ns), we obtain a Landau-Zener transition error  $1 - P_{\text{LZ}}$  of about 4%. This error is unacceptably large. We do not attempt here to perform a more quantitative analysis of logical error rate for these architectures. However, we emphasize that while microwave control-based gate protocols may prove to be useful for these cases, such gate operations have not yet been analyzed in the context of these designs.

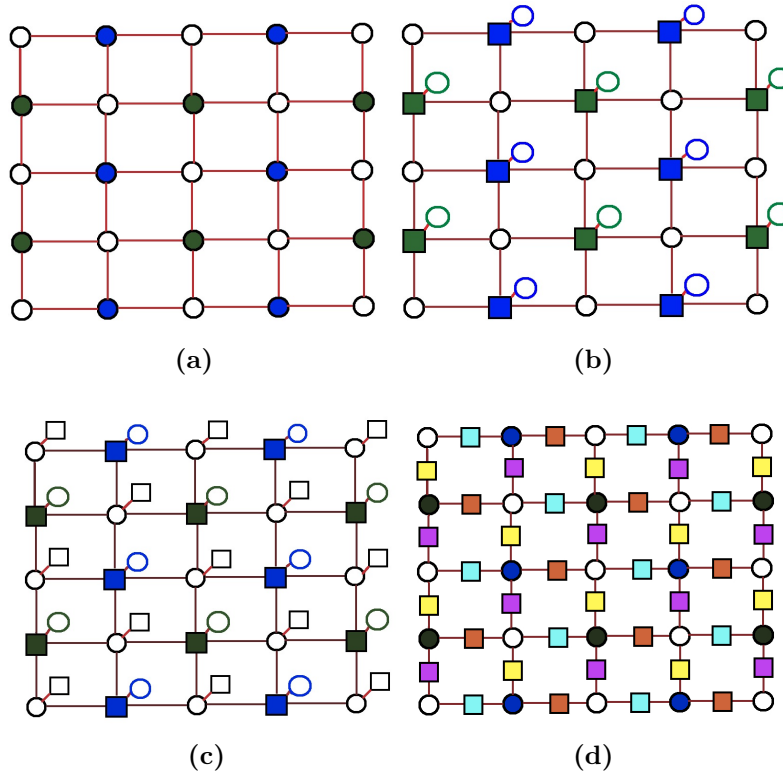


**Figure 4.10:** (Color online) Various possible fixed coupling-based architectures are shown for  $d=3$  surface code. The circles denote qubits, squares denote resonators and various colors (grayscale) denote a possible frequency allocation. (a) An architecture where superconducting qubits are arranged in a two-dimensional square lattice each coupled to its nearest neighbor with fixed couplers. (b) An architecture where superconducting qubits are used for data qubits and resonators for syndrome qubits coupled via fixed couplers. Each resonator is also coupled to another qubit required for read out. (c) Same as architecture (b) except for the fact that each qubit is also coupled to another resonator used as its memory. (d) In this architecture each qubit in a two-dimensional square lattice is coupled to its nearest neighbor via a resonator.

## 4.4 Summary

Table 4.3 summarizes our main results of this analysis. It should be emphasized in this context that the  $T_1$  of the current state-of-the-art Xmon qubit is  $\sim 44 \mu\text{s}$  [14]. So, our results suggest that the coherence times of the recent superconducting qubits are in fact good enough for the fault-tolerant quantum computing within the error model considered

**Table 4.3:** Fault-tolerant  $T_1$  thresholds for the three architectures studied in this work.

architecture	$T_1$ threshold	
	logical $X$ error	logical $Z$ error
textbook	$2.6 \mu s$	$2.6 \mu s$
Helmer	$2.8 \mu s$	$2.8 \mu s$
DiVincenzo	$10 \mu s$	$5 \mu s$

in this work. The operation time requirements for qubit state preparation and readout are, however, yet to be achieved experimentally to the accuracy assumed in this chapter.

# Chapter 5

## Conclusion

*Education never ends, Watson. It is a series of lessons, with the greatest for the last.*

– Sir Arthur Conan Doyle

The main focus of this thesis is the design of a high-fidelity two-qubit CZ gate and an analysis of some existing superconducting fault-tolerant architectures of a quantum computer.

We have investigated the problem of CZ gate design for a qubit-resonator model as well as for the superconducting QVN architecture based on a realistic, two-parameter filtered rectangular pulse. We observe that the use of interacting eigenfunctions as computational basis states, and the use of auxiliary  $z$  rotations on the qubits and bus are critical to obtaining this high performance. We also find that our pulse shape correctly captures the relevant pulse degrees-of-freedom for fidelities up to about 99.99%. One can also consider more complex pulse shapes with many control parameters, which can achieve nearly perfect intrinsic fidelity in a time  $t_{\text{gate}}$  (depending on  $g_b$ ) significantly shorter than obtained with pulse shape (2.69). Egger *et al.* [55] have recently investigated this optimal control approach (using the gradient pulse shape engineering method of Khaneja *et al.* [82]), and have obtained about a factor of

two speedup for a qubit-qubit CZ gate similar to that of Sec. 2.4.4. This approach clearly warrants further investigation and experimental implementation. We did not include the effects of decoherence (or flux noise) in this work. However, an order-of-magnitude estimate of the  $T_1$  decay error  $\mathbb{E} \approx t_{\text{gate}}/T_1$  suggests that it should be possible to demonstrate a 99.9% CZ gate with existing transmon qubits, which would be an important step towards the development of fault-tolerant quantum computation.

We have also investigated the fault-tolerance of three superconducting surface code implementations. While the coherence time has been improving over the past few years for superconducting qubits, we discuss here the minimum coherence time required to achieve error correction. The logical error rate for  $d = 3$  and 5 is computed as a function of qubit coherence time and the threshold is found to be dependent on the architecture, error model, and assumed gate protocol. These error thresholds are within reach of current state-of-the-art superconducting circuit designs. The operation time requirements for qubit state preparation and readout are, however, yet to be achieved experimentally to the accuracy assumed in this work. Our analysis can be extended to the future surface code architectures. As mentioned earlier, the effect of decoherence on the logical error rate is a primary focus in this work, and our error models neglect various higher-order and unintended stray couplings between qubits. Exploring the effect of these factors is a possible direction of future research.

# Appendix A

## Derivation of Approximate Logical Error Rate <sup>1</sup>

In this section we derive the logical error per qubit per cycle as a function of the single qubit error rates, to leading order. Our derivation here does not include the “diagonal” error propagation via CNOT gates [79, 80] and therefore underestimates the logical error rates. Logical error rates for  $X$  and  $Z$  errors per cycle ( $P_{XL}$  and  $P_{ZL}$  respectively) are defined as the probability of formation of an  $X$  or  $Z$  error chain in the surface at the end of a single cycle. We consider the logical  $X$  error first, and the expression for the logical  $Z$  error follows from a similar combinatorial argument. Suppose  $p_{bf}$  and  $q_{bf}$  are bit-flip error probabilities (per cycle) in the data and syndrome qubits, respectively. The dominant error mechanism emerges from the fact that  $(d+1)/2$  errors either get misidentified as  $(d-1)/2$  errors (with 100% probability) or as a different arrangement of  $(d+1)/2$  errors (with 50% probability), thereby producing an error chain after attempting error correction. Such a process can happen in three ways.

*Case 1.* The most natural error chain happens when there are  $(d+1)/2$  data-qubit bit-flip

---

<sup>1</sup>J. Ghosh, A. G. Fowler, and M. R. Geller, *Physical Review A* **86**, 062318 (2012) [Copyrighted material reprinted in this chapter as per transfer of copyright agreement with the publisher].

errors in a single row of a distance- $d$  surface. These  $(d + 1)/2$  error locations can be chosen out of  $d$  locations in  $\binom{d}{\frac{d+1}{2}}$  ways, and such an error chain may occur in any one of the  $d$  rows, leading to

$$P_{\text{XL}}^{(1)} = d \binom{d}{\frac{d+1}{2}} p_{\text{bf}}^{\frac{d+1}{2}}. \quad (\text{A.1})$$

Note that the chance of misidentification of these  $(d + 1)/2$  errors is 100% for this case because the classical error detection software is based on minimal-weight perfect matching. This expression was previously derived in Ref. [57].

*Case 2.* In this case  $(d + 1)/2$  errors occur in two consecutive rows, as shown in Fig. 4.1. We refer to such an error chain as a ‘broken’ error chain and call the point where the chain changes its row as the ‘breaking point’ (shown in Fig. 4.1). In order to estimate this case correctly one needs additional care with error-chains starting from one boundary and ending at the same boundary in a different row. We refer to such an error chain as a ‘clasp’ (shown in Fig. 4.1). Notice that clasps are homologically trivial and therefore should not be considered as a source of logical error. In order not to count these clasps, we classify this case into two mutually exclusive and exhaustive (to leading order) subcases: i) when errors occur in horizontal links of a surface code lattice and ii) when there are no errors on horizontal links. Also, observe that chains with errors in more than one horizontal links contribute to a higher-order process and are therefore excluded from our leading order analysis. If we think that the horizontal link with error divides a row into shorter and longer arms (also shown in Fig. 4.1), then for subcase i, the number of ways an error chain is formed ( $\mathcal{W}^1$ ) is constrained by the condition that all sites of the shorter side cannot be filled with errors for any error chain since in that subcase one would be constructing a clasp. Satisfying this condition, for

a given orientation and a specific pair of adjacent rows, we obtain,

$$\mathcal{W}^1 = \underbrace{(d-1) \binom{d}{\frac{d-1}{2}}}_{\text{all possible chains}} - 2 \underbrace{\sum_{r=1}^{\frac{d-1}{2}} \binom{d-r}{\frac{d-1}{2}-r}}_{\text{clasps}} = \frac{d^2-1}{d+3} \binom{d}{\frac{d-1}{2}}. \quad (\text{A.2})$$

For subcase ii all the single physical qubit errors are distributed among vertical links in two adjacent rows. In this subcase, for a given distribution of single qubit errors, in order not to overcount the homotopic error chains one needs to adopt a convention to place the breaking point. Without loss of any generality, we adopt the convention that the breaking point for this subcase is always placed right next to the rightmost error on the lower arm. Such a convention prevents overcounting of homotopic error chains. The remaining condition one needs to satisfy for this subcase is not to place all single qubit errors on the longer arm of the error chain. This condition prevents us from overcounting case 1. Satisfying these conditions, we find the number of ways an error chain is formed ( $\mathcal{W}^2$ ) for subcase ii as,

$$\mathcal{W}^2 = \underbrace{(d-1) \binom{d-1}{\frac{d-1}{2}}}_{\text{all possible chains}} - \underbrace{\sum_{r=2}^{\frac{d+1}{2}} \binom{d-r}{\frac{d-1}{2}}}_{\text{Case-1 chains}} = \frac{d-1}{2} \binom{d}{\frac{d-1}{2}}. \quad (\text{A.3})$$

Combining these results we obtain the logical  $X$  error probability per cycle for case 2 as

$$P_{\text{XL}}^{(2)} = \frac{1}{2} 2(d-1) [\mathcal{W}^1 + \mathcal{W}^2] p_{\text{bf}}^{\frac{d+1}{2}} = (d-1) \frac{(3d+5)(d-1)}{2(d+3)} \binom{d}{\frac{d-1}{2}} p_{\text{bf}}^{\frac{d+1}{2}}. \quad (\text{A.4})$$

In the first term, the factor of 2 comes from the orientation (bottom-left to top-right or top-left to bottom-right) of the error chain, the factor of 1/2 denotes the fact that the classical error detection software misidentifies such an error chain with a 50% probability, and  $d-1$  corresponds to the number of adjacent pair of rows in a distance- $d$  code.

*Case 3.* The third process that contributes to the same order involves error chains weaving

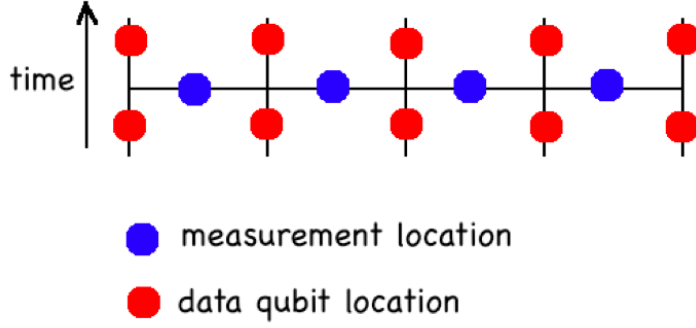


**Figure A.1:** (Color online) Data qubits (red filled circles) of a single row in a distance-5 surface code is shown in two subsequent time slices. The blue filled circles denote measurement locations. An error in any measurement location generates two adjacent timelike syndrome events.

through surfaces in different time slices. In Fig. A.1 we show a single row of a distance-5 surface in two subsequent time slices. Note that the geometry of locations of data qubits and measurement events for this case exactly correspond to the geometry of broken error chains discussed in case 2, except for the fact that the breaking point is along timelike direction instead of spacelike one. In analogy with case 2 we argue that such a situation happens for two subcases: i) when there is one measurement error with a probability  $q_{\text{bf}}$  on one time slice along with  $(d-1)/2$  bit-flip errors on data qubits in two subsequent time slices in a single row, and ii) when there are only  $(d+1)/2$  bit-flip errors on data qubits in two subsequent time slices in a single row. Bit-flip error probability on a syndrome or data qubit in one of the two subsequent time slices is in fact  $p_{\text{bf}}(1-p_{\text{bf}})$  or  $q_{\text{bf}}(1-q_{\text{bf}})$  and keeping only leading order terms we approximate those as  $p_{\text{bf}}$  or  $q_{\text{bf}}$ . Note that the two subcases of case-3 can be mapped exactly with the two subcases of case-2 as far as their combinatorics are concerned and following a similar argument as in case 2 we obtain

$$P_{\text{XL}}^{(3)} = d \left[ \frac{d^2 - 1}{d + 3} \frac{q_{\text{bf}}}{p_{\text{bf}}} + \frac{d - 1}{2} \right] \binom{d}{\frac{d-1}{2}} p_{\text{bf}}^{\frac{d+1}{2}}, \quad (\text{A.5})$$

where the difference in the prefactor comes from the fact that the single row for this case can be chosen in  $d$  ways. Assuming  $q_{\text{bf}}$  is of the same order of magnitude as  $p_{\text{bf}}$ , we observe that case 3 in fact contributes to the same order like previous cases. Also assuming  $p_{\text{bf}} = q_{\text{bf}}$  and replacing the prefactor  $d$  with  $d-1$  in (A.5), we can retrieve the right hand side of (A.4). We claim that—except for these three cases—all other processes contribute higher-order terms as they involve multiple breaking points. Combining all the contributions we obtain

$$P_{\text{XL}} = \left[ d + (d-1) \frac{(3d+5)(d-1)}{2(d+3)} + d \left( \frac{d^2-1}{d+3} \frac{q_{\text{bf}}}{p_{\text{bf}}} + \frac{d-1}{2} \right) \right] \binom{d}{\frac{d-1}{2}} p_{\text{bf}}^{\frac{d+1}{2}}. \quad (\text{A.6})$$

As far as the topology of the logical error chains are concerned, there is no difference between logical  $X$  and  $Z$  errors which enables us to use the same combinatorics to show that the logical  $Z$  error probability,

$$P_{\text{ZL}} = \left[ d + (d-1) \frac{(3d+5)(d-1)}{2(d+3)} + d \left( \frac{d^2-1}{d+3} \frac{q_{\text{pf}}}{p_{\text{pf}}} + \frac{d-1}{2} \right) \right] \binom{d}{\frac{d-1}{2}} p_{\text{pf}}^{\frac{d+1}{2}}, \quad (\text{A.7})$$

where  $p_{\text{pf}}$  and  $q_{\text{pf}}$  are phase-flip error probabilities (per cycle) in data and syndrome qubits respectively.

At this point, we emphasize that our derivation never invokes any particular assumption about internal steps of a surface code cycle and therefore is also valid in a situation where the capability of directly measuring three or four qubit Pauli operators is implicitly assumed. As pointed out in Ref. [79, 80], for a surface code cycle where measurement of multi-qubit operators are replaced by a sequence of CNOT operations, additional error chains having pure diagonal links emerge. While these error chains also contribute to the leading order, the number of such error chains is negligible for low distances. To verify the performance of our analytic expression, we assume a symmetric depolarization channel error model for an 8-step surface code cycle (as described in Ref. [57]) and plot logical  $X$  error rate per cycle as a function of single physical qubit error rate per timestep ( $p_{\text{step}}$ ), which is (approximately)

related to  $p_{\text{bf}}$  via

$$p_{\text{step}} = \frac{3}{2} \left( \frac{p_{\text{bf}}}{8} \right). \quad (\text{A.8})$$

Fig. 4.3 shows a comparison (for logical  $X$  error) of our analytical estimate and a numerical Monte-Carlo simulation as obtained in Ref. [57]; it is evident that for low distances the analytic estimate correctly captures the dominant behavior of these error chains below threshold.

# Appendix B

## Coupled Qubit Model under Decoherence <sup>1</sup>

In this section we compute the fidelity loss during a CZ gate for a coupled qubit model under amplitude and phase damping. Such a model is important for the estimation of total CNOT gate time as well as intrinsic errors for textbook architecture. Since we assume the couplers having infinite on-off ratio for this architecture, each pair of qubits gets decoupled from all other pairs for each intermediate step of error correction cycle and therefore each pair of coupled qubits can be treated separately. Both the qubits are assumed to have three levels and the Hamiltonian is given by,

$$H(t) = \begin{pmatrix} 0 & 0 & 0 \\ 0 & \omega_1(t) & 0 \\ 0 & 0 & 2\omega_1(t) - \eta \end{pmatrix}_{q_1} + \begin{pmatrix} 0 & 0 & 0 \\ 0 & \omega_2 & 0 \\ 0 & 0 & 2\omega_2 - \eta \end{pmatrix}_{q_2} + g \begin{pmatrix} 0 & -i & 0 \\ i & 0 & -i\sqrt{2} \\ 0 & i\sqrt{2} & 0 \end{pmatrix}_{q_1} \otimes \begin{pmatrix} 0 & -i & 0 \\ i & 0 & -i\sqrt{2} \\ 0 & i\sqrt{2} & 0 \end{pmatrix}_{q_2}, \quad (\text{B.1})$$

where the suffix denotes qubit index,  $g$  represents the coupling between the qubits and  $\eta$  is the anharmonicity of the qubit. For a CZ operation we control the frequency of the first

---

<sup>1</sup>J. Ghosh, A. G. Fowler, and M. R. Geller, *Physical Review A* **86**, 062318 (2012) [Copyrighted material reprinted in this chapter as per transfer of copyright agreement with the publisher].

qubit ( $\omega_1(t)$ ) with an error function pulse as described in Ref. [62] while the frequency of the second qubit is kept constant. The Kraus matrices for the amplitude damping channel of any three level quantum system are given by,

$$E_1^{\text{AD}} = \begin{pmatrix} 1 & 0 & 0 \\ 0 & \sqrt{1-\lambda_1} & 0 \\ 0 & 0 & \sqrt{1-\lambda_2} \end{pmatrix}, E_2^{\text{AD}} = \begin{pmatrix} 0 & \sqrt{\lambda_1} & 0 \\ 0 & 0 & 0 \\ 0 & 0 & 0 \end{pmatrix}, E_3^{\text{AD}} = \begin{pmatrix} 0 & 0 & \sqrt{\lambda_2} \\ 0 & 0 & 0 \\ 0 & 0 & 0 \end{pmatrix} \quad (\text{B.2})$$

and Kraus matrices for phase damping are given by,

$$E_1^{\text{PD}} = \begin{pmatrix} 1 & 0 & 0 \\ 0 & \sqrt{1-\lambda_3} & 0 \\ 0 & 0 & \sqrt{1-\lambda_4} \end{pmatrix}, E_2^{\text{PD}} = \begin{pmatrix} 0 & 0 & 0 \\ 0 & \sqrt{\lambda_3} & 0 \\ 0 & 0 & \sqrt{\lambda_4} \end{pmatrix}, \quad (\text{B.3})$$

where  $\lambda_k$  for  $k = 1, 2, 3, 4$  being parameters of our decoherence model. We assume the same amplitude and phase damping probability for  $|1\rangle$  and  $|2\rangle$  states ( $\lambda \equiv \lambda_1 = \lambda_2$  and  $\lambda' \equiv \lambda_3 = \lambda_4$ ) and represent  $\lambda$  and  $\lambda'$  as functions of time duration ( $\Delta t$ ) and  $T_1, T_2$  of the quantum system as,

$$\lambda(\Delta t, T_1) = 1 - e^{-\Delta t/T_1}, \lambda'(\Delta t, T_1, T_2) = 1 - e^{-\Delta t[\frac{2}{T_2} - \frac{1}{T_1}]}. \quad (\text{B.4})$$

**Table B.1:** Optimal parameters and results obtained for CNOT gate in this coupled qubit model. We use these results for the estimation of logical error rate in textbook architecture.

$\omega_1(t=0)$	$\omega_2$	$\eta$	$g$	$t_{\text{CNOT}}$	$p_{\text{intr}}$
8 GHz	6 GHz	300 MHz	55 MHz	21 ns	$1.23 \times 10^{-4}$

The assumption that decoherence affects each qubit independently enables us to construct the full Kraus matrices for the qubit-qubit model by performing all possible tensor products between individual single qubit Kraus matrices. We first simulate the Hamiltonian given by

(B.1) for parameters given in Table. 4.1 without decoherence to obtain an optimal pulse shape that maximizes the average fidelity of the CZ gate for a given coupling and gate time. Next we apply our decoherence model described by Eqs. (B.2) and (B.3) on those optimal pulses. Fig. B.1 shows plots of leakage error from  $|11\rangle$  for such decoherence model (for  $T_1 = 10 \mu s$ ) applied on optimal pulses with respect to various total gate time and for various values of coupling strengths. Fig. B.1 also shows that there exists an optimal point corresponding to total gate time  $\sim 11$  ns at  $g = 55$  MHz for which the leakage from  $|11\rangle$  state is the minimum under decoherence. We use this point for the CZ part of the CNOT operation in textbook architecture and assuming that local rotations can be performed almost exactly in 5 ns, a CNOT requires 21 ns time duration as it involves two Hadamard operations along with a CZ. Table B.1 shows the optimal parameters and results obtained from this analysis.

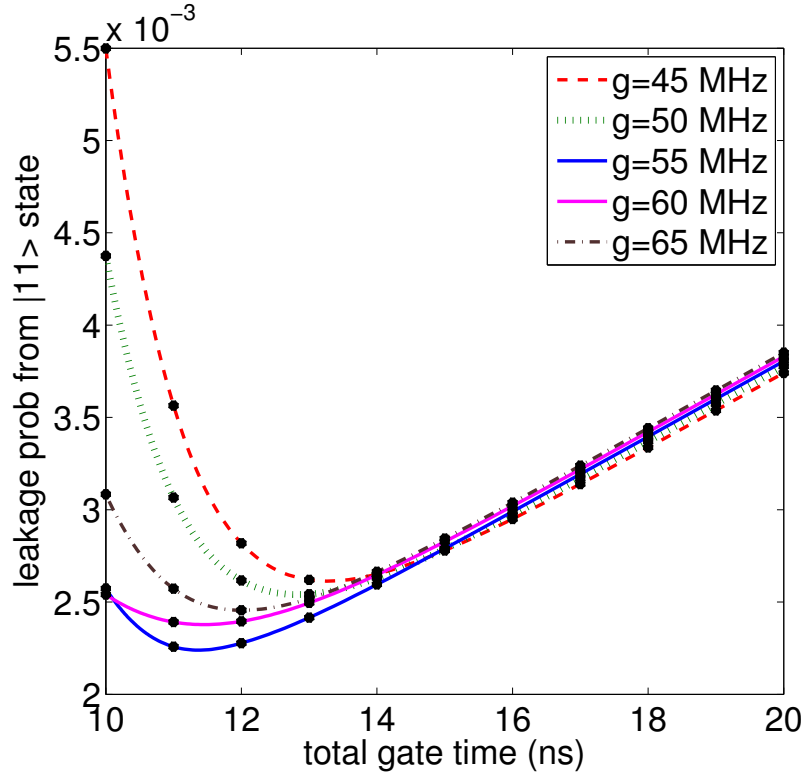


**Figure B.1:** (Color online) Plot of leakage probability from  $|11\rangle$  state under decoherence for various  $g$  during a CZ operation vs total CZ operation time.

# Bibliography

- [1] DiVincenzo, David P, “Fault-tolerant architectures for superconducting qubits,” *Physica Scripta*, volume T137, no. T137, p. 014020, 2009
- [2] Feynman, Richard P., “Simulating physics with computers,” *International Journal of Theoretical Physics*, volume 21, no. 6-7, pp. 467–488, ISSN 0020-7748, 1982
- [3] You, J. Q. and Nori, F., “Superconducting circuits and quantum information,” *Physics Today*, volume 58, no. 11, p. 42, p. 42, November 2005
- [4] Geller, M. R., Pritchett, E. J., Sornborger, A. T., and Wilhelm, F. K., “Quantum Computing with Superconductors I: Architectures,” *Manipulating Quantum Coherence in Solid State Systems edited by M E Flatte and I Tifrea Springer 2007*, volume Springer, 2007, p. 171, 2007
- [5] Martinis, John M., Nam, S., Aumentado, J., and Urbina, C., “Rabi Oscillations in a Large Josephson-Junction Qubit,” *Phys Rev Lett*, volume 89, p. 117901, Aug 2002
- [6] Yu, Yang, Han, Siyuan, Chu, Xi, Chu, Shih-I, and Wang, Zhen, “Coherent Temporal Oscillations of Macroscopic Quantum States in a Josephson Junction,” *Science*, volume 296, no. 5569, pp. 889–892, 2002

- [7] Vion, D., Aassime, A., Cottet, A., Joyez, P., Pothier, H., Urbina, C., Esteve, D., and Devoret, M. H., “Manipulating the Quantum State of an Electrical Circuit,” *Science*, volume 296, no. 5569, pp. 886–889, 2002
- [8] DiVincenzo, David P., “The Physical Implementation of Quantum Computation,” *Fortschritte der Physik*, volume 48, no. 9-11, pp. 771–783, ISSN 1521-3978, 2000
- [9] Nielsen, M. A. and Chuang, I. L., *Quantum Computation and Quantum Information*, Cambridge University Press, 2005
- [10] Motzoi, F., Gambetta, J. M., Rebentrost, P., and Wilhelm, F. K., “Simple Pulses for Elimination of Leakage in Weakly Nonlinear Qubits,” *Phys Rev Lett*, volume 103, no. 11, p. 110501, Sep 2009
- [11] Sete, Eyob A., Galiautdinov, Andrei, Mlinar, Eric, Martinis, John M., and Korotkov, Alexander N., “Catch-Disperse-Release Readout for Superconducting Qubits,” *Phys Rev Lett*, volume 110, p. 210501, May 2013
- [12] Xiang, Ze-Liang, Ashhab, Sahel, You, J. Q., and Nori, Franco, “Hybrid quantum circuits: Superconducting circuits interacting with other quantum systems,” *Rev Mod Phys*, volume 85, pp. 623–653, Apr 2013
- [13] Koch, Jens, Yu, Terri M., Gambetta, Jay, Houck, A. A., Schuster, D. I., Majer, J., Blais, Alexandre, Devoret, M. H., Girvin, S. M., and Schoelkopf, R. J., “Charge-insensitive qubit design derived from the Cooper pair box,” *Phys Rev A*, volume 76, p. 042319, Oct 2007
- [14] Barends, R., Kelly, J., Megrant, A., Sank, D., Jeffrey, E., Chen, Y., Yin, Y., Chiaro, B., Mutus, J., Neill, C., O’Malley, P., Roushan, P., Wenner, J., White, T. C., Cleland, A. N., and Martinis, J. M., “Coherent Josephson qubit suitable for scalable quantum integrated circuits,” *ArXiv e prints*, April 2013

- [15] Megrant, A., Neill, C., Barends, R., Chiaro, B., Chen, Yu, Feigl, L., Kelly, J., Lucero, Erik, Mariantoni, Matteo, O'Malley, P. J. J., Sank, D., Vainsencher, A., Wenner, J., White, T. C., Yin, Y., Zhao, J., m, C. J. Palmstrø, Martinis, John M., and Cleland, A. N., "Planar superconducting resonators with internal quality factors above one million," *Applied Physics Letters*, volume 100, no. 11, p. 113510, 2012
- [16] Strauch, Frederick W., Johnson, Philip R., Dragt, Alex J., Lobb, C. J., Anderson, J. R., and Wellstood, F. C., "Quantum Logic Gates for Coupled Superconducting Phase Qubits," *Phys Rev Lett*, volume 91, p. 167005, 2003
- [17] Johnson, Philip R., Strauch, Frederick W., Dragt, Alex J., Ramos, Roberto C., Lobb, C. J., Anderson, J. R., and Wellstood, F. C., "Spectroscopy of capacitively coupled Josephson-junction qubits," *Phys Rev B*, volume 67, p. 020509, Jan 2003
- [18] Blais, Alexandre, van den Brink, Alexander Maassen, and Zagoskin, Alexandre M., "Tunable Coupling of Superconducting Qubits," *Phys Rev Lett*, volume 90, p. 127901, Mar 2003
- [19] You, J. Q., Nakamura, Y., and Nori, Franco, "Fast two-bit operations in inductively coupled flux qubits," *Phys Rev B*, volume 71, p. 024532, Jan 2005
- [20] Rigetti, Chad, Blais, Alexandre, and Devoret, Michel, "Protocol for Universal Gates in Optimally Biased Superconducting Qubits," *Phys Rev Lett*, volume 94, p. 240502, Jun 2005
- [21] Liu, Yu-xi, Wei, L. F., Tsai, J. S., and Nori, Franco, "Controllable Coupling between Flux Qubits," *Phys Rev Lett*, volume 96, p. 067003, Feb 2006
- [22] Paraoanu, G. S., "Microwave-induced coupling of superconducting qubits," *Phys Rev B*, volume 74, p. 140504, Oct 2006

- [23] Ashhab, S., Matsuo, Shigemasa, Hatakenaka, Noriyuki, and Nori, Franco, “Generalized switchable coupling for superconducting qubits using double resonance,” *Phys Rev B*, volume 74, p. 184504, Nov 2006
- [24] Grajcar, M., Liu, Yu-xi, Nori, Franco, and Zagoskin, A. M., “Switchable resonant coupling of flux qubits,” *Phys Rev B*, volume 74, p. 172505, Nov 2006
- [25] Ashhab, S. and Nori, Franco, “Switchable coupling for superconducting qubits using double resonance in the presence of crosstalk,” *Phys Rev B*, volume 76, p. 132513, Oct 2007
- [26] Liu, Yu-xi, Wei, L. F., Johansson, J. R., Tsai, J. S., and Nori, Franco, “Superconducting qubits can be coupled and addressed as trapped ions,” *Phys Rev B*, volume 76, p. 144518, Oct 2007
- [27] Rigetti, Chad and Devoret, Michel, “Fully microwave-tunable universal gates in superconducting qubits with linear couplings and fixed transition frequencies,” *Phys Rev B*, volume 81, p. 134507, Apr 2010
- [28] de Groot, P. C., Lisenfeld, J., Schouten, R. N., Ashhab, S., Lupascu, A., Harmans, C. J. P. M., and Mooij, J. E., “Selective darkening of degenerate transitions demonstrated with two superconducting quantum bits,” *Nat Phys*, volume 6, no. 10, pp. 763–766, ISSN 1745-2473, October 2010
- [29] Chow, Jerry M., Córcoles, A. D., Gambetta, Jay M., Rigetti, Chad, Johnson, B. R., Smolin, John A., Rozen, J. R., Keefe, George A., Rothwell, Mary B., Ketchen, Mark B., and Steffen, M., “Simple All-Microwave Entangling Gate for Fixed-Frequency Superconducting Qubits,” *Phys Rev Lett*, volume 107, p. 080502, Aug 2011
- [30] de Groot, P C, Ashhab, S, Lupacu, A, DiCarlo, L, Nori, Franco, Harmans, C J P M, and Mooij, J E, “Selective darkening of degenerate transitions for implementing quantum

- controlled-NOT gates,” *New Journal of Physics*, volume 14, no. 7, pp. 073038–, ISSN 1367-2630, 2012
- [31] Chow, Jerry M., Gambetta, Jay M., Córcoles, A. D., Merkel, Seth T., Smolin, John A., Rigetti, Chad, Poletto, S., Keefe, George A., Rothwell, Mary B., Rozen, J. R., Ketchen, Mark B., and Steffen, M., “Universal Quantum Gate Set Approaching Fault-Tolerant Thresholds with Superconducting Qubits,” *Phys Rev Lett*, volume 109, p. 060501, Aug 2012
- [32] Zanardi, Paolo and Lidar, Daniel A., “Purity and state fidelity of quantum channels,” *Phys Rev A*, volume 70, no. 1, p. 012315, Jul 2004
- [33] Pedersen, Line Hjortshøj, Møller, Niels Martin, and Mølmer, Klaus, “Fidelity of quantum operations,” *Physics Letters A*, volume 367, no. 1-2, pp. 47 – 51, ISSN 0375-9601, 2007
- [34] Pedersen, Line Hjortshøj, Møller, Niels Martin, and Mølmer, Klaus, “The distribution of quantum fidelities,” *Physics Letters A*, volume 372, no. 47, pp. 7028 – 7032, ISSN 0375-9601, 2008
- [35] Zhang, J., Vala, J., Sastry, S., and Whaley, K. B., “Geometric theory of nonlocal two-qubit operations,” *Phys Rev A*, volume 67, p. 042313, 2003
- [36] Zhang, J. and Whaley, K. B., “Generation of quantum logic operations from physical Hamiltonians,” *Phys Rev A*, volume 71, p. 052317, 2005
- [37] Geller, Michael R., Pritchett, Emily J., Galiautdinov, Andrei, and Martinis, John M., “Quantum logic with weakly coupled qubits,” *Phys Rev A*, volume 81, no. 1, p. 012320, Jan 2010

- [38] Ghosh, Joydip and Geller, Michael R., “Controlled-not gate with weakly coupled qubits: Dependence of fidelity on the form of interaction,” *Phys Rev A*, volume 81, no. 5, p. 052340, May 2010
- [39] Plantenberg, J. H., de Groot, P. C., Harmans, C. J. P. M, and Mooij, J. E., “Demonstration of controlled-NOT quantum gates on a pair of superconducting quantum bits,” *Nature*, volume 447, p. 836, 2007
- [40] DiCarlo, L., Chow, J. M., Gambetta, J. M., Bishop, Lev S., Johnson, B. R., Schuster, D. I., Majer, J., Blais, A., Frunzio, L., Girvin, S. M., and Schoelkopf, R. J., “Demonstration of two-qubit algorithms with a superconducting quantum processor,” *Nature*, volume 460, no. 7252, pp. 240–244, July 2009
- [41] Mariani, Matteo, Wang, H., Yamamoto, T., Neeley, M., Bialczak, Radoslaw C., Chen, Y., Lenander, M., Lucero, Erik, O’Connell, A. D., Sank, D., Weides, M., Wenner, J., Yin, Y., Zhao, J., Korotkov, A. N., Cleland, A. N., and Martinis, John M., “Implementing the Quantum von Neumann Architecture with Superconducting Circuits,” *Science*, volume 334, no. 6052, pp. 61–65, 2011
- [42] Galiutdinov, Andrei, Korotkov, Alexander N., and Martinis, John M., “Resonator-zero-qubit architecture for superconducting qubits,” *Phys Rev A*, volume 85, p. 042321, Apr 2012
- [43] Viola, Lorenza and Lloyd, Seth, “Dynamical suppression of decoherence in two-state quantum systems,” *Phys Rev A*, volume 58, pp. 2733–2744, Oct 1998
- [44] Yamamoto, T., Neeley, M., Lucero, E., Bialczak, R. C., Kelly, J., Lenander, M., Mariani, Matteo, O’Connell, A. D., Sank, D., Wang, H., Weides, M., Wenner, J., Yin, Y., Cleland, A. N., and Martinis, John M., “Quantum process tomography of

- two-qubit controlled-Z and controlled-NOT gates using superconducting phase qubits,” *Phys Rev B*, volume 82, no. 18, p. 184515, Nov 2010
- [45] Ghosh, Joydip, Fowler, Austin G., and Geller, Michael R., “Surface code with decoherence: An analysis of three superconducting architectures,” *Phys Rev A*, volume 86, p. 062318, 2012
- [46] Gambetta, J. M., Motzoi, F., Merkel, S. T., and Wilhelm, F. K., “Analytic control methods for high-fidelity unitary operations in a weakly nonlinear oscillator,” *Phys Rev A*, volume 83, p. 012308, Jan 2011
- [47] Hofheinz, Max, Wang, H., Ansmann, M., Bialczak, Radoslaw C., Lucero, Erik, Neeley, M., O’Connell, A. D., Sank, D., Wenner, J., Martinis, John M., and Cleland, A. N., “Synthesizing arbitrary quantum states in a superconducting resonator,” *Nature*, volume 459, no. 7246, pp. 546–549, ISSN 0028-0836, May 2009
- [48] Hofheinz, Max, Weig, E. M., Ansmann, M., Bialczak, Radoslaw C., Lucero, Erik, Neeley, M., O’Connell, A. D., Wang, H., Martinis, John M., and Cleland, A. N., “Generation of Fock states in a superconducting quantum circuit,” *Nature*, volume 454, no. 7202, pp. 310–314, ISSN 0028-0836, July 2008
- [49] Martinis, John, “Superconducting phase qubits,” *Quantum Information Processing*, volume 8, pp. 81–103, ISSN 1570-0755, 10.1007/s11128-009-0105-1, 2009
- [50] Houck, A.A., Koch, Jens, Devoret, M.H., Girvin, S.M., and Schoelkopf, R.J., “Life after charge noise: recent results with transmon qubits,” *Quantum Information Processing*, volume 8, no. 2-3, pp. 105–115, ISSN 1570-0755, 2009
- [51] L. Pryadko and A. Korotkov, unpublished.

- [52] Raussendorf, Robert and Harrington, Jim, “Fault-Tolerant Quantum Computation with High Threshold in Two Dimensions,” *Phys Rev Lett*, volume 98, p. 190504, May 2007
- [53] Fowler, Austin G., Stephens, Ashley M., and Groszkowski, Peter, “High-threshold universal quantum computation on the surface code,” *Phys Rev A*, volume 80, p. 052312, Nov 2009
- [54] A. Galiutdinov, arXiv:1103.4641.
- [55] D. Egger, S. T. Merkel, and F. K. Wilhelm (unpublished).
- [56] Dennis, Eric, Kitaev, Alexei, Landahl, Andrew, and Preskill, John, “Topological quantum memory,” *Journal of Mathematical Physics*, volume 43, no. 9, pp. 4452–4505, 2002
- [57] Fowler, Austin G., Mariantoni, Matteo, Martinis, John M., and Cleland, Andrew N., “Surface codes: Towards practical large-scale quantum computation,” *Phys Rev A*, volume 86, p. 032324, Sep 2012
- [58] Raussendorf, R, Harrington, J, and Goyal, K, “Topological fault-tolerance in cluster state quantum computation,” *New Journal of Physics*, volume 9, no. 6, p. 199, 2007
- [59] Fowler, Austin G., “Proof of Finite Surface Code Threshold for Matching,” *Phys Rev Lett*, volume 109, p. 180502, 2012
- [60] Fowler, Austin G., Whiteside, Adam C., and Hollenberg, Lloyd C. L., “Towards Practical Classical Processing for the Surface Code,” *Phys Rev Lett*, volume 108, p. 180501, May 2012
- [61] Fowler, Austin G., Whiteside, Adam C., and Hollenberg, Lloyd C. L., “Towards practical classical processing for the surface code: Timing analysis,” *Phys Rev A*, volume 86, p. 042313, 2012

- [62] Ghosh, Joydip, Galiautdinov, Andrei, Zhou, Zhongyuan, Korotkov, Alexander N., Martinis, John M., and Geller, Michael R., “High-fidelity controlled- $\sigma^Z$  gate for resonator-based superconducting quantum computers,” *Phys Rev A*, volume 87, p. 022309, Feb 2013
- [63] Fowler, Austin G., Whiteside, Adam C., McInnes, Angus L., and Rabbani, Alimohammad, “Topological Code Autotune,” *Phys Rev X*, volume 2, p. 041003, Oct 2012
- [64] Gottesman, Daniel, “Fault-Tolerant Quantum Computation with Higher-Dimensional Systems,” *Chaos Solitons Fractals*, volume 10, no. 10, pp. 1749 – 1758, ISSN 0960-0779, 1999
- [65] Hostens, Erik, Dehaene, Jeroen, and De Moor, Bart, “Stabilizer states and Clifford operations for systems of arbitrary dimensions and modular arithmetic,” *Phys Rev A*, volume 71, p. 042315, 2005
- [66] Bullock, Stephen S and Brennen, Gavin K, “Qudit surface codes and gauge theory with finite cyclic groups,” *Journal of Physics A Mathematical and Theoretical*, volume 40, no. 13, p. 3481, 2007
- [67] Jafarizadeh, M. A., Najarbashi, G., Akbari, Y., and Habibian, H., “Multi-qubit stabilizer and cluster entanglement witnesses,” *The European Physical Journal D*, volume 47, pp. 233–255, ISSN 1434-6060, 2008
- [68] Chen, Xie, Zeng, Bei, and Chuang, Isaac L., “Nonbinary codeword-stabilized quantum codes,” *Phys Rev A*, volume 78, p. 062315, 2008
- [69] Looi, Shiang Yong and Griffiths, Robert B., “Tripartite entanglement in qudit stabilizer states and application in quantum error correction,” *Phys Rev A*, volume 84, p. 052306, 2011

- [70] V. Gheorghiu, arXiv:1101.1519.
- [71] Dür, W., Hein, M., Cirac, J. I., and Briegel, H.-J., “Standard forms of noisy quantum operations via depolarization,” *Phys Rev A*, volume 72, p. 052326, Nov 2005
- [72] Dankert, Christoph, Cleve, Richard, Emerson, Joseph, and Livine, Etera, “Exact and approximate unitary 2-designs and their application to fidelity estimation,” *Phys Rev A*, volume 80, p. 012304, Jul 2009
- [73] Emerson, Joseph, Silva, Marcus, Moussa, Osama, Ryan, Colm, Laforest, Martin, Baugh, Jonathan, Cory, David G., and Laflamme, Raymond, “Symmetrized Characterization of Noisy Quantum Processes,” *Science*, volume 317, no. 5846, pp. 1893–1896, 2007
- [74] Sarvepalli, Pradeep Kiran, Klappenecker, Andreas, and Rötteler, Martin, “Asymmetric quantum codes: constructions, bounds and performance,” *Proceedings of the Royal Society A Mathematical Physical and Engineering Science*, volume 465, no. 2105, pp. 1645–1672, 2009
- [75] Silva, M., Magesan, E., Kribs, D. W., and Emerson, J., “Scalable protocol for identification of correctable codes,” *Phys Rev A*, volume 78, p. 012347, Jul 2008
- [76] Gutiérrez, Mauricio, Svec, Lukas, Vargo, Alexander, and Brown, Kenneth R., “Approximation of realistic errors by Clifford channels and Pauli measurements,” *Phys Rev A*, volume 87, p. 030302, Mar 2013
- [77] Magesan, Easwar, Puuzzoli, Daniel, Granade, Christopher E., and Cory, David G., “Modeling quantum noise for efficient testing of fault-tolerant circuits,” *Phys Rev A*, volume 87, p. 012324, Jan 2013

- [78] Wilhelm, F. K., Storz, M. J., Hartmann, U., and Geller, M.R., “Superconducting qubits II: Decoherence,” *Manipulating Quantum Coherence in Solid State Systems edited by M E Flatte and I Tifrea Springer 2007*, volume Springer, 2007, p. 195, 2007
- [79] Fowler, Austin G., Wang, David S., and Hollenberg, Lloyd C. L., “Surface code quantum error correction incorporating accurate error propagation,” *Quantum Information and Computation*, volume 11, pp. 0008–0018, 2011
- [80] Fowler, Austin G., “Analytic asymptotic performance of topological codes,” *Phys Rev A*, volume 87, p. 040301, Apr 2013
- [81] Helmer, F., Mariani, M., Fowler, A. G., von Delft, J., Solano, E., and Marquardt, F., “Cavity grid for scalable quantum computation with superconducting circuits,” *EPL Europhysics Letters*, volume 85, no. 5, p. 50007, 2009
- [82] Khaneja, Navin, Reiss, Timo, Kehlet, Cindie, Schulte-Herbruggen, Thomas, and Glaser, Steffen J., “Optimal control of coupled spin dynamics: design of {NMR} pulse sequences by gradient ascent algorithms,” *Journal of Magnetic Resonance*, volume 172, no. 2, pp. 296 – 305, ISSN 1090-7807, 2005